

Ferromagnetic colloids in liquid crystal solvents

Von der Fakultät für Mathematik und Physik der Universität Stuttgart
zur Erlangung der Würde eines Doktors der Naturwissenschaften
(Dr. rer. nat.) genehmigte Abhandlung

Vorgelegt von

Grigorii Sergeevich Zarubin

aus Nizhnii Tagil

Hauptberichter: Prof. Dr. Siegfried Dietrich

Mitberichter: Prof. Dr. C. Holm

Tag der mündlichen Prüfung: 27.02.2019

Institut für Theoretische Physik IV der Universität Stuttgart und
Max-Planck-Institut für Intelligente Systeme, Stuttgart

2018

Erklärung

Hiermit erkläre ich, Grigorii Zarubin, dass ich abgesehen von den ausdrücklich bezeichneten Hilfsmitteln die Dissertation selbständig verfasst habe.

Stuttgart, den 19.12.2019

Contents

List of abbreviations	7
1 Introduction	9
1.1 Liquid crystals	9
1.2 Colloids in liquid crystal	12
1.2.1 Colloidal suspensions	12
1.2.2 Effective colloidal interactions and colloidal stability	13
1.2.3 Colloidal particles in an NLC	18
1.2.4 Ferronematics	24
2 Methods	35
2.1 Density Functional Theory	35
2.2 Conjugate gradient method	41
3 Effective Landau theory of ferronematics	49
3.1 Introduction	49
3.2 Theory	52
3.2.1 Noninteracting particles in a nematic liquid crystal	52
3.2.2 Single disc-like colloid immersed in a nematic liquid crystal	55
3.2.3 Mesoscopic functional	58
3.3 Results	61
3.3.1 Limits of reliability for using the one-particle potential	61
3.3.2 Free energy functional in quadratic approximation	66
3.4 Discussion	71
4 Ferronematic slab in external magnetic fields	75
4.1 Introduction	75
4.2 Numerical model	78
4.3 Results	79
4.3.1 Switching mechanism I and the critical field	79
4.3.2 Switching mechanism II	87

4.3.3	Confining walls with different anchoring strengths	89
4.4	Segregation effects	93
4.5	Summary and conclusions	96
5	Conclusions and outlook	101
6	Summary	109
7	Zusammenfassung	115
Appendix A	Boundary problems for $\alpha^{(0)}$ and $\alpha^{(1)}$	121
A.1	Zeroth order in c	121
A.2	First order in c	122
A.3	Free energy	122
Appendix B	Quadratic approximation of the generating function $Z(\mathbf{h})$	125
Appendix C	Constraint of the field $\tau(z)$	129
Bibliography		131

List of abbreviations

LC	liquid crystal
NLC	nematic liquid crystal
MBBA	N-(4-Methoxybenzylidene)-4-butylaniline
5CB	4-cyano-4'-pentylbiphenyl
DFT	density functional theory
IA	infinite anchoring
WA	weak anchoring

Chapter 1

Introduction

1.1 Liquid crystals

The liquid crystalline state of matter as suggested by the name possesses properties that are typical for liquids, i.e., fluidity, formation of droplets when placed on the solid surface etc., and also properties characteristic of solid bodies, i.e., anisotropy of response to external electromagnetic fields as well as the presence of long range orientational and possibly positional order. Molecules of a liquid crystal (LC) have an anisotropic shape and therefore, unlike molecules of classical isotropic liquids that usually can be modelled to have a spherical shape, when brought close together interact through anisotropic steric potentials. As a result, either under sufficiently low temperature (*thermotropic* liquid crystals) or for sufficiently high packing fraction (*lyotropic* liquid crystals) a collection of such molecules undergoes a spontaneous breaking of rotational symmetry at each point developing a preferred orientation of molecular axes. A unit vector associated with such direction is called the director \mathbf{n} . Liquid crystals can be categorized into separate groups based on the microscopic structure of the mesophase. *Nematic* LCs exhibit anisotropy in one (*uniaxial* nematic) direction or two (*biaxial* nematic) directions but possess no spatial order. The simple case of a uniaxial nematic can be visualized using model of rod-like hard particles (see Fig. 1.1(a)). The nematic whose director in the bulk undergoes helical rotation with a certain constant pitch is known as *cholesteric* LC (see Fig. 1.1(b)). Formally one can think of nematics as being a particular case of cholesterics with an infinite pitch. Cholesteric mesophase becomes possible when molecules of an LC have distinct left- and right-handed forms. The existence of a biaxial nematic mesophase requires particles of more complicated shape (see Fig. 1.1(c)).

Along with having long range orientational order *smectic* LCs develop a spatially periodic structure through the formation of individual stacked layers of molecules (see Fig. 1.2). Within the layers spatial order is absent and the arrangement of molecules is liquid-like. There is a variety of smectic phases ranging from more common A (see Fig.

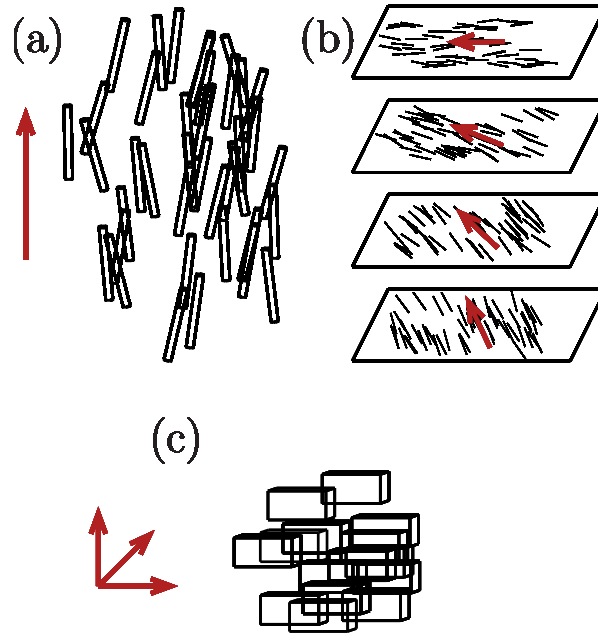


Figure 1.1: Schematic representation of: (a) Nematic liquid crystal phase of the liquid constituted of rod-like molecules (black rods). All the constituent molecules have their long axes directed along a particular local direction called director (red arrow); (b) Cholesteric phase. The director (red arrow) gradually rotates around a particular axis (vertical axis in this figure); (c) Biaxial nematic. In this simple example brick-shaped molecules (bricks) exhibit a preferred orientation in one direction (i.e., director, horizontal red arrow) and also an additional secondary direction (*either* of the arrows in the plane perpendicular to the horizontal arrow). Particles in (a) and (c) are represented as frames. The projections on the plane are showed and particles do not overlap in the corresponding three-dimensional representation.

1.2(a)) and C (see Fig. 1.2(c)) to more exotic ones such as B, E, F. All smectic phases differ from each other in the structure of the liquid within the layers.

A *columnar* LC phase is characterized by the stacking of the LC molecules in columns. Disc-shaped molecules are obvious candidates to exhibit columnar phases [1, 2, 3], however anisotropic particles of other shapes [5, 4] and even particles interacting through a spherically symmetric potential [6] has been shown to be capable of exhibiting columnar phases.

For the rest of the thesis a uniaxial nematic liquid crystal (NLC) is considered unless stated otherwise.

The fundamental microscopic anisotropy of the constituent molecules of an NLC manifests itself on the macroscopic level through the anisotropy of the response to external electromagnetic fields. The dielectric constant $\underline{\underline{\epsilon}}$ and the magnetic susceptibility $\underline{\underline{\chi}}$ of NLCs are both tensorial quantities. The uniaxial property of NLCs implies a certain

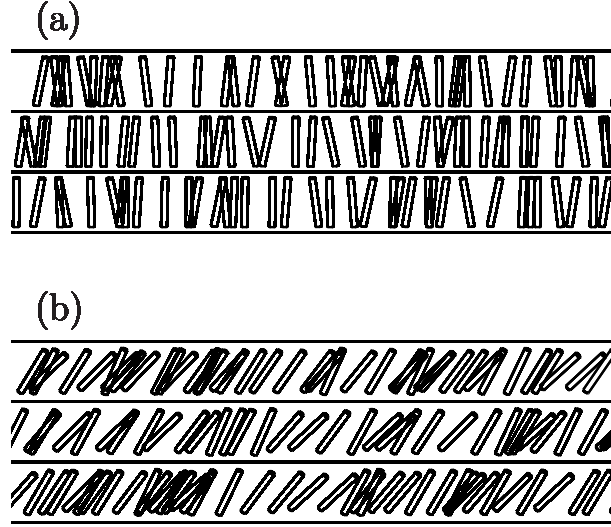


Figure 1.2: Schematic representation of: (a) Smectic A (LC molecules (black rods) exhibit a layered structure, inside each layer the centers of gravity show no long range order, each layer is a two-dimensional fluid, the system is uniaxial with the optical axis being the normal to the layers); (b) Smectic C (similar to smectic A except that the optical axis makes a nonzero angle with the normal to the layers). The projections on the plane are showed and particles do not overlap in the corresponding 3-dimensional representation. Thin black horizontal lines denote the boundaries of the layers.

mathematical structure of both $\underline{\underline{\varepsilon}}$ and $\underline{\underline{\chi}}$ (in the local frame of reference associated with the director such that $Oz \parallel \mathbf{n}$):

$$\underline{\underline{\varepsilon}} = \begin{bmatrix} \varepsilon_{\perp} & 0 & 0 \\ 0 & \varepsilon_{\perp} & 0 \\ 0 & 0 & \varepsilon_{\parallel} \end{bmatrix}, \quad \underline{\underline{\chi}} = \begin{bmatrix} \chi_{\perp} & 0 & 0 \\ 0 & \chi_{\perp} & 0 \\ 0 & 0 & \chi_{\parallel} \end{bmatrix}, \quad (1.1)$$

where elements carrying index \perp (\parallel) correspond to the response in the direction perpendicular (parallel) to the local director \mathbf{n} . It is often convenient to work with dielectric and magnetic *anisotropies* defined as

$$\begin{aligned} \varepsilon_a &:= \varepsilon_{\parallel} - \varepsilon_{\perp} \\ \chi_a &:= \chi_{\parallel} - \chi_{\perp}. \end{aligned} \quad (1.2)$$

While the dielectric anisotropy of the NLCs is usually relatively large ($\approx 1 - 13$ [7, 8, 9, 10]) therefore making the material very responsive to the external electric fields of low magnitude ($\propto 10^6$ V/m [11, 12]) their magnetic anisotropy is generally relatively small thus yielding NLC practically unresponsive to external magnetic fields of magnitude less than $\approx 7 \times 10^3$ mT (for a sample of thickness $100 \mu\text{m}$ [13]).

Although there are examples of liquid crystals with both positive and negative magnetic anisotropy χ_a , the former case is much more common [14]. A positive χ_a implies

that the molecules minimize their magnetic energy by aligning their long axis along the external magnetic field.

Thus, the molecular orientation and therefore the nematic director field \mathbf{n} can be manipulated by applying external electric or magnetic fields. A very useful feature of LCs is that the corresponding response can be easily observed using optical means. Naturally, an NLC, being an anisotropic material, exhibits birefringence and therefore when the light of a certain polarization enters the nematic sample its polarization after passing through the sample may be different from the initial one. If one places the nematic sample between crossed polarizers such that initially planar polarized light travels through the sample without changing its polarization the sample will appear black to the observer behind the second polarizer. If now the external field of suitable orientation is applied the director profile is distorted compared to the initial setup, the polarization of light gets rotated upon travelling through the sample and some light can go through the second polarizer. The sample appears bright.

The described electro- or magneto-optical response is at the core of the main industrial application of NLCs — liquid crystal displays.

It is one of the aims of the liquid crystal research to improve the current liquid crystal technologies or to invent new ways to manipulate liquid crystalline samples. A very interesting and effective way to alter the liquid crystalline response to external fields is to dope the nematic matrix with colloidal inclusions. Liquid crystal interacts with the colloids dispersed in it and if one has means to act on the colloids one effectively interacts with the liquid crystal too.

1.2 Colloids in liquid crystal

1.2.1 Colloidal suspensions

If one has two substances of known properties one of the ways to get a new substance with possibly new and exciting properties is to mix those two. Sometimes this is not a good idea like in the case of boiling oil and water. Other times it does work out nicely and one is able to get a new material with interesting physical properties. An example of the latter is a *colloidal suspension* where solid particles (*colloidal particles* or *dispersed phase*), usually of the size in the range 10 nm – 10 μm , are dispersed in a host liquid (*dispersion medium*).

Colloidal suspensions are all around us. The white viscous liquid known as latex is extracted from rubber trees in the Amazon rain forests is a suspension of polymeric particles of few hundred nanometers in diameter in water [15]. Something as simple as milk is actually a colloidal dispersion of droplets of fat and proteins in an aqueous plasma

containing molecularly dispersed lactose and certain mineral salts [16]. Paint on the wall is created by dispersing solid pigment particles of the submicron size in a liquid polymer solution [17].

The remarkable properties of colloidal suspensions are the main reason they attract an enormous amount of scientific interest. The property of being easily deformed by external stresses, external electromagnetic fields or sometimes even thermal fluctuations (the elastic constant of a hypothetical “colloidal crystal” is about 10 orders of magnitude smaller than that of a classical atomic crystal [18]) puts colloidal solutions into the class of *soft matter* systems.

The unique properties originate from the microscopic interactions between the constituent particles. Assuming the size of the dispersion medium particles to be about a few angstroms it is evident that studying the colloidal suspensions one would inevitably face a complication: the two ingredients of the solution live on hugely different length and time scales. The medium particles being small are fast and mobile while the colloids in comparison are large and slow. From the theoretical point of view this fundamental asymmetry renders the statistical mechanics problem of colloids to be practically impossible to solve if one considers it to be a simple mixture of ingredients. A rather elegant way to resolve this issue is to “integrate out” fast degrees of freedom, i.e., those related to the dispersion medium particles, thus reducing the problem to that of a one-component fluid.

1.2.2 Effective colloidal interactions and colloidal stability

Consider a model mixture of two species. We consider one of the species being composed of “large” and another one of “small” particles. Let us have N_1 large and N_2 small particles in volume V . Let the large particles have positions $\mathbf{R}_1, \mathbf{R}_2, \dots, \mathbf{R}_{N_1}$ and the small particles $\mathbf{r}_1, \mathbf{r}_2, \dots, \mathbf{r}_{N_2}$. For simplicity we assume that the particles interact with each other through a spherically symmetric pair potentials u . Then, the total potential energy of the system is the sum of three terms $U(\{\mathbf{R}\}, \{\mathbf{r}\}) = U_{11}(\{\mathbf{R}\}) + U_{22}(\{\mathbf{r}\}) + U_{12}(\{\mathbf{R}\}, \{\mathbf{r}\})$ where U_{pq} , $p, q \in \{1, 2\}$ are defined as:

$$\begin{aligned}
 U_{11}(\{\mathbf{R}\}) &:= \sum_{i=1}^{N_1} \sum_{j=i+1}^{N_1} u_{11}(|\mathbf{R}_i - \mathbf{R}_j|) \\
 U_{22}(\{\mathbf{r}\}) &:= \sum_{i=1}^{N_2} \sum_{j=i+1}^{N_2} u_{22}(|\mathbf{r}_i - \mathbf{r}_j|) \\
 U_{12}(\{\mathbf{R}\}, \{\mathbf{r}\}) &:= \sum_{i=1}^{N_1} \sum_{j=1}^{N_2} u_{12}(|\mathbf{R}_i - \mathbf{r}_j|),
 \end{aligned} \tag{1.3}$$

and where for brevity the notations $\{\mathbf{R}\} := \mathbf{R}_1, \mathbf{R}_2, \dots, \mathbf{R}_{N_1}$, $\{\mathbf{r}\} := \mathbf{r}_1, \mathbf{r}_2, \dots, \mathbf{r}_{N_2}$ are used. It is now straightforward to write down the corresponding Hamilton functions:

$$\begin{aligned}\mathcal{H}_{11} &= \sum_{i=1}^{N_1} \frac{\mathbf{P}_i^2}{2M} + U_{11}(\{\mathbf{R}\}) \\ \mathcal{H}_{22} &= \sum_{i=1}^{N_2} \frac{\mathbf{p}_i^2}{2m} + U_{22}(\{\mathbf{r}\}) \\ \mathcal{H}_{12} &= U_{12}(\{\mathbf{R}\}, \{\mathbf{r}\}),\end{aligned}\tag{1.4}$$

where \mathbf{P}_i , $i \in \{1, 2, \dots, N_1\}$ and \mathbf{p}_i , $i \in \{1, 2, \dots, N_2\}$ denote the momenta of large and small particles, respectively. We also call M and m the masses of large and small particles, respectively. The total Hamiltonian of the system is the sum $\mathcal{H} = \mathcal{H}_{11} + \mathcal{H}_{22} + \mathcal{H}_{12}$.

In the canonical ensemble the trace of a function $\mathcal{F}(\{\mathbf{P}\}, \{\mathbf{p}\}, \{\mathbf{R}\}, \{\mathbf{r}\})$ reads

$$\text{Tr}[\mathcal{F}] = \frac{h^{-3N_1}}{N_1!} \frac{h^{-3N_2}}{N_2!} \int d\{\mathbf{P}\} \int d\{\mathbf{R}\} \int d\{\mathbf{p}\} \int d\{\mathbf{r}\} \mathcal{F}(\{\mathbf{P}\}, \{\mathbf{p}\}, \{\mathbf{R}\}, \{\mathbf{r}\}),\tag{1.5}$$

where h denotes Planck's constant. The canonical partition function Q is the trace of the Boltzmann weight $\exp(-\beta\mathcal{H})$

$$Q := \text{Tr}[\exp(-\beta\mathcal{H})] = Q(N_1, N_2, V, T)\tag{1.6}$$

with T being the absolute temperature and $\beta := 1/(k_B T)$. The dependence on V in Q is implicit through the limits of spatial integrals in Eq. (1.5). The integrations over the momenta in Eq. (1.6) can be carried out explicitly [19] yielding

$$Q = \frac{1}{N_1! N_2!} \frac{1}{\Lambda_1^{3N_1} \Lambda_2^{3N_2}} Z(N_1, N_2, V, T),\tag{1.7}$$

where $\Lambda := \left(\frac{\beta h^2}{2\pi m}\right)^{\frac{1}{2}}$ is the de Broglie thermal wavelength (which is different for the two species due to the difference in mass) and $Z(N_1, N_2, V, T)$ is the so-called configurational integral:

$$Z(N_1, N_2, V, T) := \int d\{\mathbf{R}\} \int d\{\mathbf{r}\} \exp(-\beta U(\{\mathbf{R}\}, \{\mathbf{r}\}))\tag{1.8}$$

We now perform the integration over the coordinates of the small particles in Eq. (1.8) formally keeping the coordinates of the large particles constant. The result is a partial configurational integral that depends on $\{\mathbf{R}\}$:

$$Z_2(N_1, N_2, V, T, \{\mathbf{R}\}) := \int d\{\mathbf{r}\} \exp(-\beta U_{22}(\{\mathbf{r}\}) - \beta U_{12}(\{\mathbf{R}\}, \{\mathbf{r}\})).\tag{1.9}$$

Therefore it is possible to define a quantity

$$Q_2(N_1, N_2, V, T, \{\mathbf{R}\}) := \frac{1}{N_2!} \frac{1}{\Lambda_2^{3N_2}} Z_2(N_1, N_2, V, T, \{\mathbf{R}\})\tag{1.10}$$

which represents the partition function of the small particles in the external field of the large particles given that the large particles have positions $\{\mathbf{R}\}$. Comparing Eqs. (1.6), (1.7) and (1.10) we conclude that

$$Q = \text{Tr}_1 [\exp(-\beta\mathcal{H}_{11})Q_2(N_1, N_2, V, T, \{\mathbf{R}\})], \quad (1.11)$$

where the trace has index 1 because only integration over the large particles' degrees of freedom is implied. Thus, we formally reduced the statistical mechanics problem of the mixture of two types of particles to that of a one-component system of particles that interact through the *effective* Hamiltonian \mathcal{H}_{eff} defined as

$$\mathcal{H}_{\text{eff}}(\{\mathbf{P}\}, \{\mathbf{R}\}) := \mathcal{H}_{11}(\{\mathbf{P}\}, \{\mathbf{R}\}) - \frac{1}{\beta} \ln Q_2(N_1, N_2, V, T, \{\mathbf{R}\}). \quad (1.12)$$

The described procedure does not alter the original partition function Q (see Eq. (1.6)) and therefore does not alter the thermodynamical properties of the original system.

In order to understand the structure of the effective Hamiltonian it is useful to rewrite it in the form:

$$\mathcal{H}_{\text{eff}}(\{\mathbf{P}\}, \{\mathbf{R}\}) = \sum_{i=1}^{N_1} \frac{\mathbf{P}_i^2}{2M} + U_{11}(\{\mathbf{R}\}) - \frac{1}{\beta} \ln \left(\frac{Z_2}{V^{N_2}} \right) + \frac{V}{\beta} (\rho_2 \ln(\rho_2 \Lambda_2^3) - \rho_2) \quad (1.13)$$

where the last term in the above equation corresponds to the ideal gas contribution in the partition function (1.10) and $\rho_2 := N_2/V$ was defined. The third term in Eq. (1.13) is the contribution to the *effective interaction* between large particles due to small particles. Since this term depends also on the thermodynamic quantities (temperature, number of particles N_1 and N_2 and therefore densities ρ_1 and ρ_2) one arrives at one of the nice and extremely useful properties of effective interactions: one can tune them externally by tuning macroscopic thermodynamic parameters.

If one could calculate the integrals in Eq. (1.9) analytically then the effective Hamiltonian Eq. (1.12) would be known exactly. This is the case only in a very limited number of situations (e.g., for the so-called Asakura-Oosawa model of the colloid-ideal polymer coils mixture and only if the ratio of the radii of the constituent particles is smaller than $2/\sqrt{3} - 1$ [20]) and therefore usually one is forced to use approximations. A diagrammatic expansion of Z_2 (see Eq. (1.9)) has been performed by Dijkstra, van Roij and Evans [21].

These authors showed that the corresponding expansion has the following structure

$$-\frac{1}{\beta} \ln \left(\frac{Z_2}{V^{N_2}} \right) = \sum_{n=0}^{\infty} K_n \quad (1.14)$$

$$K_0 = V k_0(\rho_1, \rho_2, T) \quad (1.15)$$

$$K_1 = \sum_{i=1}^{N_1} k_1(\mathbf{R}_i, \rho_1, \rho_2, T) \quad (1.16)$$

$$K_2 = \sum_{i=1}^{N_1} \sum_{j=i+1}^{N_1} k_2(|\mathbf{R}_i - \mathbf{R}_j|, \rho_1, \rho_2, T) \quad (1.17)$$

$$K_3 = \sum_{i=1}^{N_1} \sum_{j=i+1}^{N_1} \sum_{q=j+1}^{N_1} k_3(|\mathbf{R}_i - \mathbf{R}_j|, |\mathbf{R}_i - \mathbf{R}_q|, |\mathbf{R}_j - \mathbf{R}_q|, \rho_1, \rho_2, T) \quad (1.18)$$

and so on. Terms k_i , $i \in \{0, 1, 2, \dots\}$ represent i -body effective interactions. Clearly, the original problem possesses the translational symmetry and therefore $k_1 = 0$ is required since this one body interaction violates the symmetry. The sum in Eq. (1.14) is often truncated after $n = 2$ thus yielding the *pair-potential approximation*. The corresponding effective Hamiltonian thus reads

$$\mathcal{H}_{\text{eff}}(\{\mathbf{P}\}, \{\mathbf{R}\}) = \sum_{i=1}^{N_1} \frac{\mathbf{P}_i^2}{2M} + \sum_{i=1}^{N_1} \sum_{j=i+1}^{N_1} U_{\text{eff}}(|\mathbf{R}_i - \mathbf{R}_j|, \rho_1, \rho_2, T) + V f_0(\rho_1, \rho_2, T), \quad (1.19)$$

where

$$U_{\text{eff}}(R, \rho_1, \rho_2, T) = u_{11}(R) + k_2(R, \rho_1, \rho_2, T) \quad (1.20)$$

and the notation $f_0(\rho_1, \rho_2, T) := k_B T (\rho_2 \ln(\rho_2 \Lambda_2^3) - \rho_2) + k_0(\rho_1, \rho_2, T)$ was introduced. The term $V f_0$ represents a so-called volume term (it scales with the system volume, hence the name). Since the volume term does not depend on the inter-colloidal distance it does not affect the effective pair interaction. However, the volume term becomes important when one deals with phase transitions since it depends on the densities ρ_1 and ρ_2 .

The form of the effective pair potential becomes relevant in the context of *colloidal stability*. Any colloidal particle undergoes Brownian random motion and therefore two colloids can in principle approach each other down to the inter-particle distances of the order of the colloidal size. As a consequence of the random fluctuations of the electron density inside the colloidal particles two such particles acquire instantaneous dipole moments and thus attract each other and the corresponding interaction is called van der Waals interaction [22]. The van der Waals interaction is long-ranged with $1/r^6$ decay over the intermediate separations and $1/r^7$ decay for very large separations due to retardation effects. In the simplest case of two identical spherical particles separated by a distance r the van der Waals interaction reads [23]:

$$U_{\text{vdW}} = -\frac{1}{6} A \left(\frac{2R^2}{r^2 - 4R^2} + \frac{2R^2}{r^2} + \ln \left(\frac{r^2 - 4R^2}{r^2} \right) \right), \quad (1.21)$$

where $A > 0$ is the Hamaker constant that depends on the materials (polarizabilities) of both spheres. The potential in Eq. (1.21) diverges towards $-\infty$ for $r \rightarrow 2R$. Therefore it is required to have a repulsive contribution to the effective interaction in order to prevent colloids from aggregating. There are two main methods used in the experiments. The first is the steric stabilization, where the surface of sterically stabilized colloidal particles is decorated with polymer brushes. In a very good solvent polymers tend to maximize the volume available to each monomer therefore resulting in longer self-avoiding chains. If a polymeric brush has sufficient density (number of different polymeric chains per unit area of the colloidal particle) and two colloids approach each other down to distance $\sim 2(R+L)$, where L is the average length of a polymer in a brush, the polymers belonging to different particles start to overlap therefore reducing the effective volume available to their monomers. The such created effective steric repulsion might be used to suppress the van der Waals attraction and therefore to stabilize the solution.

Using steric stabilization has several advantages. By changing the temperature one can adjust the degree of how “good” the solvent is and therefore change the effective length L of the polymer chains thus changing the effective range of the steric repulsion. One can explicitly change L during the production of the polymers by changing the degree of polymerization (i.e., the number of monomers per polymer chain). The density of polymers in the brush also effectively alters the strength of the repulsion.

The second method is the electrostatic stabilization. If a body that carries ionizable groups on its surface is suspended in a polar solvent it releases ions into the solvent thus acquiring a surface charge density σ corresponding to a so-called bare charge Z . The released ions together with the anions and cations of the solvent form coion and counterion densities. The charge Z is usually in the range $10^2 - 10^4$ elementary charges in the case of colloidal suspensions and therefore the body is referred to as a macroion. The oppositely charged ions form a complicated charge density profile around the macroion which, in the simplest model, is traditionally separated into two groups: (i) in the closest vicinity of the macroion surface the counterions become “adsorbed” and form a tightly bound layer known as *Stern layer*, charges belonging to the Stern layer significantly reduce the total charge of the macroion + stern layer compound therefore adjusting $Z \rightarrow Z^* < Z$; (ii) the new effective charge Z^* is seen by the free counterions in the solution which then form the *diffuse layer* and therefore the rest of the “cloud” of counterions around the macroion. Determination of the details of the exact microion density profile represents a challenging theoretical task not only because of the large asymmetry between the macroion and microion particles but also because the microscopic properties of the profile represent an intricate interplay between the surface chemistry and the local inhomogeneities induced by electrostatics.

The diffuse layer of the counterions screens the effective macroion charge Z^* and there-

fore two macroions separated by the distance r interact through the screened Coulomb effective pair potential

$$U_{\text{SC}} = \frac{(\tilde{Z}e)^2 \exp(-\kappa r)}{\varepsilon r}, \quad (1.22)$$

where ε is the dielectric constant of the medium, e is the elementary charge, \tilde{Z} is a charge incorporating finite-size polyion effects given by

$$\tilde{Z} := Z^* \frac{\exp(\kappa R)}{1 + \kappa R} \quad (1.23)$$

for the spherical macroions of radius R and κ is the inverse Debye screening length

$$\kappa := \sqrt{\frac{4\pi\rho_c(qe)^2}{\varepsilon k_B T}} \quad (1.24)$$

with ρ_c being the density of free counterions and q being their valence.

The potential in Eq. (1.22) can be tuned externally by tuning the temperature or ε (changing the solvent) since the range of the potential κ depends on those parameters (see Eq. (1.24)). One could also tune κ by adding some extra salt in the solution thus supplying additional charges. In that case the product of the square of the charge and the counterion concentration in Eq. (1.24) would be modified.

For separations larger than the colloid diameter, $r > 2R$, the superposition of the Van-der-Waals and the screened Coulomb potential result in the Derjaguin-Landau-Verwey-Overbeek (DLVO) potential $V_{\text{DLVO}}(r) = U_{\text{VdW}}(r) + U_{\text{SC}}(r)$. The van der Waals interaction and the screened Coulomb interaction are in a sense conventional. Among the less conventional types of interactions are the critical Casimir interaction [24, 25] (e.g. between so-called Janus particles suspended in a critical binary mixture) and depletion forces between large colloids suspended in a sea of much smaller particles (e.g. aforementioned Asakura-Oosawa interaction potential).

1.2.3 Colloidal particles in an NLC

The previous section dealt with colloidal suspensions in isotropic liquids.

Obviously, going from an isotropic liquid to the anisotropic one adds an extra level of complication to the theoretical description. In this work only one step in the direction of increasing the complexity is made, i.e., we step away from the purely isotropic liquid and introduce a uniaxial directional anisotropy to the dispersion medium, i.e., we consider a nematic liquid crystal. As we show below such a step gives the medium a property of elasticity and thus a new type of effective interactions between the colloids suspended in such medium.

As mentioned in Sec. 1.1 NLC molecules are of anisotropic shape. Canonical examples include N-(4-Methoxybenzylidene)-4-butylaniline (MBBA) [26, 27, 28] and 4-cyano-4'-pentylbiphenyl (5CB) [29, 30, 31]. The molecules of the NLC need not to be symmetric

with respect to the transformation “head – tail” and therefore one could in principle assign a direction to each individual molecule but since at each point there are on average as many molecules “pointing in one direction” as there are those “pointing in the opposite direction” one can conclude that the director \mathbf{n} is not a vector but an *axis*. This consideration implies that physical quantities that depend on \mathbf{n} should be invariant with respect to the transformation $\mathbf{n} \rightarrow -\mathbf{n}$.

Let us now consider a particular physical quantity, the free energy, in the context of *distortions* of the director field $\mathbf{n}(\mathbf{r})$. In a free space filled with an NLC the static equilibrium configuration would be that of a uniform nematic, i.e., $\mathbf{n}(\mathbf{r}) = \text{const}$. However confining walls, external fields, or colloidal inclusions may impose conditions under which the nematic director is in a distorted state.

In order to get an expression for the free energy cost due to distortions one can use a somewhat “brute-force” approach. Obviously, the free energy of elastic distortions is a function of the components of the gradient of the director field, i.e., $F_{\text{el}} = F_{\text{el}}(\partial n_i / \partial x_j)$, where $i, j \in \{1, 2, 3\}$ and x_j are the components of the position vector $\mathbf{r} = (x_1, x_2, x_3)$ within some basis. The free energy has to be invariant with respect to the transformation $\mathbf{n} \rightarrow -\mathbf{n}$ and therefore contains only even powers of $\mathbf{n}(\mathbf{r})$. If one now restricts the description to the free energies quadratic in $\mathbf{n}(\mathbf{r})$ it is a feasible (although cumbersome) task to figure out which terms are allowed under symmetry constraints which include [32]:

- rotations about an axis parallel to $\mathbf{n}(\mathbf{r})$;
- a mirror plane perpendicular to $\mathbf{n}(\mathbf{r})$;
- an infinite number of two-fold axes also perpendicular to $\mathbf{n}(\mathbf{r})$.

These symmetry elements represent symmetry elements of a cylinder and correspond to point group $D_{\infty h}$. The free energy that fulfills the above requirements is the Frank-Oseen elastic energy [33]

$$F_{\text{el}} = \int_{\mathcal{V}} d\mathbf{r} [f_{\text{el}} + f_{24}] \quad (1.25)$$

where \mathcal{V} is the sample volume and f_{el} reads

$$f_{\text{el}} = \frac{1}{2} \left[K_1 (\nabla \cdot \mathbf{n}(\mathbf{r}))^2 + K_2 (\mathbf{n}(\mathbf{r}) \cdot [\nabla \times \mathbf{n}(\mathbf{r})])^2 + K_3 [\mathbf{n}(\mathbf{r}) \times [\nabla \times \mathbf{n}(\mathbf{r})]]^2 \right] \quad (1.26)$$

and represents the free energy density of the bulk distortions and f_{24} is the so-called saddle-splay term

$$f_{24} = -\frac{K_{24}}{2} \nabla \cdot (\mathbf{n}(\mathbf{r}) \cdot (\nabla \cdot \mathbf{n}(\mathbf{r})) + \mathbf{n}(\mathbf{r}) \times [\nabla \times \mathbf{n}(\mathbf{r})]), \quad (1.27)$$

which is a divergence of a certain vector field (see the expression in brackets in Eq. (1.27)) and therefore can be transformed into an integral over the surfaces of the sample and

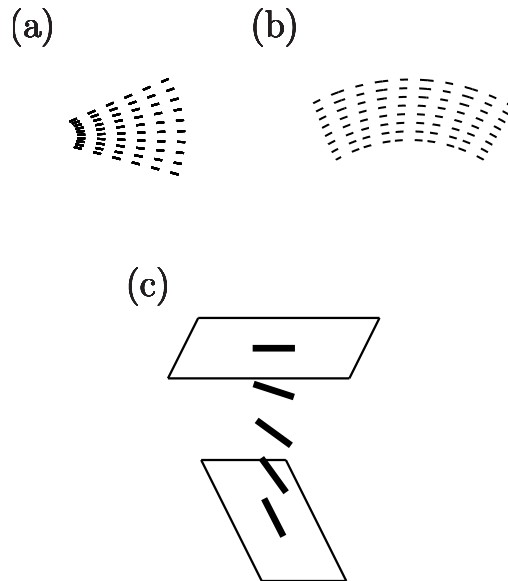


Figure 1.3: Schematic representation of three possible bulk distortion modes. Black rods represent the local director field. (a) Splay ($\nabla \cdot \mathbf{n} \neq 0$); (b) Bend ($\mathbf{n} \times [\nabla \times \mathbf{n}] \neq 0$); and (c) Twist ($\mathbf{n} \cdot [\nabla \times \mathbf{n}] \neq 0$).

therefore is not a bulk contribution. The coefficients K_{ij} in Eqs. (1.26) and (1.27) are called elastic constants and have the dimension of force.

It is clearly seen from the form of the free energy density in Eq. (1.26) that any bulk distortion represents a superposition of three modes: splay ($\nabla \cdot \mathbf{n} \neq 0$, elastic constant K_1), twist ($\mathbf{n} \cdot [\nabla \times \mathbf{n}] \neq 0$, elastic constant K_2), and bend ($\mathbf{n} \times [\nabla \times \mathbf{n}] \neq 0$, elastic constant K_3). Different distortion modes are schematically shown in Fig. 1.3. Elastic constants for usual nematics are of the order of $10^{-12} - 10^{-11}$ N [33] and the relation $K_3 \geq K_1 > K_2$ is holds.

The saddle-splay term f_{24} (see Eq. (1.27)) contains second-order spatial derivatives of $\mathbf{n}(\mathbf{r})$ and represents a significant contribution to the free energy when the nematic is subject to curved boundary condary conditions or mixed types of anchoring to the sample walls. The examples of systems where the saddle-splay term influences the stability of the equilibrium director field distribution and therefore phase diagram include submicron sized nematic droplets [34], cylindrical confinements with homeotropic [35] and planar wall anchorings [36], knotted colloidal particles [37], and planar walls with an array of circular holes in them [38]. It also plays a substantial role in the case of a wall with a patch of a different type of anchoring of the nematic to the surface [37]. The value of the corresponding elastic constant K_{24} , although possibly measured experimentally, remains a challenge from the theoretical point of view [39].

The interaction of an NLC with surfaces is the crucial part of any liquid crystal related theoretical investigation or real life device. The way the director prefers to align at the

surface is called anchoring. If the surface imposes a certain preferred direction, called *easy axis*, on the director the anchoring is said to be nondegenerate.

One can think of several different possibilities for the easy axis to be oriented with respect to the surface normal. If the easy axis is parallel to the surface normal or equivalently the liquid crystal molecules prefer to align their axes of cylindrical symmetry with the normal of the surface at any given point of the surface then such a configuration is called homeotropic anchoring and it is usually found when the surface is treated with chemical compounds that have long chains extending into the bulk [40, 41, 42, 43].

If the surface is rubbed using cloth [44] or diamond paste [45] creating grooves directly in the surface material [45] or in the layer of polymers adsorbed on the surface [44] elongated molecules of the liquid crystal “fit” into the grooves therefore adopting an anisotropic in plane configuration directly at the surface which then propagates into the bulk due to elasticity (see Eq. (1.26)) and the corresponding mechanism is called planar anchoring. In this case the easy axis is in plane perpendicular to the surface normal.

The possible surface configurations of course are not limited to the nondegenerate cases. In the case of degenerate anchoring the preferred direction that the nematic director adopts at the surface is not limited to a single easy axis. The corresponding azimuthal angle (the direction of the projection of the director onto the surface) is free to change between two or more discrete stable state values [46, 47, 48, 49] or even in the full continuous range $[0, 2\pi]$ [50, 51].

More exotic anchoring scenarios are achieved by elaborate treatments of the surface. Among those are bistable anchoring produced by nanoscale rubbing of the surface with the tip of an atomic force microscope [52], periodically changing anchoring patterns used to produce highly efficient diffraction gratings [53, 54, 55, 56], rotation of the in-plane easy axis by $\pi/2$ upon changing the number of methylene molecules in the deposited molecules by one [57] and others.

The theoretical description of the corresponding interaction between the liquid crystal and the surface is a demanding task but it is usually sufficient to use a simple form due to Rapini and Papoular [58]

$$F_s = W \int_{\partial\mathcal{V}} d\mathbf{s} [\mathbf{n}(\mathbf{s}) \times \boldsymbol{\nu}(\mathbf{s})]^2, \quad (1.28)$$

where $W > 0$ is the *anchoring energy* measured in J/m^2 , \mathbf{s} is a point of the surface $\partial\mathcal{V}$ and $\boldsymbol{\nu}(\mathbf{s})$ is the easy axis direction on the surface at point \mathbf{s} .

Any solid body added to the liquid crystal can be treated as a surface the NLC is in contact with. One can therefore treat colloidal particles suspended in the NLC as a source of surface terms described by Eq. (1.28). The presence of colloidal particles strongly anchored to the NLC can potentially distort the homogeneous director profile due to the presence of additional boundary conditions or in other words each colloid would create a

distortion of the liquid crystal director profile around it. If now two such distortion clouds created by two different particles overlap in space a new kind of an effective interaction arises – an *effective elastic interaction*. This interaction is not present in the suspensions of the colloidal particles in isotropic liquids and it is a direct manifestation of the anisotropic nature of the host liquid.

It is considerably more straightforward to consider the limit of *infinitely strong* anchoring of the NLC to the surface of the particle, i.e., the direction of the director at any point of the surface is fixed, thus augmenting the problem with Dirichlet boundary conditions and the surface term Eq. (1.28) drops out from the energy functional one has to minimize.

Unlike for the case of isotropic liquids, a spherical colloidal particle is not the simplest example when one is concerned with anisotropic solvents. The scientific interest in the dispersions of spherical colloidal particles in an NLC rose considerably only after the excellent experiment performed by Poulin et al. [59]. The authors of Ref. [59] studied a so-called “reverse emulsion” of spherical water droplets inside bigger nematic droplets. The notion “inverse” stems from the fact that the opposite case of nematic drops in water was historically first to be investigated. Experiments with the inverse emulsion showed that water spheres formed extremely stable linear chains and that their thermal Brownian motion was completely suppressed. The chains broke and water droplets started exhibiting Brownian motion again after the nematic was heated up and the transition to the isotropic phase took place. It was proposed that the formation of chains was caused by a novel colloidal effective interaction and the fact that it disappeared upon entering the isotropic phase of the nematic suggested that the interaction was exclusively due to the anisotropy of the liquid crystalline phase.

In order to understand the outcome of the experiment in Ref. [59] it was necessary to study the director profile around a spherical colloidal particle. Terentjev and coworkers [60, 61, 62, 63] started the investigation using the assumption of infinite anchoring of the director to the surface of the spherical inclusion. Lubensky et. al. [64] discussed the possible nematic configurations in the context of inverse nematic emulsions inspired by the experiment of Poulin et al. [59]. The authors of Ref. [64] looked at two qualitatively different situations of an equatorial defect line (“saturn ring defect”) and a point defect accompanying the particle (“hedgehog defect”). Owing to the symmetry of the defect-particle pair the authors of Ref. [64] proposed an ansatz analogous to electrostatic identifying the saturn ring defect with the elastic quadrupole and the hedgehog defect with the elastic dipole. The dipole symmetry of the hedgehog defect was able to qualitatively explain the chaining of water droplets in the experiment in Ref. [59]. Stark [65] found that whether a saturn ring or a hedgehog scenario is realized depends on the size of the particle and the anchoring energy W . Later it was shown experimentally that either

of the configurations can be stabilized using thicker or thinner confinement [66].

The corresponding elastic interaction was measured experimentally [67, 66, 68, 69, 70, 71] and investigated numerically using the minimization of the free-energy of the NLC formulated using the Frank-Oseen functional [72] or the free-energy formulated as an expansion in the tensorial order parameter of the NLC [73, 74, 76, 75, 77, 78]. The large-separation asymptotics dictated by the analogy of the elastic interactions with the electrostatic quadrupole ($\propto 1/r^5$) and dipole interactions ($\propto 1/r^3$) was confirmed both experimentally and numerically for separations larger than 10 particle radii. The short range part of the potential could not be predicted analytically since it is determined by the interaction of the topological defects accompanying each particle. When two topological defects approach each other they interact causing the change in their position with respect to the situation of the isolated colloid and possibly even merge into one topological defect (the latter is relevant for a pair of saturn ring defects) thus yielding a complicated nonlinear and possibly many-body nature of the interaction at small separations.

Lev and Tomchuk [79] derived the effective interparticle interaction between the colloidal particles under the condition of weak anchoring of the particles to the liquid crystal. In particular within the case of the one elastic constant approximation the elastic potential of Lev and Tomchuk reduced to the expression involving spatial derivatives of the inverse absolute value of the inter-colloidal separation which could be identified as an elastic multipole expansion. Later, Lev et. al. pointed out the role of the symmetry of the nematic distribution [80, 81] in the corresponding elastic pair potential. The type of the far field dependence of the elastic pair potential on the separation distance was connected to the symmetry of the nematic “coat” around each particle. The coat was defined such that any defect accompanying the colloid was included inside the coat thus the particle was effectively replaced by the fictitious new particle that has a much weaker anchoring of the liquid crystal on its surface (since it does not spawn any defect outside its boundaries). It was concluded by the authors of Ref. [80] that if the coat has three perpendicular symmetry planes the far field interaction is of quadrupolar type and falls off as $1/r^5$. If one of the three symmetry planes is absent then an elastic dipole is created perpendicular to it and the interaction decays as $1/r^3$. If two symmetry planes are absent the result is a *Coulomb-like* interaction between the colloids. The latter is possible when there is an external torque acting on the otherwise dipolar or quadrupolar colloid thus inclining the colloid (and therefore the coat) with respect to the far field homogeneous director. The Coulomb like interaction was later derived by Pergamenshik and Uzunova [82] who explicitly showed that the Euler-Lagrange equation corresponding to the Frank-Oseen functional under the assumption of the large separation between colloidal inclusions and the one elastic constant approximation reduces to the Laplace equation for the director components perpendicular to the far field director. Pergamenshik and Uzunova were not

the first to formulate the direct mathematical analogy between electrostatics and nematic distortions far away from the distorting body. De Gennes got the corresponding Laplace equations in his celebrated book [33] for the case of a “floating body”. He also predicted that long range distortions of the liquid crystal from such a body would decay at most as $1/r$ and that $1/r$ decay is generated due to the presence of the external torque that rotates the body in an NLC. The authors of Refs. [83, 82] got an analytic expression for the Coulomb-like elastic interaction:

$$U_{\text{el, Coulomb}} = -\frac{\mathbf{\Gamma}_{\perp}^{(1)} \cdot \mathbf{\Gamma}_{\perp}^{(2)}}{4\pi Kr}, \quad (1.29)$$

where $\mathbf{\Gamma}_{\perp}^{(i)}$ is the transverse (with respect to the far field homogeneous director) component of the external torque acting on a colloid i . One can identify two torques in Eq. (1.29) as “elastic charges” in analogy with the Coulomb interaction between two electric charges. An interesting consequence of the form of the interaction in Eq. (1.29) is that two colloids in the NLC can either repel or attract each other based on the sign of the scalar product between the torques that are imposed on each particle.

The electrostatic analogy could be pushed even further to investigate the interaction of such particles suspended in an NLC with a confining wall. Pergamenshik and Uzunova [84] developed a method of “elastic image charges” to investigate the behavior of quadrupolar, dipolar, and monopolar (i.e., Coulomb-like) colloids near a wall. The same authors summarized the previous results and developed a systematic approach to the effective elastic interactions in the context of the electrostatic analogy under the name of “colloidal nematostatics” [82].

The above discussion was dedicated to somewhat larger colloidal particles (size of $\geq 1 \mu\text{m}$) which inevitably introduce considerable distortions of the NLC. Moreover no “internal” degrees of freedom were attached to the colloids. Of particular interest is the case when a colloidal particle carries a dipole, either electric or magnetic, such that its orientation can be controlled by the external electric or magnetic field.

1.2.4 Ferronematics

It was mentioned in Sec. 1.2.3 that the case of spherical colloidal particles was not historically the first to be considered by the scientific community. Almost five decades ago Brochard and de Gennes [85] in their pioneering work proposed a very simple and elegant idea: one, in principle, should be able to enhance the susceptibility of a liquid crystalline matrix to an external magnetic field by doping the NLC with anisotropic (rod- or disc-like) particles that carry a magnetic moment. Brochard and de Gennes considered the case of infinite anchoring at the surface of the colloidal particle. They performed approximate calculations of the difference between the free energy of the particle suspended in an NLC

for situations when the long axis of the particle is parallel (F_{\parallel}) and perpendicular (F_{\perp}) to the far-field homogeneous director. In all of the considered nondegenerate boundary conditions at the colloid's surface (the easy axis is parallel to the particle's long axis and tangential to the surface, the easy axis is perpendicular to the particle's long axis and tangential to the surface, the easy axis is perpendicular to the surface) Brochard and de Gennes found that for sufficiently large particles the energy barrier between two perpendicular orientations of the particle with respect to the far-field director significantly exceeds the thermal energy $k_{\text{B}}T$:

$$\Delta F := |F_{\parallel} - F_{\perp}| \propto KL \gg k_{\text{B}}T, \quad (1.30)$$

where L is the size of the colloid. For room temperature and a colloid of size $L = 1 \mu\text{m}$ suspended in an NLC with $K = 3.5 \times 10^{-12}$ N one obtains $\Delta F \approx 10^3 k_{\text{B}}T$.

The first attempt to realize a ferronematic suspension experimentally was made in the same year as the theoretical work of Brochard and de Gennes [86] and later by Chen and Amer in 1983 [87] and Liang and Chen [88]. Chen and Amer used 500 nm long needle-like particles with an aspect ratio of 7:1. The surface of the needles was treated chemically as to obtain a homeotropic anchoring to the nematic, thus in the equilibrium state of the suspension all the colloids had their long axes in the plane perpendicular to the homogeneous director profile. The authors of [87] aimed at the demonstration of the so-called *collective behavior* that was predicted to occur for sufficiently high concentrations by Brochard and de Gennes [85]. To do so, Chen and Amer applied an external magnetic field perpendicular to the plane in which the long axes of the colloids lie and, since the magnetic moments of individual colloids were parallel to the long axis, each needle felt the presence of the magnetic field and started to rotate. The change in birefringence of the sample using a polarisation microscope was observed. Upon the application of the external field a thresholdless distortion of the bulk of the liquid crystal was observed which corresponded to the homogeneous brightening of the sample when seen under the polarization microscope. Thus Chen and Amer concluded that they observed a manifestation of the collective behavior due to the magnetic needles. The fact that the distortion of the liquid crystal occurred for arbitrarily small magnetic fields makes the phenomenon qualitatively different from the usual Frederiksz transition where a certain critical magnetic field is required to introduce a bulk distortion of the NLC [33].

Chen and Amer studied the phase difference between the ordinary and the extraordinary waves as a function of the magnetic field strength, the sample thickness, and the particle volume fraction. They also proposed an analytical expression for the phase difference in terms of relevant experimental parameters and showed that their expression provided an excellent description of the experimental data for small magnitudes of the external magnetic field. However, for larger fields the authors of Ref. [87] observed what

they called a “cellular” texture, i.e., a previously uniformly distorted sample went through the transition into an array of “cells” of the $\approx 10 \mu\text{m}$ in size. The cellular structure was attributed to the flocculation of colloidal particles into larger aggregates. The flocculation of the particles could not be interpreted in terms of the magnetic dipole-dipole attraction because it was too weak to cause the chaining of the particles. Chernyshuk et. al. [89] found a theoretical explanation after extending the theory of Lev and Tomchuk [79] and calculating the corresponding effective elastic pair interaction in the case of thin rods. It was shown that such anisotropic particles interact through the screened Coulomb potential with the effective charge (and sign) that depends on their orientation. It was concluded that the action of the large magnetic field causes the screened Coulomb attraction of the colloidal particles which makes particles flocculate once the attraction becomes larger than the repulsion due to the treatment of the particle’s surface with the surfactant.

It quickly became obvious that the theoretical approach of Brochard and de Gennes [85] could not be unconditionally applied to real experimental situations because the assumption of infinite coupling between the particle and the liquid crystal is not realised in practice. It was established that, in fact, nematic director *can* deviate from the easy axis on the surface of the colloidal particle. Taking the theory of Brochard and de Gennes as a base, Burylov and Raikher [90] formulated a similar theory which took into account the fact that the anchoring energy W (see Eq. (1.28)) can have a finite value. An important dimensionless combination WR/K was introduced with R being the size of the colloid. The authors of Ref. [90] argued that the approach of Brochard and de Gennes could be adopted only in the limit $WR/K \gg 1$ which was not the case for real experimental systems. Important comments were made concerning the preparation of a *ferromagnetic phase* of a ferronematic. Consider for example a suspension of needle-like particles that have a planar anchoring of the NLC at the surface. Rotational entropy considerations imply that in the equilibrium state in the absence of an external magnetic field there should be no net magnetization of the sample, i.e., there should be on average as many particles whose magnetic moments point in the direction \mathbf{n} as there are particles whose magnetic moments point in the direction $-\mathbf{n}$. Burylov and Raikher argued that there are two ways to break this binary orientational symmetry in the context of real experiments: (i) one can prepare the suspension at a temperature that is higher than the isotropic-nematic transition temperature of the liquid crystalline material and apply an external magnetic field in either direction. All magnetic moments of the colloids will be aligned along the field and a subsequent *quench* of the sample into the nematic phase of the liquid crystal will trap this orientation of the colloids (and, thus, of their magnetic moments) and yield a uniformly magnetized sample. (ii) One can use a short pulse of a strong magnetic field which makes individual magnetic moments overcome the magnetic anisotropy barrier

and switch *within* the colloid. If the pulse is shorter than the characteristic time it takes for the particle to rotate inside the liquid crystal the method should produce a uniformly magnetized ferronematic sample. The situation is more straightforward if one deals with homeotropically anchored needles. In that case the particles can freely rotate in the plane perpendicular to the director and in order to align them one would need to apply a constant bias magnetic field in that plane.

Arguably the most important result of Ref. [90] is the expression for the free energy density of the ferronematic:

$$f_{\text{FN}}^{\text{BR}} = f_{\text{el}} - \frac{1}{2}\chi_a\mu_0(\mathbf{n}(\mathbf{r}) \cdot \mathbf{B})^2 - \mu_0M_s v(\mathbf{r})(\mathbf{m}(\mathbf{r}) \cdot \mathbf{B}) + k_{\text{B}}T \frac{v(\mathbf{r})}{V_0} \ln v(\mathbf{r}) + A \frac{Wv(\mathbf{r})}{L}(\mathbf{n}(\mathbf{r}) \cdot \mathbf{m}(\mathbf{r}))^2, \quad (1.31)$$

where f_{el} is the elastic energy of the NLC (see Eq. (1.26)), M_s is the magnetization (magnetic moment per volume) of the individual colloid, v is the volume fraction of the colloids, $\mathbf{m}(\mathbf{r})$ is the unit vector in the direction of the local magnetization of the ferronematic at a point \mathbf{r} , V_0 is the volume of the colloidal particle, and A equals -2 in case of planar anchoring and 1 in case of homeotropic anchoring. The second term in Eq. (1.31) describes the coupling of the liquid crystal to the external magnetic field due to a nonzero magnetic anisotropy χ_a of the constituent molecules (see Sec. 1.1). The third term couples the magnetic colloids to the magnetic field. The fourth term favors the homogeneous distribution of the particles throughout the sample and is of entropic nature. The last term is the coupling of the nematic director to the magnetization field due to the coupling of the colloids to the liquid crystal. This term is essential for the description of the processes in the ferronematic. Burylov and Raikher derived the last term on the rhs of Eq. (1.31) based on the expression for the orientational energy of a *single* colloid in an NLC:

$$F(\theta) = \frac{AWV_0}{L}(\mathbf{m} \cdot \mathbf{n}_0)^2, \quad (1.32)$$

where θ is the angle between the long axis of the colloid (which in this case coincides with \mathbf{m}) and the far-field director \mathbf{n}_0 . It was assumed that when one considers a ferronematic instead of a single isolated particle the expression in Eq. (1.32) should merely be multiplied by the concentration of the colloidal inclusions and the value of the local director field $\mathbf{n}(\mathbf{r})$ should be used instead of constant \mathbf{n}_0 .

According to the Burylov and Raikher theory the state of the ferronematic is characterized by three spatially varying fields (see Eq. (1.31)): the director $\mathbf{n}(\mathbf{r})$, the magnetization direction $\mathbf{m}(\mathbf{r})$, and the particle concentration $v(\mathbf{r})$. The dependence of the concentration on the spatial coordinate and therefore a possibility to have a nonuniform distribution of the centers of mass of the particles in the sample was first pointed out by Brochard and de Gennes [85]. They called the corresponding effect *segregation*. Segregation occurs when

the coupling of colloids to the liquid crystal does not allow them to align their magnetic moments along the magnetic field. If there is a region of the sample where the nematic director favors the alignment of the particles' magnetic moments along the field it might be energetically favorable for some colloids to migrate in those regions at the expense of the entropic contribution (see the fourth term in Eq. (1.31)).

For a long time the Burylov-Raikher free energy was the main tool in theoretical investigations of ferronematics.

Zaklevnykh [91] considered an infinite ferronematic (not confined by walls). Due to this fact the elastic contribution in Eq. (1.31) can be dropped out. The author considered the case of homeotropic anchoring on the surface of needle-like colloids and the case of positive magnetic anisotropy χ_a of the liquid crystal. Such a setup was then exposed to a magnetic field in the direction parallel to the magnetization. Since χ_a was taken to be positive the nematic director prefers to orient along the external field. On the other hand, the anisotropic anchoring to the colloidal inclusions tends to keep the director perpendicular to the colloids, and therefore, perpendicular to the external magnetic field. The competition between these two phenomena was studied. It was found that depending on the strength of the coupling of the liquid crystal to the colloidal surface and the external field strength, the unbounded ferronematic can adopt three different phases. In the first phase corresponding to the weaker fields, all colloids are aligned along the field and the nematic director is homogeneous and perpendicular to the field. In the second phase corresponding to the intermediate fields, the colloids and the nematic director make two different angles ($\neq 0, \pi/2$) with the external field, creating a so-called “angular phase”. In the third phase corresponding to the high fields, the colloids and the director are aligned with the field, thus the homeotropic anchoring is no longer valid. Zakhlevnykh refers to the switch between the first and second phase as “peculiar Frederiksz-like” transition. The analogy is clear: in the first phase the nematic is undistorted, and there exists a certain value of the external field at which the nematic changes its configuration (although it remains homogeneous, it differs from the initial configuration).

The transitions between the orientational states of an unbounded ferronematic were thoroughly studied in Ref. [92]. The free energy functional used in Ref. [91] was augmented with an important detail: the energy of the coupling of the magnetization field to the director was extended to fourth order in the scalar product $(\mathbf{n} \cdot \mathbf{m})$. It was shown earlier (see Ref. [93]) that the orientational energy of a single anisotropic colloid in an NLC can be expressed as an infinite series of even powers of $\cos \theta$ where θ is the angle that particle's long axis makes with the far-field director. Thus, it was proposed by the authors of Ref. [92] that the theory that includes only the term $\propto (\mathbf{n} \cdot \mathbf{m})^2 = [\cos \theta]^2$ is incomplete and should be extended by at least one more order. Physically, addition of an extra term to the energy of interaction between the magnetization (i.e., the colloids) and the director field

can be interpreted as an attempt to effectively take into account some minor phenomena such as the influence of so far disregarded end effects of the needle (i.e., a thin cylinder), local inhomogeneities of the anchoring surface energy, deviations of the particle shape from a cylinder, local microscopic distortions of the NLC around the particles etc. It turned out that the coefficient in front of the extra fourth order term influences the character (first- or second-order) of the transitions between the phases of the unbounded ferronematic. This coefficient is also responsible for the character of the hysteresis behaviour when the transition is of first order. The authors of Ref. [92] proposed to gain information about that coefficient by observing the type of hysteresis in an experiment.

Zadorozhnii et. al. [94] presented an extension of the work of Zakhlevnykh by confining the nematic between two parallel walls with infinitely strong anchoring. The addition of walls and therefore of a preferred axis of orientation of the liquid crystal in the equilibrium state (without external field) introduces new possibilities for the geometry of the problem under consideration. Indeed, in the infinite nematic considered by Zakhlevnykh the external magnetic field direction had to be specified with respect to the axis along which particles in the suspension have their long axes (i.e. the initial magnetization axis). Under the confinement one essential direction is added to the problem. The behavior of the system now strongly depends on the mutual orientation of the three vectors: a unit vector along the easy axis at the wall (here and in the following only the simplest case of a single non-degenerate easy axis is considered), a unit vector along the initial direction of the long axes of the colloidal inclusions, and the direction of the external magnetic field. The initial configuration that the nematic *planar cell* or *slab* adopts is dictated by the type of anchoring of the liquid crystal at the confining walls and the type of the anchoring of the colloidal particles to the nematic solvent. The authors of Ref. [94] considered a geometry where the nematic is homeotropically anchored to the confining walls and homeotropically anchored to needle-like colloids. Such a setup implies that initially the particles' long axis can freely rotate in the plane that is parallel to the walls. In order to obtain a homogeneously magnetized sample it is required to apply a bias magnetic field along an arbitrary direction that belongs to the said plane. A sample that is prepared in such a way is then exposed to another external magnetic field in the direction perpendicular to the walls. The case of planar anchoring at the walls and particles' surface eliminates the need of the bias field and was considered by the same authors in Ref. [95]. The response of the sample was then investigated numerically as a function of the external field strength and the strength of the coupling between the colloids and the NLC. It was found that the system is capable of exhibiting an "inverse Freederiksz effect": at low fields the nematic is perturbed because it is coupled to the colloidal particles and those rotate in order to minimize their magnetic energy. However there is a critical value of the field above which the distortion vanishes if the coupling between the colloids and the NLC is

weak enough. The system was not investigated for very high fields where the nematic is distorted due to the direct diamagnetic coupling (see the second term in Eq. (1.31)). Comparing the outcome of the investigation of Zakhlevnykh [91] to that of Zadorozhnii et. al. [94] it is evident that the presence of confinement can drastically alter the behavior of the ferronematic and that more complete theories have to include this.

A more complete theoretical investigation was performed by Zakhlevnykh and Petrov [96]. Once again the Burylov-Raikher theory was used as a theoretical tool. The authors of Ref. [96] adopted the geometry used in Ref. [94] and studied the system in the context of the following parameters: the external magnetic field strength, a spatially varying volume fraction of colloidal particles, a so-called segregation parameter, and the coupling of the colloids to the NLC matrix. The assumption of equality of the elastic constants was also lifted and therefore an additional parameter of “elastic anisotropy” (the ratio of splay and bend elastic constants) was introduced. The numerical solution of the corresponding Euler-Lagrange equations showed that in such a geometry the ferronematic undergoes a series of transitions as the external field is increased according to the scheme uniform phase – non-uniform phase – uniform phase – non-uniform phase. The first three phases coincide with those found in Ref. [94] and thus confirm the earlier result. The last “non-uniform phase” is the result of pushing the external magnetic field into the region where the direct diamagnetic coupling of the NLC to the external magnetic field becomes relevant. The important role of segregation effects was pointed out in Ref. [96]. The inclusion of segregation had a particular effect on the character of the transitions, i.e., depending on the value of the segregation parameter transitions may be either first or second order.

A case of a “compensated ferronematic”, where there are on average as many magnetic moments pointing in one direction as there are pointing in the opposite direction, was considered by Zakhlevnykh and Petrov [97]. An interesting property of such a suspension was observed: unlike for the case of a completely magnetized ferronematic sample where the response of the director field appeared in a thresholdless manner, i.e., for arbitrarily small magnetic fields, in the case of a compensated nematic the distortions of the director field arose only upon reaching a certain critical field, i.e., much like in a classic Freederiksz transition. Since macroscopic nematic distortions are easily observable by optical means it was suggested that the presence/absence of a threshold magnetic field could be used as an indicator of whether the sample is magnetized or not.

The Burylov-Raikher theory proved to be a useful theoretical tool for the description of ferronematics. However, being a mesoscopic theory it does not account for the microscopic details of the immediate vicinity of the colloidal particle, i.e., the distortions of the liquid crystal on the scale of the particle size. Such details could in principle be included implicitly by extending the particle-liquid crystal coupling term to higher orders in the scalar product $(\mathbf{n} \cdot \mathbf{m})$ (see Ref. [92]) or, alternatively, by the renormalization of the

prefactor A (see Eq. (1.31)) in front of the aforementioned term [92]. A theory that takes a systematic approach to include the microscopic phenomena has not been established yet.

Moreover, the theoretical work discussed above [91, 92, 93, 94, 95, 96, 97] exclusively deals with essentially the same geometry: the external magnetic field is applied *perpendicular* to the direction of the initial magnetization. Such a geometry has been investigated experimentally [98, 99, 100, 101]. The geometry where the external field is applied parallel and in the direction *opposite* to the initially fully-magnetized (ferromagnetic-like) sample was not considered.

Although it is experimentally feasible to create a suspension of needle-like magnetic particles, such a system suffered from the formation of aggregates for higher magnetic fields or higher volume fractions of the colloidal particles. The aggregation is attributed to the long-ranged Coulomb-like elastic interaction between such needle-like particles. The idea of coating each particle with a surfactant that would provide either a surface charge or a sterically repulsive coat (i.e., a polymer brush) can be considered. However, in case of the surface charge the electric field created in the vicinity of each particle would strongly distort the liquid crystalline medium due to a large electric anisotropy of the NLC (see Sec. 1.1) thus being incompatible with a simplistic theoretical approach. Polymer brushes would both alter the effective shape of each colloid and provide only a short-range repulsion.

A stable suspension was obtained by Mertelj et al. [102], who replaced needle-like colloids with platelets. Platelet-like barium hexaferrite colloidal particles are monodomain magnetic disc-shaped polygons with 3 to 7 sides (see Ref. [102]). The magnetic moment of such a colloid points perpendicular to the plane of the disc. The surface of the colloids was treated to impose a homeotropic boundary condition. A dilute suspension of such platelets in the liquid crystal MBBA was prepared. The sample remained stable over at least several months and no spontaneous aggregation was observed. It was argued that the stability of the colloidal solution was exclusively due to elastic quadrupoles accompanying each particle. Indeed, a disc of finite thickness with homeotropic boundary conditions once placed in a nematic would align its normal to the disc surface parallel to the nematic director and a saturn ring defect would be created in the vicinity of the rim (or “inside” the particle if the anchoring is weak enough). It is known [66] that elastic quadrupoles, much like their electrostatic counterparts, repel when two approach each other along the main axes of the quadrupolar symmetry and attract otherwise. If one adds the dipole-dipole interaction between magnetic moments of the particles for a certain set of parameters (anchoring at the surface, magnetic moment strength, elastic constant, disc thickness) it is possible to get a repulsive overall effective interaction between two discs. However, the small thickness of particles and the low magnitude of their magnetic

moments cast doubt on the suggestion that such interaction would be able to suppress an elastic Coulomb attraction. Therefore, the question of the nature of the stability of the suspension remains open.

It was possible to produce a uniformly magnetized sample if one followed a particular sample preparation protocol: the solid phase (colloidal platelets) was dispersed in the heated up liquid crystal such that the liquid was in the isotropic phase. Then the solution was temperature-quenched into the nematic phase in the presence of a bias magnetic field. The magnetization of such a prepared sample is parallel to the nematic field and remains constant because the free rotation of the platelets is prevented by the nematic. The described protocol is identical to the one proposed in [90]. The authors of Ref. [102] then applied a magnetic field in the direction *antiparallel* to the initial direction of the magnetization and measured the magnitude of the projection of the magnetization of the sample onto the external magnetic field. The observed curve as a function of the magnetic field strength exhibited a hysteresis behavior very much like the corresponding dependence for the case of ferromagnets.

Another important outcome of Ref. [102] is the phenomenological free-energy density that has a form that differs from the form proposed by Burylov and Raikher. The new expression was written as a series in powers of the relevant order parameters, i.e., the magnetization field vector and the nematic director:

$$f_{\text{FN}}^{\text{Me}}(\mathbf{M}, \mathbf{n}) = f_{\text{el}} + \frac{a}{2} |\mathbf{M}(\mathbf{r})|^2 + \frac{b}{4} |\mathbf{M}(\mathbf{r})|^4 - \frac{1}{2} \gamma \mu_0 (\mathbf{M}(\mathbf{r}) \cdot \mathbf{n}(\mathbf{r}))^2 - \mathbf{M}(\mathbf{r}) \cdot \mathbf{B} \quad (1.33)$$

(if one considers only moderate amplitudes of the external magnetic field, i.e., $|\mathbf{B}| < 10^2$ mT, the diamagnetic term (see the second term in Eq. (1.31)) can be disregarded). The phenomenological form in Eq. (1.33) includes the elastic energy of the nematic f_{el} and the coupling of the magnetization field to the external magnetic field (see the last term) similar to the Burylov-Raikher free energy density. The quadratic coupling between the magnetization and the director is also present, however, a *coupling constant* γ is introduced as a prefactor (compare to the last term in Eq. (1.31)). The most obvious difference between the two theories is the addition of even powers of the magnetization \mathbf{M} to the free energy and the absence of the *explicit* dependence on the volume fraction of the colloids in Eq. (1.33). The former and the latter are connected: indeed, the magnetization \mathbf{M} in Eq. (1.33) has dimensions of magnetic moment per volume, unlike the dimensionless vector \mathbf{m} in Eq. (1.31). The *Landau-like* form of the free energy proposed by Mertelj et al. *implicitly* includes the dependence on the spatial distribution of the colloids through the dependence of the absolute value of the magnetization vector \mathbf{M} on the spatial coordinate. Since $|\mathbf{M}(\mathbf{r})|$ is proportional to the density of colloids at point \mathbf{r} the free energy density in Eq. (1.33) contains contributions proportional to the first, second, and fourth power in density (compare to the logarithmic contribution in Eq. (1.31)). Only the second

power of the scalar product ($\mathbf{M} \cdot \mathbf{n}$) is present and the corresponding term is the only place besides f_{el} where the director field enters (even powers of \mathbf{n} would merely provide a constant shift to the energy since $\mathbf{n}^2 = 1$).

The expression in Eq. (1.33) is a *phenomenological* one and therefore the coefficients of the expansion (i.e., a , b , and γ) have to be treated as fitting parameters when compared to experimental data. A reasonable question one can ask is whether the expression similar to the one in Eq. (1.33) could be derived rigorously from a microscopic theory and thus calculate the coefficients of such a Landau-like expansion in terms of microscopic details (material constants, interaction parameters) of the ferronematic.

The present work is aimed at improving the understanding of ferronematics both from the standpoint of fundamental microscopic theory and from the standpoint of mesoscopic behavior of ferronematics in confinement. This twofold approach is motivated by the two problems mentioned above. First of all, we answer the following question: Can one obtain an expression for the free energy density similar to that in Eq. (1.33) from a microscopic statistical-mechanical description? After the corresponding expression is derived we use it to investigate the behavior of ferronematics confined between two parallel and planar walls which impose a nondegenerate easy direction on the NLC. However, unlike studies reported in Refs. [91, 92, 93, 94, 95, 96, 97] in which the external magnetic field was applied *perpendicular* to the direction of initial magnetization, the current study considers the case in which the external magnetic field is applied in the direction *antiparallel* to the direction of initial magnetization. Ferronematics are described by two *vector* fields \mathbf{n} and \mathbf{M} and therefore their behavior strongly depends on the mutual orientation of \mathbf{n} and \mathbf{M} as well as on the orientation of \mathbf{n} and \mathbf{M} relative to external fields (i.e., the magnetic field, confining walls, and the electric field (not considered in the present study)). As a result, the setup studied in the present work is characterized by a qualitatively different behavior compared to the situations that have been discussed in the literature.

The dissertation is organized as follows. Section 2.1 contains a brief derivation of the density functional theory of non-interacting colloids starting from the familiar machinery of statistical mechanics, i.e., the grand canonical distribution function and ensemble averages. The derived density functional is used as a starting point in deriving the effective Landau-like free energy density of ferronematics later on. A mathematical foundation of the conjugate gradient algorithm is presented in Sec. 2.2. This algorithm is relevant in the context of minimization of arbitrary functions and it is used as a numerical tool to study the behavior of ferronematics in confinement. The mesoscopic Landau-like free energy density similar to that in Eq. (1.33) is obtained in Chap. 3. The connection of the coupling constant γ (see Eq. (1.33)) with microscopic parameters of the colloidal suspension (size of the colloids, elastic constant of the NLC, and the coupling of the NLC to the colloidal surface) is established. The behavior of the uniformly magnetized fer-

ronematic slab confined between two planar and parallel walls is studied numerically in Chap. 4. The hysteresis of the magnetization is found and the corresponding critical field is characterized in terms of the coupling constant γ and the strength of the coupling of the NLC to confining walls. We have found two qualitatively different scenarios according to which the slab switches its magnetization between two antiparallel directions. The suitably prepared slab allows one to reversibly switch off its magnetization by applying an external magnetic field of suitable orientation. We conclude and discuss possible directions of further investigations in Chap. 5.

Chapter 2

Methods

2.1 Density Functional Theory

A very successful microscopic theory of fluids is density functional theory (DFT) [103]. Originally, the concept of expressing the energy as a functional of the density distribution of particles was used in the context of variational methods in quantum mechanics, in particular, the energy of many-body system of quantum particles (e.g., electrons) can be expressed in terms of functionals of the electron density [104, 105].

A classical analogue of the quantum DFT was formulated by Evans [103] in the context of inhomogeneous fluids, e.g., in the presence of a liquid-vapour interface. In the following a brief introduction to the method is provided.

Consider a collection of N particles (N can fluctuate, for instance, one can think of a liquid in equilibrium with its vapour) in volume \mathcal{V} and at temperature T . A description of such a system from the point of view of statistical mechanics is carried out within the grand canonical ensemble. Any physical observable \mathcal{O} is, in general, a function of coordinates and momenta of all particles (i.e., $\mathcal{O} = \mathcal{O}(\mathbf{r}_1, \mathbf{r}_2, \dots, \mathbf{r}_N, \mathbf{p}_1, \mathbf{p}_2, \dots, \mathbf{p}_N,) =: \mathcal{O}(\mathbf{r}^N, \mathbf{p}^N)$) and therefore depends on the *microscopic* state of the system. In this sense, an observable \mathcal{O} is a microscopic observable. Its ensemble average $\langle \mathcal{O} \rangle$ is defined as

$$\langle \mathcal{O} \rangle := \text{Tr} [\varrho \mathcal{O}], \quad (2.1)$$

where the trace operator reads

$$\text{Tr} [\mathcal{F}] = \sum_{N=0}^{\infty} \frac{1}{h^{3N} N!} \int d\mathbf{p}^N \int d\mathbf{r}^N \mathcal{F}(\mathbf{r}^N, \mathbf{p}^N). \quad (2.2)$$

The quantity denoted as ϱ in Eq. (2.1) is the grand canonical ensemble probability density

$$\varrho := \frac{1}{\Xi} e^{-\beta(\mathcal{H} - \mu N)} \quad (2.3)$$

where μ is the chemical potential and Ξ is the grand canonical partition function

$$\Xi := \text{Tr} [e^{-\beta(\mathcal{H}-\mu N)}]. \quad (2.4)$$

The grand potential $\Omega = -k_B T \ln \Xi$ is the thermodynamic potential of the grand canonical ensemble.

Consider a system having exactly N particles. The information contained in the full phase space probability density ϱ (see Eq. (2.3)) is excessive when one is concerned with the microscopic structure of the fluid. Let us introduce a reduced phase-space distribution function

$$\varrho_N^{(n)}(\mathbf{r}^n, \mathbf{p}^n) := \frac{N!}{(N-n)!} \frac{1}{h^{3N} N!} \int d\mathbf{p}^{(N-n)} \int d\mathbf{r}^{(N-n)} \varrho(\mathbf{r}^N, \mathbf{p}^N), \quad (2.5)$$

where $\mathbf{r}^n := \mathbf{r}_1, \dots, \mathbf{r}_n$, $\mathbf{r}^{(N-n)} := \mathbf{r}_{(n+1)}, \dots, \mathbf{r}_N$, and $\varrho(\mathbf{r}^N, \mathbf{p}^N) := \exp(-\beta\mathcal{H})/Q_N$ is the canonical distribution and Q_N is canonical partition function. The corresponding product $\varrho_N^{(n)}(\mathbf{r}^n, \mathbf{p}^n) d\mathbf{r}^n d\mathbf{p}^n$ gives the probability to find n particles within the volume element $d\mathbf{r}^n$ with the momenta within the volume element $d\mathbf{p}^n$. There are $N!/[(N-n)!]$ ways to choose a subset of n particles out of N particles *and* assign them with tags $1, 2, \dots, n$ hence the corresponding prefactor in Eq. (2.5) (notice that it is $n!$ times larger than the number of ways to choose n indistinguishable particles from N particles without tagging them, i.e., the binomial coefficient C_N^n).

Assume that the Hamiltonian of the system contains a kinetic energy term $K_N := \sum_{i=1}^N |\mathbf{p}_i|^2 / (2m)$ (assume masses of all particles being equal m), an interaction term $U_N(\mathbf{r}^N) = \sum_{i=1}^N \sum_{j>i}^N u_{ij}(\mathbf{r}_i, \mathbf{r}_j)$, and an external field term $\Phi_N(\mathbf{r}^N) = \sum_{i=1}^N \phi(\mathbf{r}_i)$

$$\mathcal{H}(\mathbf{r}^N, \mathbf{p}^N) = K_N + U_N + \Phi_N. \quad (2.6)$$

Then, the reduced phase-space distribution function $\varrho_N^{(n)}$ can be rewritten as

$$\begin{aligned} \varrho_N^{(n)} &= \frac{N!}{(N-n)!} \frac{1}{h^{3N} N!} \frac{1}{Q_N} \int d\mathbf{p}^{(N-n)} \int d\mathbf{r}^{(N-n)} \exp(-\beta\mathcal{H}) \\ &= \frac{N!}{(N-n)!} \exp\left(-\beta \sum_{i=1}^n \frac{|\mathbf{p}_i|^2}{2m}\right) \frac{1}{Q_N} \times \\ &\quad \times \int d\mathbf{p}^{(N-n)} \int d\mathbf{r}^{(N-n)} \exp\left(-\beta \left(U_N + \sum_{i=n+1}^N \frac{|\mathbf{p}_i|^2}{2m} + \Phi_N\right)\right) \\ &= \frac{N!}{(N-n)!} \frac{\exp\left(-\beta \sum_{i=1}^n \frac{|\mathbf{p}_i|^2}{2m}\right)}{(2\pi m k_B T)^{3n/2}} \int d\mathbf{p}^N \int d\mathbf{r}^{(N-n)} \frac{\exp(-\beta\mathcal{H})}{Q_N} \\ &= \frac{\exp\left(-\beta \sum_{i=1}^n \frac{|\mathbf{p}_i|^2}{2m}\right)}{(2\pi m k_B T)^{3n/2}} \frac{N!}{(N-n)!} \frac{1}{Z_N} \int d\mathbf{r}^{(N-n)} \exp(-\beta(U_N + \Phi_N)) \\ &=: f_M^{(n)}(\mathbf{p}^n) \rho_N^{(n)}(\mathbf{r}^n), \end{aligned} \quad (2.7)$$

where we used the fact that $\int d\mathbf{p} \exp\left(-\beta\frac{|\mathbf{p}|^2}{2m}\right) = (2\pi mk_{\text{B}}T)^{3/2}$ and defined the Maxwellian distribution for n particles $f_{\text{M}}^{(n)}(\mathbf{p}^n)$

$$f_{\text{M}}^{(n)}(\mathbf{p}^n) := \frac{\exp\left(-\beta\sum_{i=1}^n\frac{|\mathbf{p}_i|^2}{2m}\right)}{(2\pi mk_{\text{B}}T)^{3n/2}}, \quad (2.8)$$

and the equilibrium n -particle density $\rho_N^{(n)}(\mathbf{r}^n)$

$$\rho_N^{(n)}(\mathbf{r}^n) := \frac{N!}{(N-n)!} \frac{1}{Z_N} \int d\mathbf{r}^{(N-n)} \exp\left(-\beta(U_N + \Phi_N)\right). \quad (2.9)$$

The quantity Z_N is the configurational integral, i.e., $Z_N := \int d\mathbf{r}^N \exp\left(-\beta(U_N + \Phi_N)\right)$. The n -particle density represents a probability density and therefore the quantity $\rho_N^{(n)}(\mathbf{r}^n) d\mathbf{r}^n$ is the probability to find n particles within the volume $d\mathbf{r}^n$. The particle densities provide all the information about the microscopic structure of the fluid.

Extending the concept of n -particle density to the case of fluctuating N is rather straightforward. Consider the grand canonical probability distribution ϱ (see Eq. (2.3)). The probability $p(N)$ that the system contains exactly N particles is

$$\begin{aligned} p(N) &= \frac{1}{h^{3N}N!} \int d\mathbf{p}^N \int d\mathbf{r}^N \varrho(\mathbf{r}^N, \mathbf{p}^N) \\ &= \frac{1}{\Xi} \frac{\zeta^N}{N!} Z_N, \end{aligned} \quad (2.10)$$

where we introduced the activity $\zeta := \exp(\beta\mu)/\Lambda^3$. Consequently, the n -particle density $\rho^{(n)}(\mathbf{r}^n)$ in the grand canonical ensemble reads

$$\rho^{(n)}(\mathbf{r}^n) := \sum_{N=n}^{\infty} p(N) \rho_N^{(n)}(\mathbf{r}^n) \quad (2.11)$$

or explicitly,

$$\rho^{(n)}(\mathbf{r}^n) = \frac{1}{\Xi} \sum_{N=n}^{\infty} \frac{\zeta^N}{(N-n)!} \int d\mathbf{r}^{(N-n)} \exp\left(-\beta(U_N + \Phi_N)\right). \quad (2.12)$$

Let us prove a rather useful representation of the 1-particle density or *density profile*:

$$\rho(\mathbf{r}) := \rho^{(1)}(\mathbf{r}) = \langle \hat{\rho}(\mathbf{r}) \rangle := \left\langle \sum_{i=1}^N \delta(\mathbf{r} - \mathbf{r}_i) \right\rangle. \quad (2.13)$$

First, write the grand canonical average on the rhs of Eq. (2.13) explicitly:

$$\begin{aligned} \left\langle \sum_{i=1}^N \delta(\mathbf{r} - \mathbf{r}_i) \right\rangle &= \\ \sum_{N=0}^{\infty} \frac{1}{h^{3N}N!} \sum_{i=1}^N \int d\mathbf{p}^N \int d\mathbf{r}^N \frac{1}{\Xi} e^{\beta\mu N} e^{-\beta\mathcal{H}} \delta(\mathbf{r} - \mathbf{r}_i) &= \\ \frac{1}{\Xi} \sum_{N=0}^{\infty} \frac{e^{\beta\mu N}}{\Lambda^{3N}} \frac{1}{N!} \sum_{i=1}^N \int d\mathbf{r}^N e^{-\beta(U_N(\mathbf{r}_1, \dots, \mathbf{r}_N) + \Phi_N(\mathbf{r}_1, \dots, \mathbf{r}_N))} \delta(\mathbf{r} - \mathbf{r}_i) & \end{aligned} \quad (2.14)$$

The integral in the last line of Eq. (2.14) does not change when the index i changes from 1 to N and therefore the sum over i equals N times the integral calculated for a particular value of i , say, $i = 1$:

$$\begin{aligned} \frac{1}{\Xi} \sum_{N=0}^{\infty} \frac{e^{\beta\mu N}}{\Lambda^{3N}} \frac{1}{N!} \sum_{i=1}^N \int d\mathbf{r}^N e^{-\beta(U_N(\mathbf{r}_1, \dots, \mathbf{r}_N) + \Phi_N(\mathbf{r}_1, \dots, \mathbf{r}_N))} \delta(\mathbf{r} - \mathbf{r}_i) = \\ \frac{1}{\Xi} \sum_{N=0}^{\infty} \frac{e^{\beta\mu N}}{\Lambda^{3N}} \frac{N}{N!} \int d\mathbf{r}^{(N-1)} e^{-\beta(U_N(\mathbf{r}, \mathbf{r}_2, \dots, \mathbf{r}_N) + \Phi_N(\mathbf{r}, \mathbf{r}_2, \dots, \mathbf{r}_N))} = \\ \frac{1}{\Xi} \sum_{N=1}^{\infty} \frac{\zeta^N}{(N-1)!} \int d\mathbf{r}^{(N-1)} e^{-\beta(U_N(\mathbf{r}, \mathbf{r}_2, \dots, \mathbf{r}_N) + \Phi_N(\mathbf{r}, \mathbf{r}_2, \dots, \mathbf{r}_N))}, \end{aligned} \quad (2.15)$$

where in going from the second line to the third line in Eq. (2.15) we used the fact that the term corresponding to $N = 0$ is identically zero. Now comparing the last line of Eq. (2.15) and the definition of the the n -particle density in Eq. (2.12) for $n = 1$ it is evident that Eq. (2.13) holds. The relation in Eq. (2.13) allows one to write an expression for the external potential Φ_N that will prove to be useful later. Consider

$$\begin{aligned} \Phi_N(\mathbf{r}_1, \dots, \mathbf{r}_N) &= \sum_{i=1}^N \phi(\mathbf{r}_i) = \sum_{i=1}^N \int d\mathbf{r} \delta(\mathbf{r} - \mathbf{r}_i) \phi(\mathbf{r}) \\ &= \int d\mathbf{r} \hat{\rho}(\mathbf{r}) \phi(\mathbf{r}), \end{aligned} \quad (2.16)$$

and thus the anseble average of the external potential $\langle \Phi_N \rangle$ is related to the density profile:

$$\langle \Phi_N \rangle = \int d\mathbf{r} \langle \hat{\rho}(\mathbf{r}) \rangle \phi(\mathbf{r}) = \int d\mathbf{r} \rho(\mathbf{r}) \phi(\mathbf{r}). \quad (2.17)$$

Next consider an external potential $\phi(\mathbf{r})$ containing a contribution that describes confining walls that surround the system [19]. The volume available to particles then corresponds to a subdomain of \mathbb{R}^3 in which $\phi(\mathbf{r})$ is finite and the change in the volume δV can be identified with the change in the external potential $\delta\phi$. The infitesimal change of the state yields a change in the internal energy E of the system:

$$\delta E = T\delta S + \int d\mathbf{r} \rho(\mathbf{r}) \delta\phi(\mathbf{r}) + \mu\delta N. \quad (2.18)$$

The corresponding change in the free energy $F = E - TS$ of the system then reads

$$\delta F = -S\delta T + \int d\mathbf{r} \rho(\mathbf{r}) \delta\phi(\mathbf{r}) + \mu\delta N. \quad (2.19)$$

It turns out to be useful to define the *intrinsic* free energy \mathcal{F}

$$\mathcal{F} = F - \int d\mathbf{r} \rho(\mathbf{r}) \delta\phi(\mathbf{r}). \quad (2.20)$$

The intrinsic free energy describes the contribution to F that does not explicitly depend on $\phi(\mathbf{r})$. The grand potential $\Omega = F - \langle N \rangle \mu$ equals

$$\Omega = \mathcal{F} + \int d\mathbf{r} \rho(\mathbf{r}) \phi(\mathbf{r}) - \langle N \rangle \mu. \quad (2.21)$$

On the other hand, the quantity $\Omega + \int d\mathbf{r} \rho(\mathbf{r}) \phi(\mathbf{r}) - \langle N \rangle \mu = \Omega + \langle \Phi_N \rangle - \langle N \rangle \mu$ can be expressed as an ensemble average (see Eq. (2.3) and the definition of Ω below Eq. (2.4))

$$\Omega - \langle \Phi_N \rangle + \langle N \rangle \mu = \langle K_N + U_N + k_B T \ln \varrho \rangle = \mathcal{F}, \quad (2.22)$$

where the second equality follows from Eq. (2.21). Since ϱ includes Φ_N and thus $\phi(\mathbf{r})$ it is evident that \mathcal{F} is a *functional* of $\phi(\mathbf{r})$. A much less obvious statement is that $\phi(\mathbf{r})$ is a *unique* functional of the density profile $\rho(\mathbf{r})$ (for a proof of this statement see [103, 19]). Therefore, the intrinsic free energy is a functional of the density profile, i.e., $\mathcal{F} = \mathcal{F}[\rho(\mathbf{r})]$. Then from Eq. (2.21) it follows that

$$\Omega = \mathcal{F}[\rho(\mathbf{r})] + \int d\mathbf{r} \rho(\mathbf{r}) (\phi(\mathbf{r}) - \mu) = \Omega[\rho(\mathbf{r})], \quad (2.23)$$

where we used the fact that $\langle N \rangle = \int d\mathbf{r} \rho(\mathbf{r})$. Consider now a functional Ω_ϕ of an *arbitrary* function $n(\mathbf{r})$

$$\Omega_\phi[n(\mathbf{r})] = \mathcal{F}[n(\mathbf{r})] + \int d\mathbf{r} n(\mathbf{r}) (\phi(\mathbf{r}) - \mu). \quad (2.24)$$

If $n(\mathbf{r}) = \rho(\mathbf{r})$ then Ω_ϕ equals grand potential of the system, i.e.,

$$\Omega_\phi[\rho(\mathbf{r})] = \Omega. \quad (2.25)$$

One can also show that Ω is the minimum of Ω_ϕ , i.e.,

$$\Omega = \Omega_\phi[\rho(\mathbf{r})] = \min_{n(\mathbf{r})} \Omega_\phi[n(\mathbf{r})]. \quad (2.26)$$

Equations (2.25) and (2.26) allow one to formulate the problem of finding the equilibrium density profile $\rho(\mathbf{r})$ for given external potential and particle-particle interactions as a variational problem of finding the function $n(\mathbf{r})$ such that Ω_ϕ is minimized. This amounts to solving the corresponding Euler-Lagrange equation $\left. \frac{\delta \Omega_\phi[n]}{\delta n(\mathbf{r})} \right|_{n(\mathbf{r})=\rho(\mathbf{r})} = 0$.

Finding the equilibrium density profile by minimizing the *grand canonical potential functional* Ω_ϕ by using analytical or numerical schemes is the subject of investigations within classical density functional theory. Unfortunately, the explicit expression for the intrinsic free energy $\mathcal{F}[\rho(\mathbf{r})]$ is generally not known. However, as we will see in Chap. [1ST-ARTICLE] a ferronematic, i.e., a dilute suspension of anisotropic magnetic particles, can be described as an ideal gas in an external field. The expression for the intrinsic free energy of the ideal gas (i.e., for $U_N \equiv 0$) can be obtained analytically.

The partition function of the ideal gas is

$$\begin{aligned}
\Xi_{\text{id}} &= \sum_{N=0}^{\infty} \frac{1}{h^{3N} N!} \int d\mathbf{p}^N \int d\mathbf{r}^N e^{-\beta(K_N(\mathbf{p}^N) + \Phi_N(\mathbf{r}^N) - \mu N)} \\
&= \sum_{N=0}^{\infty} \frac{\zeta^N}{N!} \int d\mathbf{r}_1 \dots d\mathbf{r}_N e^{-\beta \sum_{i=1}^N \phi(\mathbf{r}_i)} \\
&= \sum_{N=0}^{\infty} \frac{\zeta^N}{N!} \prod_{i=1}^N \int d\mathbf{r}_i e^{-\beta \phi(\mathbf{r}_i)} \\
&= \sum_{N=0}^{\infty} \frac{\zeta^N}{N!} \left[\int d\mathbf{r} e^{-\beta \phi(\mathbf{r})} \right]^N \\
&= \exp \left[\zeta \int d\mathbf{r} e^{-\beta \phi(\mathbf{r})} \right],
\end{aligned} \tag{2.27}$$

and thus the grand potential of the ideal gas reads

$$\Omega_{\text{id}} = -k_{\text{B}} T \ln \Xi_{\text{id}} = -k_{\text{B}} T \zeta \int d\mathbf{r} e^{-\beta \phi(\mathbf{r})}. \tag{2.28}$$

Next, let us calculate the corresponding density profile $\rho_{\text{id}}(\mathbf{r})$. According to Eq. (2.12)

$$\begin{aligned}
\rho_{\text{id}}(\mathbf{r}) &= \frac{1}{\Xi} \sum_{N=1}^{\infty} \frac{\zeta^N}{(N-1)!} \int d\mathbf{r}^{(N-1)} e^{-\beta \Phi_N(\mathbf{r}, \mathbf{r}_2, \dots, \mathbf{r}_N)} \\
&= \frac{e^{-\beta \phi(\mathbf{r})}}{\Xi} \sum_{N=1}^{\infty} \frac{\zeta^N}{(N-1)!} \left[\int d\mathbf{r}' e^{-\beta \phi(\mathbf{r}')} \right]^{N-1} \\
&= \zeta \frac{e^{-\beta \phi(\mathbf{r})}}{\Xi} \sum_{M=0}^{\infty} \frac{\zeta^M}{M!} \left[\int d\mathbf{r}' e^{-\beta \phi(\mathbf{r}')} \right]^M \\
&= \zeta \frac{e^{-\beta \phi(\mathbf{r})}}{\Xi} \Xi \\
&= \zeta e^{-\beta \phi(\mathbf{r})}
\end{aligned} \tag{2.29}$$

which is the well-known barometric law. It then follows (see Eq. (2.28) and the last line of Eq. (2.29)) that

$$\Omega_{\text{id}} = -k_{\text{B}} T \int d\mathbf{r} \rho_{\text{id}}(\mathbf{r}). \tag{2.30}$$

Recall the expression of the intrinsic free energy \mathcal{F} as an ensemble average (see Eq. (2.22))

$$\begin{aligned}
\mathcal{F}_{\text{id}} &= \Omega_{\text{id}} - \langle \Phi_N \rangle + \langle N \rangle \mu \\
&= \int d\mathbf{r} [-k_{\text{B}} T \rho_{\text{id}}(\mathbf{r}) - \rho_{\text{id}}(\mathbf{r}) \phi(\mathbf{r}) + \mu \rho_{\text{id}}(\mathbf{r})] \\
&= \int d\mathbf{r} [-k_{\text{B}} T \rho_{\text{id}}(\mathbf{r}) - \rho_{\text{id}}(\mathbf{r}) (\mu - k_{\text{B}} T \ln (\Lambda^3 \rho_{\text{id}}(\mathbf{r}))) + \mu \rho_{\text{id}}(\mathbf{r})] \\
&= k_{\text{B}} T \int d\mathbf{r} \rho_{\text{id}}(\mathbf{r}) [\ln (\Lambda^3 \rho_{\text{id}}(\mathbf{r})) - 1] \\
&= \mathcal{F}_{\text{id}}[\rho_{\text{id}}(\mathbf{r})],
\end{aligned} \tag{2.31}$$

where in order to go from the second line to the third line we used Eq. (2.29).

Finally, the grand potential functional in the case of noninteracting particles that are subject to an external potential ϕ is

$$\Omega_\phi[n(\mathbf{r})] = \mathcal{F}_{\text{id}}[n(\mathbf{r})] + \int d\mathbf{r} n(\mathbf{r})(\phi(\mathbf{r}) - \mu). \quad (2.32)$$

In this study we consider anisotropic colloidal particles and therefore the density profile naturally depends not only on the spatial coordinate \mathbf{r} but also on the orientation of the colloid $\boldsymbol{\omega}$, i.e., $\rho(\mathbf{r}) \rightarrow \rho(\mathbf{r}, \boldsymbol{\omega})$. The analytical results presented in this chapter hold. (Formally one can replace the spatial coordinate \mathbf{r} with the “generalized coordinate” $(\mathbf{r}, \boldsymbol{\omega})$ for each particle. Integrals over the spatial coordinate run over the volume \mathcal{V} while integrals over $\boldsymbol{\omega}$ run over the unit sphere, i.e., $\int d\boldsymbol{\omega} := \int_0^{2\pi} d\varphi \int_0^\pi d\theta \sin\theta$.)

2.2 Conjugate gradient method

A problem of finding a (meta)stable state of the system can be formulated as a problem of finding a (local) minimum of the appropriate energy functional $F[x]$ where x denotes all fields F depends on. Analytical solution of the corresponding Euler-Lagrange equation $\delta F/\delta x = 0$ is often unavailable due to the nonlinearities. From a numerical point of view, one has to deal with discrete quantities and therefore the discretized representation of F on some grid is necessary. Once the problem is reformulated in terms of the discretized functional only the finite number N (where N is the number of grid points) of unknowns remains and hence one can think of a *function* $F(\mathbf{x})$ of an N -dimensional vector $\mathbf{x} = (x_0, x_1, \dots, x_{N-1})^T \in \mathbb{R}^N$.

Numerical methods that deal with the minimization of a general function $F(\mathbf{x})$ can be divided in two main groups: those that do not require the analytical expression for the gradient ∇F and those that do. The former group includes methods such as the downhill simplex method [106], Powell’s method of conjugate directions [107] and its derivative due to Brent [108]. Two major representatives of methods that utilize the knowledge of the gradient are quasi-Newton methods [109, 110] and the conjugate gradient method. In this section a brief mathematical description of the latter is presented.

The gradient $\nabla F(\mathbf{x}^*)$ corresponds to the direction at point x^* in which the function F increases most rapidly. Thus, the simplest algorithm that aims at finding a minimum of a function in the vicinity of a point can be constructed as follows: Choose a starting point \mathbf{x}_0 and move along the direction $-\nabla F(\mathbf{x}_0)$ till the minimum in that direction is found. In other words, find a point \mathbf{x}_1 such that

$$\begin{aligned} \mathbf{x}_1 &= \mathbf{x}_0 - \alpha_0 \nabla F(\mathbf{x}_0) \\ F(\mathbf{x}_1) &= \min_{\alpha_0} F(\mathbf{x}_0 - \alpha_0 \nabla F(\mathbf{x}_0)). \end{aligned} \quad (2.33)$$

Writing the second line of Eq. (2.33) explicitly gives the condition for finding point \mathbf{x}_1

$$\nabla F(\mathbf{x}_1) \cdot \nabla F(\mathbf{x}_0) = 0. \quad (2.34)$$

The algorithm proceeds according to the recurrent scheme:

$$\begin{aligned} \mathbf{x}_{i+1} &= \mathbf{x}_i - \alpha_i \nabla F(\mathbf{x}_i) \\ \alpha_i &: \nabla F(\mathbf{x}_{i+1}) \cdot \nabla F(\mathbf{x}_i) = 0, \end{aligned} \quad (2.35)$$

i.e., each new approximation \mathbf{x}_{i+1} of the minimum point \mathbf{x}^* is obtained by making a step along the negative gradient at point \mathbf{x}_i until the gradient at point \mathbf{x}_{i+1} is perpendicular to the direction along which the current step is made. The described scheme is known as *steepest descent* (or *gradient descent*). The simplicity of steepest descent comes with a significant drawback. Since each new step has to be perpendicular to the previous one the algorithm struggles in a particular (but not uncommon) case: when the minimum lies at the bottom of a long and narrow “valley” the algorithm tends to bounce back between the walls of the valley which results in a relatively slow convergence.

Alternative approaches use smarter choices of directions along which one makes steps on each iteration. Assume that the starting point is sufficiently close to the minimum. Then, function $F(\mathbf{x})$ can be approximated by its Taylor series up to a quadratic order, i.e., $F(\mathbf{x})$ is approximated by a quadratic form

$$F(\mathbf{x}) \approx \frac{1}{2} \mathbf{x} \cdot A \mathbf{x} - \mathbf{b} \cdot \mathbf{x} + c, \quad (2.36)$$

where A is a Hessian matrix, i.e., $A_{ij} = \frac{\partial^2 F}{\partial x_i \partial x_j}$, $\mathbf{b} \in \mathbb{R}^N$, and c is a scalar. The Hessian matrix A is symmetric, i.e., $A^T = A$, moreover a local minimum is assumed so A is positive definite.

The quadratic form in Eq. (2.36) is minimized at point \mathbf{x}^* , therefore the gradient vanishes at \mathbf{x}^*

$$\nabla F(\mathbf{x}^*) = \frac{1}{2} (A^T \mathbf{x}^* + A \mathbf{x}^*) - \mathbf{b} = A \mathbf{x}^* - \mathbf{b} = 0 \quad (2.37)$$

and therefore at point \mathbf{x}^* the following relation holds

$$A \mathbf{x}^* = \mathbf{b}. \quad (2.38)$$

The *error* $\mathbf{e}_i := \mathbf{x}_i - \mathbf{x}^*$ shows how far one is from the true minimum \mathbf{x}^* on i th iteration. The *residual* $\mathbf{r}_i := \mathbf{b} - A \mathbf{x}_i = -A \mathbf{e}_i$ shows how far one is from the solution (\mathbf{b}) in the space of A -transformed vectors ($A \mathbf{x}_i$). Clearly, the residual \mathbf{r}_i equals the negative gradient of F at point \mathbf{x}_i

$$\mathbf{r}_i = -\nabla F(\mathbf{x}_i). \quad (2.39)$$

The *method of conjugate directions* utilizes the idea that one can choose a basis in \mathbb{R}^N and starting from arbitrary point one can on each step move along one of the directions

till the corresponding component of the difference $\mathbf{x}_i - \mathbf{x}^* = \mathbf{e}_i$ is eliminated. (Think, for example, of a person that moves towards a particular intersection. It is a good idea to move along one street till the person “aligns” with the desired destination point. Arriving to the destination would require movement *only* along the second direction). Analogous to Eq. (2.33) one can show that the minimum of F along an *arbitrary* direction \mathbf{u} is perpendicular to the gradient of F calculated in the point where the minimum along the direction is achieved, i.e.,

$$\begin{aligned}\mathbf{x}_{i+1} &= \mathbf{x}_i - \gamma_i \mathbf{u}_i \\ F(\mathbf{x}_{i+1}) &= \min_{\gamma_i} F(\mathbf{x}_i - \gamma_i \mathbf{u})\end{aligned}\tag{2.40}$$

$$\implies \nabla F(\mathbf{x}_{i+1}) \cdot \mathbf{u} = 0.\tag{2.41}$$

We require that the corresponding set of directions possesses the following property: each successive step in the corresponding direction should “respect” the minimizations made on the previous steps. Mathematically it means that upon moving along some *different* direction \mathbf{v} the orthogonality Eq. (2.41) should hold. In other words, the change in the gradient upon moving along \mathbf{v} should be orthogonal to \mathbf{u} , i.e.,

$$\begin{aligned}0 &= \delta (\nabla F(\mathbf{x}_{i+1}) \cdot \mathbf{u}) \\ &= \delta (\nabla F(\mathbf{x}_{i+1})) \cdot \mathbf{u} \\ &= \delta (A(\mathbf{x}_{i+1} + \gamma_{i+1} \mathbf{v}) - \mathbf{b}) \cdot \mathbf{u} \\ &= \mathbf{u} \cdot A\mathbf{v}.\end{aligned}\tag{2.42}$$

Vector \mathbf{v} is said to be A -orthogonal or *conjugate* to \mathbf{u} if $\mathbf{u} \cdot A\mathbf{v} = 0$. If A is symmetric then $\mathbf{u} \cdot A\mathbf{v} = \mathbf{v} \cdot A\mathbf{u}$. A set of vectors that are pairwise conjugate is a conjugate set. Minimizing the quadratic form in Eq. (2.36) using a direction from a conjugate set preserves the minimization made along other members of that set, thus, one need to minimize along each direction only once.

The *Gram-Schmidt conjugation algorithm* allows one to construct a conjugate set $\{\mathbf{d}_k\}_{k=0}^{N-1}$ from an arbitrary basis $\{\mathbf{u}_k\}_{k=0}^{N-1}$ according to the following scheme:

$$\begin{aligned}\mathbf{d}_0 &= \mathbf{u}_0 \\ \mathbf{d}_i &= \mathbf{u}_i + \sum_{k=0}^{i-1} \beta_{ik} \mathbf{d}_k, \quad i > 0.\end{aligned}\tag{2.43}$$

To find the expression for coefficients β_{ik} it is helpful to multiply Eq. (2.43) by $\mathbf{d}_j A$, $j < i$

from the left

$$\begin{aligned}
0 &= \mathbf{d}_j \cdot \mathbf{A}\mathbf{d}_i = \mathbf{d}_j \cdot \mathbf{A}\mathbf{u}_i + \sum_{k=0}^{i-1} \beta_{ik} \mathbf{d}_j \cdot \mathbf{A}\mathbf{d}_k, \quad j < i \\
&= \mathbf{d}_j \cdot \mathbf{A}\mathbf{u}_i + \sum_{k=0}^{i-1} \beta_{ik} \delta_{jk} \mathbf{d}_j \cdot \mathbf{A}\mathbf{d}_j \\
&= \mathbf{d}_j \cdot \mathbf{A}\mathbf{u}_i + \beta_{ij} \mathbf{d}_j \cdot \mathbf{A}\mathbf{d}_j \\
\implies \beta_{ij} &= -\frac{\mathbf{d}_j \cdot \mathbf{A}\mathbf{u}_i}{\mathbf{d}_j \cdot \mathbf{A}\mathbf{d}_j} = -\frac{\mathbf{u}_i \cdot \mathbf{A}\mathbf{d}_j}{\mathbf{d}_j \cdot \mathbf{A}\mathbf{d}_j},
\end{aligned} \tag{2.44}$$

where the conjugacy of \mathbf{d} vectors was used.

Performing the minimization of the quadratic form in Eq. (2.36) with the help of the conjugate set $\{\mathbf{d}_k\}_{k=0}^{N-1}$ amounts to making exactly N steps of the kind

$$\mathbf{x}_{i+1} = \mathbf{x}_i + \gamma_i \mathbf{d}_i. \tag{2.45}$$

The step size γ_i can be found from the requirement that $F(\mathbf{x}_{i+1})$ is minimized, i.e.,

$$\begin{aligned}
\frac{d}{d\gamma_i} F(\mathbf{x}_{i+1}) &= \frac{d}{d\gamma_i} \left[\frac{1}{2} (\mathbf{x}_i + \gamma_i \mathbf{d}_i) \mathbf{A} (\mathbf{x}_i + \gamma_i \mathbf{d}_i) - \mathbf{b} (\mathbf{x}_i + \gamma_i \mathbf{d}_i) + c \right] \\
&= \mathbf{x}_i \cdot \mathbf{A}\mathbf{d}_i + \gamma_i \mathbf{d}_i \cdot \mathbf{A}\mathbf{d}_i - \mathbf{b} \cdot \mathbf{d}_i \\
&= 0
\end{aligned} \tag{2.46}$$

whence

$$\gamma_i = \frac{(\mathbf{b} - \mathbf{A}\mathbf{x}_i) \cdot \mathbf{d}_i}{\mathbf{d}_i \cdot \mathbf{A}\mathbf{d}_i} = \frac{\mathbf{r}_i \cdot \mathbf{d}_i}{\mathbf{d}_i \cdot \mathbf{A}\mathbf{d}_i}. \tag{2.47}$$

An expression analogous to Eq. (2.41) is

$$\mathbf{r}_{i+1} \cdot \mathbf{d}_i = 0, \tag{2.48}$$

or equivalently

$$\mathbf{d}_i \cdot \mathbf{A}\mathbf{e}_{i+1} = 0. \tag{2.49}$$

Since every step of the algorithm brings it closer to the true solution \mathbf{x}^* it is reasonable to say that the corresponding initial error $\mathbf{e}_0 = \mathbf{x}_0 - \mathbf{x}^*$ loses a component along the corresponding direction \mathbf{d}_k after the k th step. To show that, let us expand \mathbf{e}_0 in the basis $\{\mathbf{d}_k\}_{k=0}^{N-1}$:

$$\mathbf{e}_0 = \sum_{j=0}^{N-1} \delta_j \mathbf{d}_j. \tag{2.50}$$

The expansion coefficients δ_j can be found by multiplying \mathbf{e}_0 by $\mathbf{d}_k \mathbf{A}$ from the left and using the conjugacy of \mathbf{d} basis. The result is

$$\delta_k = \frac{\mathbf{d}_k \cdot \mathbf{A}\mathbf{e}_0}{\mathbf{d}_k \cdot \mathbf{A}\mathbf{d}_k}, \tag{2.51}$$

where now using the conjugacy one more time one can rewrite it as

$$\begin{aligned}\delta_k &= \frac{\mathbf{d}_k \cdot A \left(\mathbf{e}_0 + \sum_{i=0}^{k-1} \gamma_i \mathbf{d}_i \right)}{\mathbf{d}_k \cdot A \mathbf{d}_k} \\ &= \frac{\mathbf{d}_k \cdot A \mathbf{e}_k}{\mathbf{d}_k \cdot A \mathbf{d}_k},\end{aligned}\tag{2.52}$$

where obviously

$$\mathbf{e}_0 + \sum_{i=0}^{k-1} \gamma_i \mathbf{d}_i = \mathbf{x}_0 + \gamma_0 \mathbf{d}_0 + \gamma_1 \mathbf{d}_1 + \dots + \gamma_{k-1} \mathbf{d}_{k-1} - \mathbf{x}^* = \mathbf{x}_k - \mathbf{x}^* = \mathbf{e}_k\tag{2.53}$$

Recalling the expression for the residual $\mathbf{r}_k = -A\mathbf{e}_k$ and Eq. (2.47) it is evident that $\gamma_i = -\delta_i$ and thus

$$\mathbf{e}_i = \sum_{k=i}^{N-1} \delta_k \mathbf{d}_k\tag{2.54}$$

and therefore after the i th iteration error \mathbf{e}_i has nonzero components only in the subspace spanned by the subset $\{\mathbf{d}_k\}_{k=i}^{N-1}$. Accordingly,

$$\mathbf{r}_i = -A\mathbf{e}_i = -\sum_{k=i}^{N-1} \delta_k A\mathbf{d}_k\tag{2.55}$$

and

$$\mathbf{d}_j \cdot \mathbf{r}_i = -\sum_{k=i}^{N-1} \delta_k \mathbf{d}_j \cdot A\mathbf{d}_k\tag{2.56}$$

$$= 0, \text{ for } j < i.\tag{2.57}$$

One more relation that will be used later has to be derived. Multiplying the second line of Eq. (2.43) by \mathbf{r}_i yields

$$\begin{aligned}\mathbf{d}_i \cdot \mathbf{r}_i &= \mathbf{u}_i \cdot \mathbf{r}_i + \sum_{k=0}^{i-1} \beta_{ik} \mathbf{d}_k \cdot \mathbf{r}_i \\ &= \mathbf{u}_i \cdot \mathbf{r}_i - \sum_{k=0}^{i-1} \beta_{ik} \mathbf{d}_k \cdot \sum_{p=i}^{N-1} \delta_p A\mathbf{d}_p\end{aligned}\tag{2.58}$$

$$\implies \mathbf{d}_i \cdot \mathbf{r}_i = \mathbf{u}_i \cdot \mathbf{r}_i,$$

where we used that the scalar products of the vectors within the summation signs in the second line are all zero.

The results in Eqs. (2.44), (2.47), and (2.57) motivate the choice $\mathbf{u}_i = \mathbf{r}_i$, $i \in \{0, 1, \dots, N-1\}$. Indeed, from Eqs. (2.43) and (2.57) it follows that the residual \mathbf{r}_i is orthogonal to the previous search directions and therefore to the previous residuals, i.e.,

$$\mathbf{r}_i \cdot \mathbf{r}_j = \delta_{ij},\tag{2.59}$$

which allows one to simplify the Gram-Schmidt algorithm (see Eqs. (2.43) and (2.44)). In order to see that let us first derive a recurrent expression for the residuals

$$\begin{aligned}
\mathbf{r}_{j+1} &= -A\mathbf{e}_{j+1} \\
&= -A(\mathbf{x}_{j+1} - \mathbf{x}^*) \\
&= -A(\mathbf{x}_j + \gamma_j \mathbf{d}_j - \mathbf{x}^*) \\
&= -A(\mathbf{e}_j + \gamma_j \mathbf{d}_j) \\
&= \mathbf{r}_j - \gamma_j A\mathbf{d}_j.
\end{aligned} \tag{2.60}$$

Multiplying the result of Eq. (2.60) by \mathbf{r}_i yields

$$\begin{aligned}
\mathbf{r}_i \cdot \mathbf{r}_{j+1} &= \mathbf{r}_i \cdot \mathbf{r}_j - \gamma_j \mathbf{r}_i \cdot A\mathbf{d}_j \\
\implies \gamma_j \mathbf{r}_i \cdot A\mathbf{d}_j &= \mathbf{r}_i \cdot \mathbf{r}_j - \mathbf{r}_i \cdot \mathbf{r}_{j+1} \\
\implies \mathbf{r}_i \cdot A\mathbf{d}_j &= \begin{cases} \frac{1}{\gamma_i} \mathbf{r}_i \cdot \mathbf{r}_i, & i = j \\ -\frac{1}{\gamma_{i-1}} \mathbf{r}_i \cdot \mathbf{r}_i, & i = j + 1 \\ 0, & \text{otherwise.} \end{cases}
\end{aligned} \tag{2.61}$$

Consequently, all but one coefficients of the expansion in the Gram-Schmidt algorithm β_{ik} (see Eq. (2.44)) drop out:

$$\begin{aligned}
\beta_{ij} &= -\frac{\mathbf{r}_i \cdot A\mathbf{d}_j}{\mathbf{d}_j \cdot A\mathbf{d}_j} \\
&= \begin{cases} \frac{1}{\gamma_{i-1}} \frac{\mathbf{r}_i \cdot \mathbf{r}_i}{\mathbf{d}_{i-1} \cdot A\mathbf{d}_{i-1}}, & i = j + 1 \\ 0, & i > j + 1, \end{cases}
\end{aligned} \tag{2.62}$$

and thus the β -coefficients depend only on one index, i.e, $\beta_{ij} = \beta_{i,i-1} := \beta_i$. Simplifying further

$$\begin{aligned}
\beta_i &= \frac{1}{\gamma_{i-1}} \frac{\mathbf{r}_i \cdot \mathbf{r}_i}{\mathbf{d}_{i-1} \cdot A\mathbf{d}_{i-1}} \\
&= \frac{\mathbf{d}_{i-1} \cdot A\mathbf{d}_{i-1}}{\mathbf{r}_{i-1} \cdot \mathbf{d}_{i-1}} \frac{\mathbf{r}_i \cdot \mathbf{r}_i}{\mathbf{d}_{i-1} \cdot A\mathbf{d}_{i-1}} \\
&= \frac{\mathbf{r}_i \cdot \mathbf{r}_i}{\mathbf{r}_{i-1} \cdot \mathbf{d}_{i-1}} \\
&= \frac{\mathbf{r}_i \cdot \mathbf{r}_i}{\mathbf{r}_{i-1} \cdot \mathbf{r}_{i-1}},
\end{aligned} \tag{2.63}$$

where in going from the third to the fourth line Eq. (2.58) was used. The resulting

algorithm can be summarized as

$$\begin{aligned}
\mathbf{d}_0 &= \mathbf{r}_0 = \mathbf{b} - A\mathbf{x}_0 \\
\gamma_i &= \frac{\mathbf{r}_i \cdot \mathbf{r}_i}{\mathbf{d}_i \cdot A\mathbf{d}_i} \\
\mathbf{x}_{i+1} &= \mathbf{x}_i + \gamma_i \mathbf{d}_i \\
\mathbf{r}_{i+1} &= \mathbf{r}_i - \gamma_i A\mathbf{d}_i \\
\beta_{i+1} &= \frac{\mathbf{r}_{i+1} \cdot \mathbf{r}_{i+1}}{\mathbf{r}_i \cdot \mathbf{r}_i} \\
\mathbf{d}_{i+1} &= \mathbf{r}_{i+1} + \beta_i \mathbf{d}_i,
\end{aligned} \tag{2.64}$$

which is the *conjugate gradient algorithm*. The major improvement compared to the more general method of conjugated directions is that it is not necessary to store the entire sets of vectors $\{\mathbf{r}_k\}_{k=0}^{N-1}$ and $\{\mathbf{d}_k\}_{k=0}^{N-1}$ thus significantly reducing the storage required. Computational effort-wise each iteration contains 1 matrix-vector multiplication and 3 scalar products of two vectors. The algorithm finds the minimum of the quadratic form (2.36) in N steps.

Applying the algorithm described above to the minimization of general functions requires a few comments. First of all, the residual \mathbf{r}_i is replaced by the value of the negative gradient $-\nabla F(\mathbf{x}_i)$ at point \mathbf{x}_i . Moreover, one does not usually know the hessian matrix A and its numerical evaluation using finite differences of first derivatives of F can be inaccurate and time-consuming. Fortunately, the issue is solved easily. According to Eq. (2.46) point \mathbf{x}_{i+1} corresponds to the minimum of F along \mathbf{d}_i . Suppose that instead of using the third line of Eq. (2.64) directly one minimizes the function F *numerically* along the direction \mathbf{d}_i starting from the point \mathbf{x}_i . Assume that the corresponding minimum is obtained in some point \mathbf{x}_{i+1} . It is not surprising that setting $\mathbf{r}_{i+1} = -\nabla F(\mathbf{x}_{i+1})$ yields the vector that is the same as that one would get if the algorithm Eq. (2.64) would have been followed directly. Indeed,

$$\begin{aligned}
\nabla F(\mathbf{x}_{i+1}) &= A\mathbf{x}_{i+1} - \mathbf{b} \\
&= A\mathbf{x}_i + \gamma_i A\mathbf{d}_i - \mathbf{b} \\
&= \nabla F(\mathbf{x}_i) + \gamma_i A\mathbf{d}_i \\
\implies \mathbf{r}_{i+1} &= \mathbf{r}_i - \gamma_i A\mathbf{d}_i.
\end{aligned} \tag{2.65}$$

(compare the last line of Eq. (2.65) and the fourth line of Eq. (2.64).)

The described algorithm performs the search of the local minimum of a general function of N variables given a starting point and given an algorithm of a one-dimensional line minimization (Brent's method [108] augmented with the knowledge of the first derivatives [111] is implemented in this work) is the Fletcher-Reeves algorithm .

Polak and Ribiere introduced a small change [111, 113] into the calculation of coeffi-

icients β_i (see the fifth line of Eq. (2.64)). The new formula reads

$$\beta_{i+1} = \frac{(\mathbf{r}_{i+1} - \mathbf{r}_i) \cdot \mathbf{r}_{i+1}}{\mathbf{r}_i \cdot \mathbf{r}_i}, \quad (2.66)$$

and it is equal to β_{i+1} calculated according to Eq. (2.64) for exact quadratic forms (see Eq. (2.36)) due to Eq. (2.59). However, for the general function the quadratic form in Eq. (2.36) is only an approximation and $\mathbf{r}_i \cdot \mathbf{r}_{i+1} \neq 0$ can be true. The adjustment in Eq. (2.66) helps to “restart” [111] the algorithm when the conjugacy of the set $\{\mathbf{d}_k\}_{k=0}^{N-1}$ is lost due to the numerical errors and due to the difference of the function from the exact quadratic form.

Chapter 3

Effective Landau theory of ferronematics

An effective Landau-like description of ferronematics, i.e., suspensions of magnetic colloidal particles in a nematic liquid crystal (NLC), is developed in terms of the corresponding magnetization and nematic director fields. The study is based on a microscopic model and on classical density functional theory. Ferronematics are susceptible to weak magnetic fields and they can exhibit a ferromagnetic phase, which has been predicted several decades ago and which has recently been found experimentally. Within the proposed effective Landau theory of ferronematics one has quantitative access, e.g., to the coupling between the magnetization of the magnetic colloids and the nematic director of the NLC. On mesoscopic length scales this generates complex response patterns.

3.1 Introduction

The quest for soft matter systems which exhibit spontaneous symmetry breaking in terms of a polar order parameter, analogous to ferromagnetism in solids, has a long history. The first class of systems investigated under this perspective are suspensions of magnetic nanoparticles in simple liquids, which exhibit particularly rich structural and dynamical properties generated by the intricacies of the dipolar character of their basic mutual interactions [114, 115, 116, 117, 118, 119, 120, 121, 122, 123]. Moreover, they offer a broad range of application prospectives such as in medicine [124, 126, 125] and technology [127, 128, 129, 130]. However, whereas such ferrofluids, i.e., colloidal suspensions of magnetic particles in isotropic liquids, display fascinating behaviors in the presence of an external magnetic field, actual systems exhibit only zero net magnetization once the external field is switched off, i.e., there is no occurrence of spontaneous symmetry breaking [131, 132, 133, 134] unless the packing fraction of the colloids is high [135].

A class of soft matter systems, which are indeed able to exhibit nonzero net magne-

tization even in the absence of an external magnetic field, are ferronematics, i.e., *dilute* suspensions of magnetic colloidal particles in anisotropic liquids, such as a nematic liquid crystal (NLC). Whereas this type of system has been studied theoretically almost half a century ago [85], its experimental realization has been achieved only recently [102]. The remarkable property of ferronematics is caused by the broken rotational symmetry of the solvent which implies that the colloids prefer certain orientations with respect to the nematic director, thus restricting their individual magnetic moments to certain directions.

Alternatively, it may be conceivable to suspend colloidal particles with an *electric* instead of a *magnetic* dipole moment in an NLC and to study their properties in external *electric* instead of *magnetic* fields (see Refs. [136, 137] and references therein). However, in contrast to the case of magnetic colloidal particles and magnetic fields, strong distortions of the NLC are expected to occur in the electric analogue, because colloidal particles with electric dipoles strongly polarize their liquid crystalline environment [138], and the molecules of the NLC are highly susceptible to external electric fields, too [33]. Hence it appears advantageous to focus on ferronematics instead of the more complicated suspensions of colloidal particles with electric dipole moments in an NLC.

Exploiting the full range of properties of ferronematics requires a reliable theoretical description which allows one to infer the mesoscopic structures formed by these colloidal suspensions from microscopic molecular properties of the liquid crystalline and colloidal materials. The first such theory was established by Brochard and de Gennes in their pioneering work [85], where the case of infinitely strong anchoring of the liquid crystal to the surface of magnetic colloids was considered, which implies that the direction of the magnetization at each point of the sample should be parallel to the nematic director. Later on it was observed that *soft* and not infinite anchoring is realized in experiments and that the magnetization is not necessarily tightly bound to the director. Burylov and Raikher constructed the theory of ferronematics with soft anchoring [90] in a way analogous to the Brochard-de Gennes approach. An important result of Ref. [90] is an expression for the free energy density of ferronematics which depends on three spatially varying fields: the volume fraction of rod-like magnetic colloids, the local magnetization direction, and the nematic director field. The Burylov-Raikher theory was later extended to include saddle-splay distortions of the nematic and an extra term proportional to the fourth power of the scalar product between the magnetization and the director [93]. An alternative approach was suggested by Mertelj et. al [102], who have proposed a phenomenological form of such a free energy density in terms of the local magnetization field and the local nematic director field. Here, a similar form of the free energy density is derived by starting, however, from a microscopic model. This microscopic approach enables one to relate the corresponding expansion coefficients of the free energy to material properties of the colloids and of the liquid crystal. In order to achieve this goal, a microscopic description of the

interaction between a single colloidal particle and the surrounding liquid is considered. As an illustration the focus is on a simplified model of a single circular disc-shaped colloidal particle suspended in an NLC. Here, the quantity of interest is the free energy as a function of the particle orientation with respect to the nematic director far away from the colloid. The theory is formulated in terms of a dimensionless *coupling constant* c , which is proportional to the particle size and which is small ($c < 0.1$) for the colloids used in the experiment reported in Ref. [102] (platelet radius ≈ 35 nm). Here, analytical expressions of the perturbations of the nematic director profile up to first order and of the corresponding free energy up to second order in the coupling parameter c are derived (Sec. 3.2.2 and Appendix A). Numerical calculations are used in order to assess the accuracy of the proposed perturbation expansion. In contrast to the approach adopted in Refs. [85, 90, 93], here the nematic director field is not approximated by its far-field asymptotics.

This microscopic expression for the free energy of a single colloidal particle in an NLC can be interpreted from the mesoscopic point of view as an external one-particle potential the NLC medium exerts onto each colloid. This one-particle potential can be incorporated into a classical density functional description of a fluid of magnetic discs suspended in the NLC. In agreement with the experimental set-up in Ref. [102], the present work is restricted to the case of dilute colloidal suspensions, which allows one to neglect the effective interactions between two colloidal particles in order to gain calculational advantages. The resulting mesoscopic free energy density is a second degree polynomial of the local magnetization $\mathbf{M}(\mathbf{r})$ and of the local nematic director $\mathbf{n}(\mathbf{r})$ (Sec. 3.2.3 and Appendix B) which can be directly compared with the corresponding form proposed in Ref. [102].

The chapter is organized as follows. In Sec. 3.2 (see also the Appendices A and B) the mathematical models are introduced in order to be able to investigate the effective one-particle potential of a single, thin disc (i.e., a disc of thickness much smaller than its radius such that the interaction of the rim with the NLC medium can be disregarded) immersed in the NLC and to establish a mesoscopic theory of a dilute ferronematic. In Sec. 3.3 the results of a numerical assessment of the proposed effective one-particle potential are presented and the free-energy functional of a ferronematic as derived here is compared with the one proposed in Ref. [102]. Conclusions and final remarks are given in Sec. 3.4.

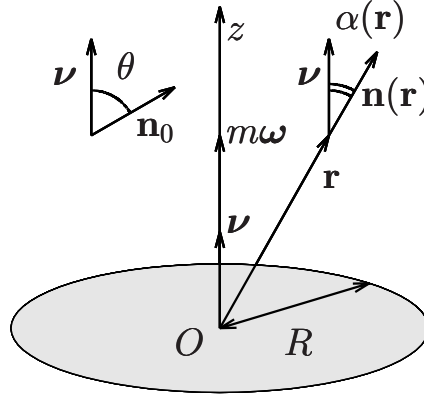


Figure 3.1: Frame of reference used in the calculation of the free energy of a single colloidal disc immersed in an NLC. A thin disc of radius R and negligible thickness is placed with its center in the origin O and is oriented with its normal ν parallel to the z -axis, i.e., the outer normal to the surface of the disc is denoted as ν . A point magnetic dipole of magnitude m and direction $\omega \parallel \nu$ is placed in the center of the disc. The angle between the disc normal ν and the far-field director \mathbf{n}_0 is denoted as θ , whereas the angle between the disc normal ν and the nematic director $\mathbf{n}(\mathbf{r})$ at any point \mathbf{r} is denoted as $\alpha(\mathbf{r})$.

3.2 Theory

3.2.1 Noninteracting particles in a nematic liquid crystal

As a first step, we consider a collection of magnetic colloids immersed in an NLC. Each colloid is represented by a thin disc of radius R and negligible thickness with the outer normal ν to the surface (see Fig. 3.1). A point magnetic dipole of strength m and direction $\omega \parallel \nu$ is placed in the center of the disc. (Note that the direction of ν depends on which side of the disc is considered whereas the direction of ω does not.) The position of the colloid is the position of its center and the orientation of the colloid is the direction of its magnetic dipole ω . (In a more general model ω and ν form a nonzero angle.)

There are four main types of interaction between such colloids: the magnetic dipole-dipole interaction, the effective interaction induced by the elasticity of the NLC medium, steric hard-core interactions, and the van der Waals interaction. Here we consider very dilute suspensions of magnetic particles, the volume fractions $\phi \approx 3 \times 10^{-4}$ of which are comparable with those in Ref. [102]. For such small densities, the dipole-dipole interaction between two colloids with magnetic moments $m \approx 3 \times 10^{-18} \text{ Am}^2$ (see Ref. [102]) and the van der Waals interaction can be neglected [139]. Moreover, the steric interaction is disregarded due to its short range and hence the very small impact on the properties of such a dilute solution. Here, the effective colloid interaction induced by the NLC elasticity can also be neglected due to the high dilution of the suspension and the weak coupling of colloids to the NLC matrix (see Sec. 3.2.2). Therefore, as direct colloid-colloid

interactions are negligible for the type of systems considered here, on the mesoscopic level the colloidal fluid can be described as an ideal gas in an external field generated by the NLC. The corresponding grand potential functional in terms of the number density $\rho(\mathbf{r}, \boldsymbol{\omega})$ of colloids at position \mathbf{r} and with orientation $\boldsymbol{\omega}$ is given by

$$\begin{aligned} \beta\Omega[\rho, \mathbf{n}] = & \int d^3r \int d^2\omega \rho(\mathbf{r}, \boldsymbol{\omega}) \left[\ln(\rho(\mathbf{r}, \boldsymbol{\omega})\Lambda^3) - 1 - \beta\mu \right. \\ & \left. + \beta V_{\text{NLC}}(\boldsymbol{\omega}, \mathbf{n}(\mathbf{r})) - \beta m \boldsymbol{\omega} \cdot \mathbf{B} \right], \end{aligned} \quad (3.1)$$

where Λ denotes the thermal de Broglie wave length, μ is the chemical potential of the colloids, \mathbf{B} describes a uniform external magnetic field acting on a magnetic dipole of strength m and orientation $\boldsymbol{\omega}$ and $\beta V_{\text{NLC}}(\boldsymbol{\omega}, \mathbf{n}(\mathbf{r}))$ is the one particle external field which describes the coupling of a colloid at position \mathbf{r} and with orientation $\boldsymbol{\omega}$ to the NLC with the local director $\mathbf{n}(\mathbf{r})$ at the position of the colloid [140].

The form of $\beta V_{\text{NLC}}(\boldsymbol{\omega}, \mathbf{n}(\mathbf{r}))$ is not known a priori; therefore we adopt certain assumptions in order to model it: whereas the nematic director field $\mathbf{n}(\mathbf{r})$ may be nonuniform on mesoscopic length scales, it is assumed to vary slowly on the scale of the colloid: $|\nabla \mathbf{n}(\mathbf{r})|R \ll 1$. The colloids are separated far from each other due to their low number density. Thus it is assumed that the interaction of a particular colloid with the NLC is determined by the director field in the close vicinity of the colloid. Accordingly, in order to obtain an expression for the one particle elastic potential $\beta V_{\text{NLC}}(\boldsymbol{\omega}, \mathbf{n}(\mathbf{r}))$ (see, c.f., Eq. (3.14)), the particular case of an isolated, disc-like colloid immersed in a uniform director field $\mathbf{n}(\mathbf{r}) = \mathbf{n}_0 = \text{const}$ (see Fig. 3.2) is considered in Sec. 3.2.2 below. Hence, a colloid with orientation $\boldsymbol{\omega}$ placed at position \mathbf{r} experiences a one-particle potential (see, c.f., Eq. (3.14)) which is obtained from, c.f., Eq. (3.10) by replacing the microscopically homogeneous far-field director \mathbf{n}_0 with the mesoscopic local director $\mathbf{n}(\mathbf{r})$.

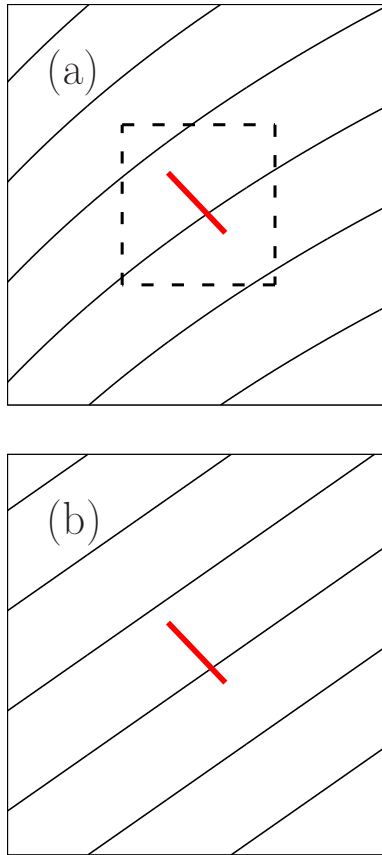


Figure 3.2: Illustration of the procedure used in the present study in order to model the one-particle elastic potential $\beta V_{\text{NLC}}(\boldsymbol{\omega}, \mathbf{n}(\mathbf{r}))$ in Eq. (3.1). (a): Sideview of a disc-like colloidal particle of radius R at position \mathbf{r} (red rod of length $2R$) is immersed in the NLC with the director field varying slowly on microscopic scales (black solid lines). The region of the slow variation of the director is indicated by the dashed square within which $|\nabla \mathbf{n}(\mathbf{r})|R \ll 1$ is satisfied. (b) The approximately constant field $\mathbf{n}(\mathbf{r})$ (i.e., the black solid lines within the dashed square in (a)) is extrapolated to everywhere and now plays the role of the far-field uniform director field \mathbf{n}_0 (black, solid, parallel, and straight lines) used in the complementary problem of a single disc immersed in an NLC (see Subsec. 3.2.2). The microscopic distortion of the nematic director due to its coupling to the surface of the colloid is not shown.

3.2.2 Single disc-like colloid immersed in a nematic liquid crystal

In this subsection we consider a single disc-like colloidal particle of radius R which is suspended in an NLC described by a mesoscopic director field $\mathbf{n}(\mathbf{r})$. According to Fig. 3.1, a frame of reference is attached to the colloid such that the z -axis is parallel to the normal of the particle. Here, we study the case of homeotropic boundary conditions on the surface of the colloid, i.e., it is energetically favorable for the director field $\mathbf{n}(\mathbf{r})$ at the surface to be parallel to the normal of the colloid (i.e., the z -axis). It is the aim of the present subsection to determine the free energy of the system as function of the colloid orientation, which is described by an angle θ between the z -axis and the uniform director \mathbf{n}_0 far away from the colloid (see Fig. 3.1).

Due to the local inversion symmetry of the nematic phase (i.e., due to the nematic directors $\mathbf{n}(\mathbf{r})$ and $-\mathbf{n}(\mathbf{r})$ describing the same thermodynamic state of the NLC [33]), both the angles $\theta = 0$ and $\theta = \pi$ correspond to the free-energetic “ground” state, i.e., the director field $\mathbf{n}(\mathbf{r})$ at any point \mathbf{r} of the colloid surface points along its surface normal. Moreover, since there are no deformations in the bulk NLC, the director field $\mathbf{n}(\mathbf{r})$ is uniform *everywhere*, and the elastic free energy of the NLC attains its minimum as a function of θ . In order to determine the free energy as function of $\theta \in [0, \pi/2]$ (the behavior in the range $\theta \in [\pi/2, \pi]$ follows from the symmetry of the free energy with respect to $\theta = \pi/2$ due to the local inversion symmetry of the NLC), it is obviously necessary to include the coupling of the director field $\mathbf{n}(\mathbf{r})$ to the particle surface.

In the limit, which is called “infinite anchoring”, in the following the director field $\mathbf{n}(\mathbf{r})$ at the colloid surface is kept fixed to a certain (here the normal) direction called “easy axis” [33]. In the language of boundary value problems this limit corresponds to a Dirichlet boundary condition at the surface of the particle. If this constraint is relaxed and the director field $\mathbf{n}(\mathbf{r})$ at the surface can deviate from the easy axis, the free energy acquires an extra contribution penalizing deviations from the easy direction:

$$F_s = W \int_{\text{disc}} d^2s [\mathbf{n}(\mathbf{s}) \times \boldsymbol{\nu}(\mathbf{s})]^2, \quad (3.2)$$

where $\mathbf{n}(\mathbf{s})$ is the director field at the point \mathbf{s} of the disc surface, $\boldsymbol{\nu}(\mathbf{s})$ is the easy axis which here is taken to be normal to the surface, and $W = \text{const} > 0$ is the anchoring strength with the dimension energy per surface area.

In the present context, the infinite anchoring limit has been investigated before. Within the infinite anchoring (IA) limit the free energy has the form [141]

$$\frac{F^{\text{IA}}}{KR} = 4\theta^2, \quad \theta \in [0, \pi/2], \quad (3.3)$$

where K denotes the Frank elastic constant of the NLC with dimension energy per length (i.e., force) within the one-constant approximation [33]. The opposite limit, i.e., the limit

of weak anchoring, has not been investigated systematically in the case of discs. This limit, which we shall refer to as “weak anchoring”, is the relevant one for the colloids used in the experiment reported in Ref. [102] (see below). It turns out (see below) that it is beneficial to formulate the description of the weak anchoring limit as an expansion of the free energy in terms of the dimensionless coupling constant

$$c := \frac{WR}{K}. \quad (3.4)$$

The same quantity was used in the Burylov-Raikher theory (see Ref. [90]). In the following, the contributions to the free energy up to and including the order $\propto c^2$ (see, c.f., Eq. (3.10)) are determined.

In order to obtain a systematic expansion of the free energy of the NLC with a colloidal inclusion in terms of powers of the coupling constant c , one can start from the Frank-Oseen functional of the nematic director field \mathbf{n} :

$$\frac{F[\mathbf{n}]}{KR} = \frac{1}{2R} \int_{\mathcal{V}} d^3r \frac{\partial n_i(\mathbf{r})}{\partial x_j} \frac{\partial n_i(\mathbf{r})}{\partial x_j} + \frac{c}{R^2} \int_{\partial\mathcal{V}} d^2s [\mathbf{n}(\mathbf{s}) \times \boldsymbol{\nu}(\mathbf{s})]^2, \quad (3.5)$$

where summation over repeated indices is assumed, $\mathcal{V} \subseteq \mathbb{R}^3$ is the space filled by the NLC, and $\partial\mathcal{V}$ denotes the boundary of the NLC (colloid + cell walls). If all lengths are measured in units of R (i.e., $d^3r/R^3 = d^3\tilde{r}$, $R\partial/\partial x_j = \partial/\partial\tilde{x}_j$, $d^2s/R^2 = d^2\tilde{s}$, $\mathcal{V}/R^3 = \tilde{\mathcal{V}}$ and $\partial\mathcal{V}/R^2 = \partial\tilde{\mathcal{V}}$) the dimensionless parameter c is (up to a numerical factor) the ratio of the surface energy (second term on the right-hand side of Eq. (3.5)) and the bulk elastic energy (first term on the right-hand side of Eq. (3.5)). Alternatively, c can be viewed as the ratio of the particle radius R and the extrapolation length $l := K/W$ [33]. Therefore, the coupling constant c measures the cost of free energy for the director field \mathbf{n} to deviate at the colloid surface from the easy axis compared to the cost of free energy for an elastic distortion of the director field \mathbf{n} in the bulk. We define the “weak anchoring” regime by the condition $c \ll 1$ and note that according to this definition the notion of “weak” does not necessarily mean that the surface anchoring W is small, but rather that the product WR is small compared to K . The latter of which is a material parameter of the particular NLC, independent of the colloid material or size. This implies that for large values of W one can still find $c \ll 1$ for sufficiently small particles. As a numerical example we consider, in line with Ref. [142], the realistic range $W \in [0, 10^{-4}]$ N/m of anchoring strengths, the particle size $R = 35$ nm, which is roughly the mean of the size distribution in Ref. [102], and $K = 10^{-11}$ N for the liquid crystal 5CB. For these material parameters the coupling constants are in the range $c \in [0, 0.35]$.

Next, one observes in the case of a thin disc, with homeotropic anchoring of arbitrary strength and with normal $\boldsymbol{\nu} = \mathbf{e}_z$, immersed in an NLC with far-field director \mathbf{n}_0 , that the nematic director field $\mathbf{n}(\mathbf{r})$ anywhere inside the NLC is parallel to the plane spanned by \mathbf{e}_z and \mathbf{n}_0 [143], which, in the following, is, without restriction of generality, taken to

be the x - z -plane spanned by the unit vectors \mathbf{e}_x and \mathbf{e}_z . This allows one to express the nematic director field $\mathbf{n} : \mathcal{V} \rightarrow \mathbb{R}^3$ in terms of a scalar field $\alpha : \mathcal{V} \rightarrow \mathbb{R}$ according to

$$\mathbf{n}(\mathbf{r}) = \mathbf{e}_x \sin(\alpha(\mathbf{r})) + \mathbf{e}_z \cos(\alpha(\mathbf{r})). \quad (3.6)$$

At large distances from the colloid, $|\mathbf{r}| \gg R$, one has the Dirichlet boundary condition $\alpha(\mathbf{r}) \simeq \theta$. In terms of the scalar field α the free energy functional in Eq. (3.5) reads

$$\frac{F[\alpha]}{KR} = \frac{1}{2R} \int_{\mathcal{V}} d^3r [\nabla \alpha(\mathbf{r})]^2 + \frac{c}{R^2} \int_{\partial \mathcal{V}} d^2s [\sin(\alpha(\mathbf{s}))]^2. \quad (3.7)$$

The equilibrium state minimizes $F[\alpha]/(KR)$ with respect to variations of α which preserve the Dirichlet boundary condition at large distances. This corresponds to the Euler-Lagrange equations

$$\begin{cases} \nabla^2 \alpha(\mathbf{r}) = 0 & , \mathbf{r} \in \mathcal{V} \\ \nabla \alpha(\mathbf{s}) \cdot \boldsymbol{\nu}(\mathbf{s}) = \frac{c}{R} \sin(2\alpha(\mathbf{s})) & , \text{at the disc surfaces} \\ \alpha(\mathbf{r}) \simeq \theta & , |\mathbf{r}| \gg R. \end{cases} \quad (3.8)$$

The boundary problem posed in Eq. (3.8) is difficult to solve analytically, in particular due to the nonlinear expression on the right-hand side of the second line in Eq. (3.8). However, for small values of the coupling parameter c it is promising to consider an expansion of the scalar field α in terms of powers of c :

$$\alpha(\mathbf{r}) = \sum_{n=0}^{\infty} c^n \alpha^{(n)}(\mathbf{r}) = \alpha^{(0)}(\mathbf{r}) + c\alpha^{(1)}(\mathbf{r}) + \dots. \quad (3.9)$$

By inserting the above expansion into Eq. (3.8) and by comparing corresponding orders of c one infers boundary problems for $\alpha^{(n)}(\mathbf{r})$, $n \in \{0, 1, 2, \dots\}$. It turns out that the boundary problems for $\alpha^{(0)}(\mathbf{r})$ and $\alpha^{(1)}(\mathbf{r})$ can be solved analytically (see Appendix A). Accordingly, here we restrict the following discussion to these two terms of the expansion in Eq. (3.9). Inserting $\alpha^{(0)}(\mathbf{r})$ (Eq. (A.2)) and $\alpha^{(1)}(\mathbf{r})$ (Eq. (A.5)) into Eq. (3.7) leads to the weak anchoring (WA) limit of the free energy (Eq. (A.14)):

$$\frac{F^{\text{WA}}}{KR} = - \left(2\pi c + \frac{32}{3} c^2 \right) (\mathbf{n}_0 \cdot \boldsymbol{\omega})^2 + \frac{32}{3} c^2 (\mathbf{n}_0 \cdot \boldsymbol{\omega})^4. \quad (3.10)$$

It is worth noting that the term $\propto c^1$ in Eq. (3.10) can be written in the form

$$-2\pi c (\mathbf{n}_0 \cdot \boldsymbol{\omega})^2 = -2\pi c [\cos \theta]^2 = \text{const} + 2\pi \frac{WR}{K} [\sin \theta]^2, \quad (3.11)$$

which is equivalent to the expression obtained in Ref. [144] for the case of a thin rod with tangential anchoring. This fact is related to the topological similarity between the thin disc with homeotropic anchoring and the thin rod with planar anchoring.

In Sec. 3.3 an interval $c \in [0, c_{\text{weak}}]$ with $c_{\text{weak}} \approx 0.1$ is determined numerically such that within this interval Eq. (3.10) is a quantitatively reliable approximation of the exact free energy $F/(KR)$.

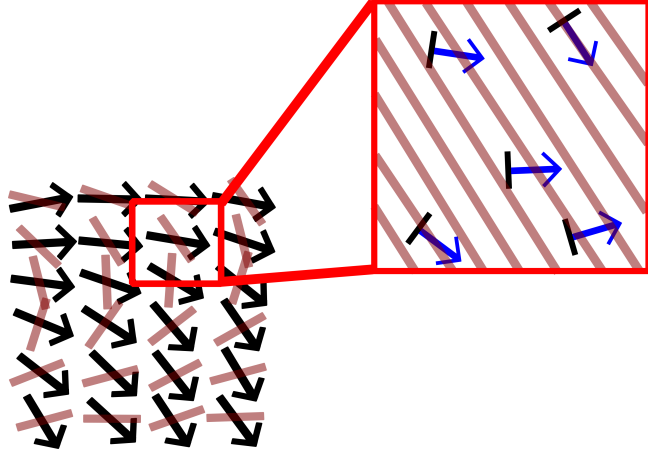


Figure 3.3: Illustration of the coarse-graining used to merge the microscopic and the mesoscopic theory. The mesoscopic theory is based on the magnetization field $\mathbf{M}(\mathbf{r})$ (black arrows in the lower left part) and on the director field $\mathbf{n}(\mathbf{r})$ (pale red rods in the lower left part). The mesoscopic magnetization at the position of a volume element (red square in the lower left part) is obtained from the magnetic moments of individual colloids (blue arrows normal to the black projected discs in the upper right part) averaged over the microscopic distribution inside the volume element (red square in the upper right part). Within the mesoscopic picture the local director field corresponds to the far-field director \mathbf{n}_0 within the microscopic one-particle picture of individual colloids (pale red hatching, see Sec. 3.2.2). The microscopic distortion of the nematic director due to its coupling to the surface of the colloid is not shown.

3.2.3 Mesoscopic functional

In order to enable a comparison with Ref. [102] we aim for replacing the functional $\Omega[\rho, \mathbf{n}]$ of the number density profile ρ and the nematic director profile \mathbf{n} in Eq. (3.1) by a functional $\bar{\Omega}[\mathbf{M}, \mathbf{n}] := \Omega[\bar{\rho}(\mathbf{r}, \boldsymbol{\omega}, [\mathbf{M}, \mathbf{n}]), \mathbf{n}]$ of the magnetization field \mathbf{M} and the nematic director profile \mathbf{n} where $\bar{\rho}(\mathbf{r}, \boldsymbol{\omega}, [\mathbf{M}, \mathbf{n}])$ is the number density profile of colloids at position \mathbf{r} with orientation $\boldsymbol{\omega}$ for a prescribed magnetization field $\mathbf{M}(\mathbf{r})$ and a nematic director field $\mathbf{n}(\mathbf{r})$; $\bar{\rho}$ minimizes the functional in Eq. (3.1), i.e., it is a solution of the Euler-Lagrange equation

$$\begin{aligned} m(\boldsymbol{\omega} \cdot \boldsymbol{\lambda}(\mathbf{r}, [\mathbf{M}, \mathbf{n}])) &= \frac{\delta \beta \Omega}{\delta \rho(\mathbf{r}, \boldsymbol{\omega})} [\bar{\rho}(\mathbf{r}, \boldsymbol{\omega}, [\mathbf{M}, \mathbf{n}]), \mathbf{n}] \\ &= \ln(\bar{\rho}(\mathbf{r}, \boldsymbol{\omega}, [\mathbf{M}, \mathbf{n}]) \Lambda^3) - \beta \mu \\ &\quad + \beta V(\boldsymbol{\omega}, \mathbf{n}(\mathbf{r}), \mathbf{B}), \end{aligned} \quad (3.12)$$

where $\beta V(\boldsymbol{\omega}, \mathbf{n}(\mathbf{r}), \mathbf{B}) := \beta V_{\text{NLC}}(\boldsymbol{\omega}, \mathbf{n}(\mathbf{r})) - \beta m \boldsymbol{\omega} \cdot \mathbf{B}$ and where $\boldsymbol{\lambda}(\mathbf{r}, [\mathbf{M}, \mathbf{n}])$ are the Lagrange multipliers which implement the constraint

$$\mathbf{M}(\mathbf{r}) = \int d^2 \omega \, m \boldsymbol{\omega} \bar{\rho}(\mathbf{r}, \boldsymbol{\omega}, [\mathbf{M}, \mathbf{n}]). \quad (3.13)$$

According to Subsecs. 3.2.1 and 3.2.2, the external field which the NLC exerts on the fluid of colloidal discs, is described by

$$\begin{aligned}\beta V_{\text{NLC}}(\boldsymbol{\omega}, \mathbf{n}(\mathbf{r})) &= -(a+b)(\boldsymbol{\omega} \cdot \mathbf{n}(\mathbf{r}))^2 + b(\boldsymbol{\omega} \cdot \mathbf{n}(\mathbf{r}))^4, \\ a &:= 2\pi\beta KRc, \quad b := \frac{32}{3}\beta KRc^2.\end{aligned}\tag{3.14}$$

The solution of Eq. (3.12) is given by

$$\begin{aligned}\bar{\rho}(\mathbf{r}, \boldsymbol{\omega}, [\mathbf{M}, \mathbf{n}]) \\ = \zeta \exp\left(-\beta V(\boldsymbol{\omega}, \mathbf{n}(\mathbf{r}), \mathbf{B}) + m\boldsymbol{\omega} \cdot \boldsymbol{\lambda}(\mathbf{r}, [\mathbf{M}, \mathbf{n}])\right)\end{aligned}\tag{3.15}$$

with the fugacity $\zeta := \exp(\beta\mu)/\Lambda^3$. Upon inserting Eq. (3.15) into Eq. (3.1) one obtains

$$\begin{aligned}\beta\Omega[\bar{\rho}(\mathbf{r}, \boldsymbol{\omega}, [\mathbf{M}, \mathbf{n}]), \mathbf{n}] &= \int d^3r \int d^2\omega \bar{\rho}(\mathbf{r}, \boldsymbol{\omega}, [\mathbf{M}, \mathbf{n}]) \left[\beta\mu - \beta V(\boldsymbol{\omega}, \mathbf{n}(\mathbf{r}), \mathbf{B}) \right. \\ &\quad \left. + m\boldsymbol{\omega} \cdot \boldsymbol{\lambda}(\mathbf{r}, [\mathbf{M}, \mathbf{n}]) - 1 - \beta\mu + \beta V(\boldsymbol{\omega}, \mathbf{n}(\mathbf{r}), \mathbf{B}) \right] \\ &= \int d^3r \left[\boldsymbol{\lambda}(\mathbf{r}, [\mathbf{M}, \mathbf{n}]) \cdot \int d^2\omega m\boldsymbol{\omega} \bar{\rho}(\mathbf{r}, \boldsymbol{\omega}, [\mathbf{M}, \mathbf{n}]) \right. \\ &\quad \left. - \int d^2\omega \bar{\rho}(\mathbf{r}, \boldsymbol{\omega}, [\mathbf{M}, \mathbf{n}]) \right],\end{aligned}\tag{3.16}$$

from which it follows that (see Eq. (3.13))

$$\beta\bar{\Omega}[\mathbf{M}, \mathbf{n}] = \int d^3r \left[\mathbf{M}(\mathbf{r}) \cdot \boldsymbol{\lambda}(\mathbf{r}, [\mathbf{M}, \mathbf{n}]) - \rho_0(\mathbf{r}, [\mathbf{M}, \mathbf{n}]) \right],\tag{3.17}$$

where $\rho_0[\mathbf{M}, \mathbf{n}]$ is the orientation-independent number density profile of the discs:

$$\rho_0(\mathbf{r}, [\mathbf{M}, \mathbf{n}]) := \int d^2\omega \bar{\rho}(\mathbf{r}, \boldsymbol{\omega}, [\mathbf{M}, \mathbf{n}]).\tag{3.18}$$

Equation (3.13) provides the important link which allows one the formulation of the functional of the density profile $\bar{\rho}(\mathbf{r}, \boldsymbol{\omega}, [\mathbf{M}, \mathbf{n}])$ in terms of the mesoscopic magnetization field $\mathbf{M}(\mathbf{r})$. The illustration of this idea is shown in Fig. 3.3.

In order to derive an explicit expression for $\beta\bar{\Omega}[\mathbf{M}, \mathbf{n}]$ it is convenient to introduce an effective magnetic field

$$\mathbf{h}(\mathbf{r}, [\mathbf{M}, \mathbf{n}]) := \boldsymbol{\lambda}(\mathbf{r}, [\mathbf{M}, \mathbf{n}]) + \beta\mathbf{B}\tag{3.19}$$

and the generating function

$$\begin{aligned}Z(\mathbf{h}) &:= \int d^2\omega \exp\left(A_1(\boldsymbol{\omega} \cdot \mathbf{n}(\mathbf{r}))^2 + A_2(\boldsymbol{\omega} \cdot \mathbf{n}(\mathbf{r}))^4 \right. \\ &\quad \left. + m\mathbf{h} \cdot \boldsymbol{\omega}\right)\end{aligned}\tag{3.20}$$

with $A_1 := a + b$ and $A_2 := -b$ denoting the coefficients of two powers of $(\boldsymbol{\omega} \cdot \mathbf{n}(\mathbf{r}))$. This leads to (see Eqs. (3.15) and (3.18))

$$\rho_0(\mathbf{r}, [\mathbf{M}, \mathbf{n}]) = \zeta Z(\mathbf{h}(\mathbf{r}, [\mathbf{M}, \mathbf{n}])) \quad (3.21)$$

and

$$\mathbf{M}(\mathbf{r}) = \zeta \frac{\partial Z}{\partial \mathbf{h}}(\mathbf{h}(\mathbf{r}, [\mathbf{M}, \mathbf{n}])). \quad (3.22)$$

With this notation Eq. (3.17) reads

$$\beta \bar{\Omega}[\mathbf{M}, \mathbf{n}] = \int d^3r \left[\zeta \left(\mathbf{h}(\mathbf{r}) \cdot \frac{\partial Z}{\partial \mathbf{h}}(\mathbf{h}(\mathbf{r})) - Z(\mathbf{h}(\mathbf{r})) \right) - \beta \mathbf{M}(\mathbf{r}) \cdot \mathbf{B} \right] \Bigg|_{\mathbf{h}=\mathbf{h}(\mathbf{r}, [\mathbf{M}, \mathbf{n}])}. \quad (3.23)$$

In the experiments described in Ref. [102] the sample is prepared by dispersing a number density ρ_{iso} of colloids in the isotropic high-temperature phase of the solvent, followed by a quench of the solvent into the low-temperature nematic phase. In the absence of an external magnetic field ($\mathbf{B} = 0$), the magnetization vanishes ($\mathbf{M} = 0$) before and after the quench, which corresponds to the effective magnetic field $\mathbf{h} = 0$ [145]. Noting that the number density of colloids does not change during the quench, one obtains from Eq. (3.21)

$$\zeta = \frac{\rho_0}{Z(0)} = \frac{\rho_{\text{iso}}}{Y_{00}}, \quad (3.24)$$

where Y_{00} is defined in Eq. (B.9).

It turns out (see Appendix B) that this part of the integrand in Eq. (3.23), which depends on Z , is an even function of both $H := m|\mathbf{h}|$ and $u := \mathbf{n} \cdot \mathbf{h}/|\mathbf{h}|$ (Eq. (3.19)), i.e., a function of $m^2|\mathbf{h}|^2$ and $(\mathbf{n} \cdot \mathbf{h}/|\mathbf{h}|)^2$. Moreover, it can be shown (see Appendix B) that the quantities $T := |\mathbf{M}|/(m\zeta)$ and $t := \mathbf{n} \cdot \mathbf{M}/(m\zeta)$ are both functions of H and u , too. If one can invert the map $(H, u) \mapsto (T, t)$, the integrand in Eq. (3.23), which equals the grand potential density, can be expressed as function of $|\mathbf{M}|^2$ and $(\mathbf{M} \cdot \mathbf{n})^2$. However, in general inverting this map is very challenging. Therefore, the following considerations are restricted to a quadratic approximation which includes only terms up to $\sim H^2$ in $Z(\mathbf{h}) =: \bar{Z}(H, u)$ (see Eq. (B.12)):

$$\bar{Z}(H, u) \simeq Y_{00} + Y_{10}H^2 + Y_{12}H^2u^2. \quad (3.25)$$

(Note the absence of a term $\propto u^2$.) From Eq. (B.7) in Appendix B one obtains the following system of equations (see Eq. (B.13)):

$$\begin{cases} (t(H, u))^2 &= 4(Y_{10} + Y_{12})^2 H^2 u^2 \\ (T(H, u))^2 &= 4(2Y_{10}Y_{12} + Y_{12}^2) H^2 u^2 + 4Y_{10}^2 H^2, \end{cases} \quad (3.26)$$

which readily can be inverted. This renders the grand potential functional within the quadratic approximation:

$$\beta\bar{\Omega}[\mathbf{M}, \mathbf{n}] = \int d^3r \left[\zeta(C_{00} + C_{20}T(\mathbf{r})^2 + C_{02}t(\mathbf{r})^2) - \beta\mathbf{M}(\mathbf{r}) \cdot \mathbf{B} \right] \quad (3.27)$$

with (see Eqs. (B.16)-(B.18))

$$C_{00} = -Y_{00}, \quad C_{20} = \frac{1}{4Y_{10}}, \quad C_{02} = -\frac{Y_{12}/Y_{10}}{4(Y_{10} + Y_{12})}, \quad (3.28)$$

or, if written explicitly in terms of $|\mathbf{M}|$ and $\mathbf{M} \cdot \mathbf{n}$:

$$\beta\bar{\Omega}[\mathbf{M}, \mathbf{n}] = \int d^3r \left[\rho_{\text{iso}} \left(\frac{C_{00}}{Y_{00}} + Y_{00}C_{20} \left| \frac{\mathbf{M}(\mathbf{r})}{m\rho_{\text{iso}}} \right|^2 + Y_{00}C_{02} \left(\frac{\mathbf{M}(\mathbf{r})}{m\rho_{\text{iso}}} \cdot \mathbf{n}(\mathbf{r}) \right)^2 \right) - \beta\mathbf{M}(\mathbf{r}) \cdot \mathbf{B} \right]. \quad (3.29)$$

3.3 Results

3.3.1 Limits of reliability for using the one-particle potential

In the present study we use the expression in Eq. (3.14) for the one-particle potential V_{NLC} corresponding to the weak anchoring regime described by the energy $F^{\text{WA}}/(KR)$ in Eq. (3.10) of a single colloidal particle with orientation $\boldsymbol{\omega}$ at position \mathbf{r} , which is immersed in the NLC with the nematic director $\mathbf{n}(\mathbf{r})$. In order to assess the accuracy of the expression in Eqs. (3.10) or (3.14) as function of the coupling constant c , for comparison the full expression for the free energy in Eq. (3.7) is minimized numerically by using a Galerkin finite element method [146], because analytical solutions of the boundary value problems for $\alpha^{(j)}, j \geq 2$, are not available. The specific set-up, which is considered, consists of a cubic box of dimension $30R \times 30R \times 30R$ which contains a single thin disc in its center. The interior of the box is decomposed into tetrahedra and the boundary due to the disc is decomposed into triangles. Within each finite element the unknown function $\alpha(\mathbf{r})$ is approximated by linear functions which interpolate between its values at the corners, i.e., the vertices of the triangulation. Within the finite-dimensional subspace of functions, which are piecewise linear with respect to the given triangulation, both the volume and the surface integral in Eq. (3.7) can be calculated explicitly for each finite element. This allows for a numerical minimization within this finite-dimensional subspace. The described Galerkin method can be performed for arbitrary values of the coupling constant c , i.e., one is not restricted to the weak anchoring regime.

Figure 3.4 compares the numerically obtained free energy (symbols) with the one obtained within the weak anchoring limit (Eq. (3.10), solid lines) as function of θ for

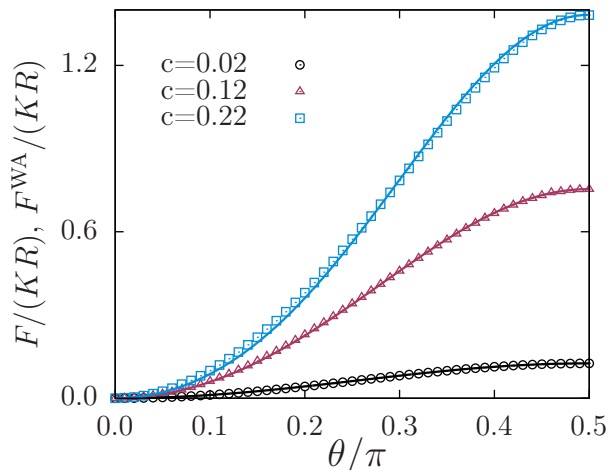


Figure 3.4: Comparison of the free energy $F/(KR)$ obtained by numerical minimization of Eq. (3.7) (symbols) and the corresponding analytical result $F^{\text{WA}}/(KR)$ (Eq. (3.10), solid lines) for three values of the coupling constant c . Already for $c = 0.22$ (blue, squares) the numerical data noticeably deviate from the analytic result.

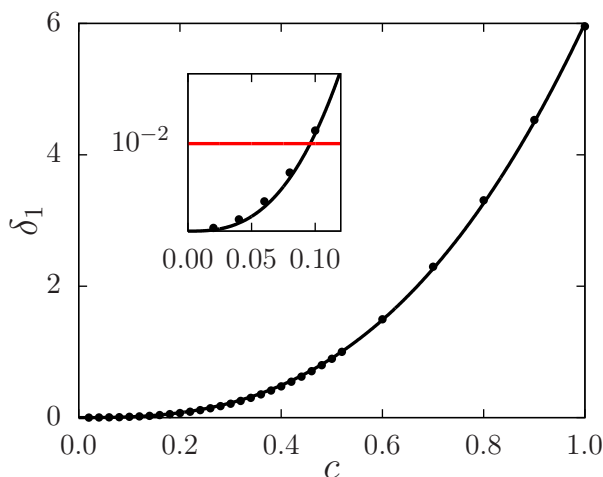


Figure 3.5: Quadratic norm $\delta_1(c) := \sqrt{\int_0^{\pi/2} d\theta \left| \frac{F^{\text{WA}}}{KR} - \frac{F}{KR} \right|^2}$ as function of the coupling strength c , where F represents the numerically exact free energy obtained from Eq. (3.7) and F^{WA} its weak anchoring limit (Eq. (3.10)). The black solid line is a fit of the power law αc^ζ to the data; $\alpha = 6.00 \pm 0.01$ and $\zeta = 2.73 \pm 0.01$. The inset is a close-up of the range $c \in [0, 0.1]$ illustrating the criterion in Eq. (3.30) for $\varepsilon = 10^{-2}$.

three values $c \in \{0.02, 0.12, 0.22\}$. For very small coupling constants (see $c = 0.02$) the weak anchoring limit Eq. (3.10) agrees very well with the numerical results, whereas there are small but visible deviations for larger values of c (see Fig. 3.4, $c = 0.22$).

In order to quantify the deviation of the weak anchoring approximation $F^{\text{WA}}/(KR)$ in Eq. (3.10) from the exact expression $F/(KR)$ in Eq. (3.7), the following criterion is introduced [147]: For a given $\varepsilon > 0$ the weak anchoring approximation $F \approx F^{\text{WA}}$ is

considered to be sufficient to describe the free energy F for a fixed value of c , if ε is an upper bound of the quadratic norm

$$\delta_1(c) := \sqrt{\int_0^{\pi/2} d\theta \left| \frac{F^{\text{WA}}}{KR} - \frac{F}{KR} \right|^2} < \varepsilon. \quad (3.30)$$

The particular choice of ε is somewhat arbitrary. Figure 3.5 shows δ_1 as a function of the coupling strength c . The resulting curve can be fitted by a power law αc^ζ with the amplitude $\alpha = 6.00 \pm 0.01$ and the exponent $\zeta = 2.73 \pm 0.01$. This fit function allows one to determine a value c_{weak} such that the criterion in Eq. (3.30) with a given tolerance ε is fulfilled for $c < c_{\text{weak}}$:

$$c_{\text{weak}} = \left(\frac{\varepsilon}{\alpha} \right)^{1/\zeta} \approx \left(\frac{\varepsilon}{6} \right)^{0.366}. \quad (3.31)$$

A value of, e.g., $\varepsilon = 10^{-2}$ implies $c_{\text{weak}} \approx 0.1$ (see the inset in Fig. 3.5).

Considering Eq. (A.14), the contributions to which, up to quadratic order in c , are given by Eq. (3.10), it is tempting to speculate that the term of cubic order in c is of the form $\sim c^3[\sin(3\theta)]^2$. In order to assess this presumption one can use the fact that the free energy $F(\theta)/(KR)$ in Eq. (3.7) is an even function of θ with period π , which allows for an expansion into a Fourier series

$$\frac{F(\theta)}{KR} = \frac{a_0}{2} + \sum_{n=1}^{\infty} a_n \cos(2n\theta), \quad (3.32)$$

with the Fourier coefficients

$$a_n = \frac{4}{\pi} \int_0^{\pi/2} d\theta \frac{F(\theta)}{KR} \cos(2n\theta), \quad n = 0, 1, 2, \dots \quad (3.33)$$

In the context of actual numerical schemes only a finite number N of free energy values $F(\theta_i)/(KR)$ for the angles θ_i , $i \in \{0, 1, \dots, N-1\}$, are available. Hence, instead of using Eq. (3.33) by applying a suitable quadrature, one can — as an alternative approximation scheme — restrict the sum in Eq. (3.32) to $n \leq N-1$ and determine the coefficients a_n , $n \in \{0, 1, \dots, N-1\}$, via fitting the numerical data $F(\theta_i)/(KR)$, $i \in \{0, 1, \dots, N-1\}$, by trigonometric polynomials, i.e., superpositions of terms $\cos(2n\theta)$, $n \in \{0, 1, \dots, N-1\}$.

Figure 3.6 shows the absolute value of the coefficients a_n as functions of n (full dots) for $c = 0.02$ (upper panel) and $c = 0.22$ (lower panel). In addition, Fig. 3.6 also displays the corresponding coefficients obtained within the weak anchoring limit (see Eq. (3.10) and the open circles): $a_0/2 = \pi c - 4c^2/3 + \mathcal{O}(c^3)$, $a_1 = -\pi c + \mathcal{O}(c^3)$, and $a_2 = 4c^2/3 + \mathcal{O}(c^3)$. For small values of the coupling constant c (see the case $c = 0.02$ in the upper panel) the agreement between the weak anchoring coefficients and the exact ones is excellent. On the other hand, for large coupling constants (see $c = 0.22$ in the lower panel) one finds (i) that modes appear with comparatively large amplitudes $|a_n|$, $n \geq 3$, which signals that the exact data cannot be strictly described within the weak anchoring limit given

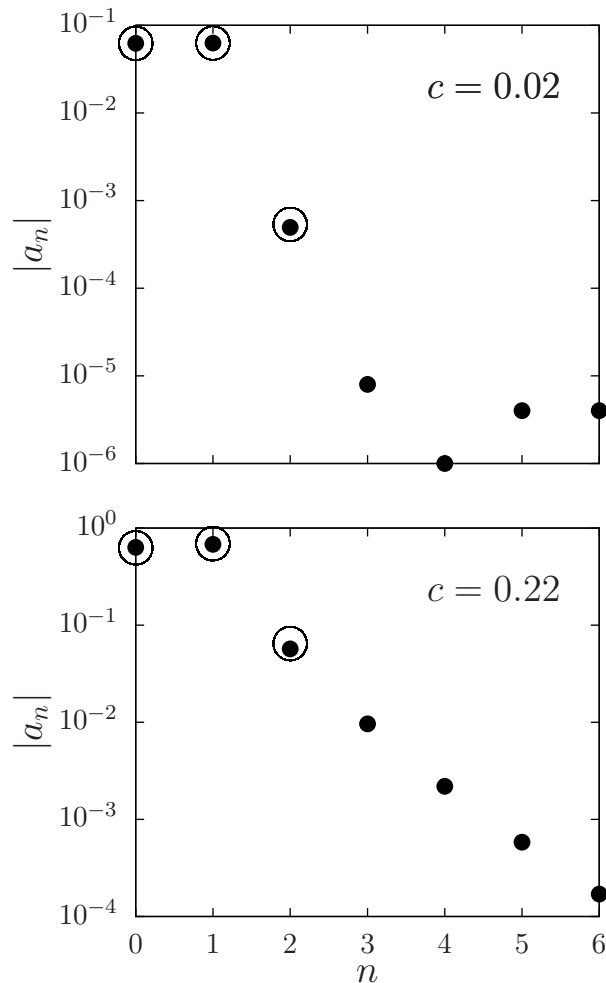


Figure 3.6: Absolute values $|a_n|$ of the first seven Fourier coefficients of the expansion of the exact free energy (Eq. (3.32), full dots) along with the three corresponding coefficients obtained within the weak anchoring limit (Eq. (3.10), open circles) for the coupling constant $c = 0.02$ (upper panel) and $c = 0.22$ (lower panel).

by Eq. (3.10), and (ii) that the exact coefficients $|a_n|$, $n \in \{0, 1, 2\}$, are not perfectly reproduced by those calculated within the weak anchoring limit according to Eq. (3.10). On a logarithmic scale these features are not conspicuous. However, they are much more apparent on a linear scale (not shown here). Both of these observations suggest that upon increasing the coupling constant c , Eq. (3.10) has to be modified in a way that (i) higher-order terms proportional to $\cos(2n\theta)$, $n \geq 3$, occur and (ii) terms of order c^3 or higher modify the coefficients a_n , $n = 0, 1, 2$.

As a byproduct of the Fourier analysis presented above, the very strong anchoring limit can be reconsidered. Figure 3.7 shows the coefficient $a_0/2$ appearing in Eq. (3.32) as function of c . As expected, for very strong couplings this curve approaches the value $\pi^2/3$, which is the coefficient $a_0/2$ appearing in the Fourier expansion of Eq. (3.3). This limiting value is attained exponentially (see the inset of Fig. 3.7).

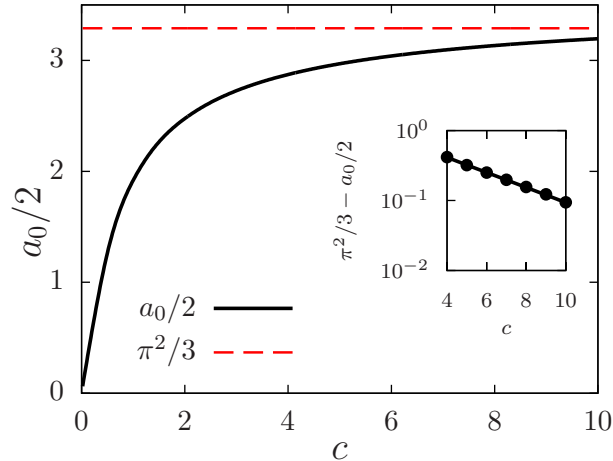


Figure 3.7: Coefficient a_0 of the leading term in the expansion in Eq. (3.32) of the free energy as function of the coupling constant c . The limit $a_0(c)/2 \rightarrow \pi^2/3$ for $c \rightarrow \infty$ is indicated by the red horizontal dashed line. The inset displays a semi-logarithmic plot of the deviation of $a_0/2$ from its asymptotic value, which is very well fitted by an exponential function $\lambda \exp(-\chi c)$ (solid line), where $\lambda = 1.11 \pm 0.02$ and $\chi = 0.247 \pm 0.003$.

In order to obtain an estimate of c_{strong} such that the infinite anchoring limit in Eq. (3.3) is reliable for $c > c_{\text{strong}}$, one can use a criterion similar to the one in Eq. (3.30), based on the quadratic norm

$$\delta_2(c) := \sqrt{\int_0^{\pi/2} d\theta \left| \frac{F^{\text{IA}}}{KR} - \frac{F}{KR} \right|^2}, \quad (3.34)$$

where F^{IA} (Eq. (3.3)) is the free energy within the infinite anchoring limit. Figure 3.8 shows δ_2 as a function of c . The tail of the data in the interval $c \in [4, 10]$ can be fitted by an exponential function $\kappa \exp(-\nu c)$ with $\kappa = 10.84 \pm 0.16$, and $\nu = 0.246 \pm 0.003$ (see the inset of Fig. 3.8). Thus, $\delta_2 < \varepsilon = 10^{-2}$ leads to

$$c_{\text{strong}} = -\frac{1}{\nu} \ln \frac{\varepsilon}{\kappa} \approx -\frac{1}{0.246} \ln \frac{\varepsilon}{10.84} \approx 28.4 \approx 28. \quad (3.35)$$

Accordingly, the interval $c \in [0, \infty)$ of coupling constants provides three regimes: (i) the weak coupling regime $c \in [0, c_{\text{weak}}]$ in which the free energy of a disc-like colloid in an NLC is very well described by Eq. (3.10), (ii) the strong coupling regime $c \in [c_{\text{strong}}, \infty)$ in which the free energy is independent of c and has the form of Eq. (3.3), and (iii) the intermediate coupling regime $c \in [c_{\text{weak}}, c_{\text{strong}}]$ in which the crossover between both previous limits takes place.

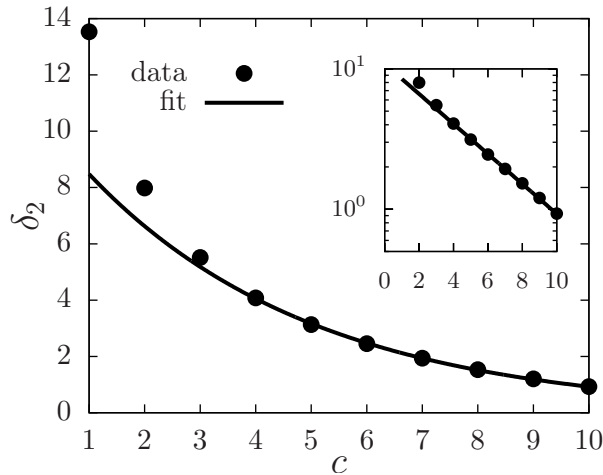


Figure 3.8: Quadratic norm δ_2 (see Eq. (3.34)) as function of the coupling constant c (full dots). The solid line is a fit of the data in the interval $c \in [4, 10]$ by an exponential function $\kappa \exp(-\nu c)$; $\kappa = 10.84 \pm 0.16$ and $\nu = 0.246 \pm 0.003$. The inset provides the same information but in terms of a semi-logarithmic plot.

3.3.2 Free energy functional in quadratic approximation

Disregarding the constant, \mathbf{M} - and \mathbf{n} -independent term $\propto C_{00}$ in the integrand on the right-hand side of Eq. (3.29), one infers the following expression for the free energy density of a fluid of magnetic discs suspended in an NLC:

$$f(\mathbf{M}, \mathbf{n}) = k_B T \rho_{\text{iso}} \left(Y_{00} C_{20} \left| \frac{\mathbf{M}}{m \rho_{\text{iso}}} \right|^2 + Y_{00} C_{02} \left(\frac{\mathbf{M}}{m \rho_{\text{iso}}} \cdot \mathbf{n} \right)^2 \right) - \mathbf{M} \cdot \mathbf{B}. \quad (3.36)$$

The dependence of the coefficients $Y_{00} C_{20}$ and $Y_{00} C_{02}$ (see Eqs. (B.9), (B.17), and (B.18)) on the coupling strength c is shown in Fig. 3.9. In contrast, in Ref. [102] the following *phenomenological* form of the free energy density has been proposed:

$$f_{\text{ph}}(\mathbf{M}, \mathbf{n}) = \frac{a}{2} |\mathbf{M}|^2 + \frac{b}{4} |\mathbf{M}|^4 - \frac{1}{2} \gamma \mu_0 (\mathbf{M} \cdot \mathbf{n})^2 - \mathbf{M} \cdot \mathbf{B}, \quad (3.37)$$

where the first two terms on the right-hand side are part of the Landau expansion describing the interaction between magnetic dipoles, the third term represents the coupling between the nematic order and the magnetization, and the last term is the interaction of magnetic dipoles with an external magnetic field.

The comparison between Eqs. (3.36) and (3.37) leads to the following conclusions: (i) By identifying the terms proportional to $|\mathbf{M}|^2$ in both expressions one infers the positive coefficient $a = 2k_B T Y_{00} C_{20} / (m^2 \rho_{\text{iso}}) > 0$. (ii) Since $a > 0$, the term proportional to $|\mathbf{M}|^4$ is unnecessary in the phenomenological expression in Eq. (3.37) and its absence in

Eq. (3.36) is without consequences. (iii) In agreement with physical intuition the coefficient γ introduced in Ref. [102] is positive and its dependence on the coupling strength c is given by

$$\begin{aligned}\gamma &= -2k_{\text{B}}T \frac{1}{\rho_{\text{iso}}} \frac{1}{\mu_0 m^2} Y_{00} C_{02} \\ &= \frac{k_{\text{B}}T}{2} \frac{1}{\rho_{\text{iso}}} \frac{1}{\mu_0 m^2} Y_{00} \frac{Y_{12}/Y_{10}}{Y_{10} + Y_{12}}.\end{aligned}\quad (3.38)$$

Figure 3.10 shows γ as function of the coupling constant c (see Eq. (3.38)) for the experimentally relevant parameters $\rho_{\text{iso}} = 1.5 \times 10^{19} \text{ m}^{-3}$ and $m \approx 3 \times 10^{-18} \text{ Am}^2$ taken from Ref. [148]. The order of magnitude of the theoretical result (black line) is in agreement with the values estimated from the experiment ($\gamma_{\text{exp}} \approx 110$, see Ref. [148]). Figure 3.10 shows that (at least in the regime of weak anchoring) γ increases monotonically with c . Based on the values given in Ref. [148] one can, on the one hand, estimate c from γ (red dot and dashed lines) and, on the other hand, one can estimate γ from c (blue square and dashed lines). Since values of c and γ given in Ref. [148] belong to one and the same system the red and blue dashed lines in Fig. 3.10 should coincide. However, this is not quite the case. The discrepancy may arise due to the fact that in all calculations the mean value of the particle size has been used assuming that the discs are monodisperse in size, whereas in the experiment the size distribution of the colloids has a finite width. Moreover, elastic interactions between the discs (generated by the nematic director field \mathbf{n}), which have been entirely neglected in the present study, might play a role for the properties of the actual system.

An obvious difference between the free energy density derived in this work and that obtained by Burylov and Raikher [90] is in the way the number density (or volume fraction) of colloids is entering. Within the Burylov-Raikher theory (see Ref. [90] and the extended theory Ref. [93]) the volume fraction is explicitly included in the expression of the free energy density by an ideal mixing entropy term and as a prefactor in front of the magnetization-director coupling term $\sim (\mathbf{M} \cdot \mathbf{n})^2$. In the theory derived in the present work the volume fraction of colloids (number density) is implicitly included via the magnetization $\mathbf{M}(\mathbf{r})$ (see Eq. (3.13)). The entropy term $\sim \rho \log \rho$ was explicitly present in the first step of the derivation, i.e., in the ideal gas contribution to the density functional (see Eq. (3.1)). The extended Burylov-Raikher theory (see Ref. [93]) contains a term proportional to $\sim (\mathbf{M} \cdot \mathbf{n})^4$ on top of the term $\sim (\mathbf{M} \cdot \mathbf{n})^2$, while our theory includes only the quadratic contribution $\sim (\mathbf{M} \cdot \mathbf{n})^2$. Also, in the present work microscopic distortions of the nematic director are implicitly taken into account in the coefficients $Y_{00}C_{20}$ and $Y_{00}C_{02}$ (see Eqs. (3.36) and (3.28)). Note also that the formula for the orientational energy of the rod-like colloid in an NLC derived by Burylov and Raikher (see Eq. (19) in Ref. [90]) is equivalent to expression in Eq. (3.10) of the current study if one disregards terms $\propto c^2$.

Knowing the explicit dependence $\gamma(c)$ offers the possibility to estimate the anchoring energy W by performing an experiment similar to the one described in Ref. [148]: Using Fig. 3.10, from an estimate of γ one obtains the corresponding value of c , which, knowing the mean size R of the platelets and the elastic constant K of the NLC, renders the value of W .

In Fig. 3.11 two expressions of γ as function of c are compared: one, for which in Eq. (3.14) only the term of first order in c (black dashed line, $\mathcal{O}(c^1)$) and one, for which terms up to second order in c (red solid line, $\mathcal{O}(c^2)$) are retained. (Note that the black dashed line is a *nonlinear* function of c , even if one has kept only the linear contribution $\mathcal{O}(c^1)$ in V_{NLC} , because γ depends nonlinearly on V_{NLC} .) The difference between the two expressions suggests that if one cuts off the expansion in c at too low order, the resulting phenomenological coupling constant γ is overestimated if $c \gtrsim 0.04$. The value of c inferred from the experiment (see Ref. [148]) lies below the value $c = 0.04$, i.e., in a range within which the two curves in Fig. 3.11 de facto coincide. Therefore, considering only the term $\propto c^1$ in Eqs. (3.10) or (3.14) does not change the outcome of the present effective theory in the context of the experimental parameters used in Ref. [148]. However, this assessment requires an analysis up to higher orders in c , as carried out in the present study.

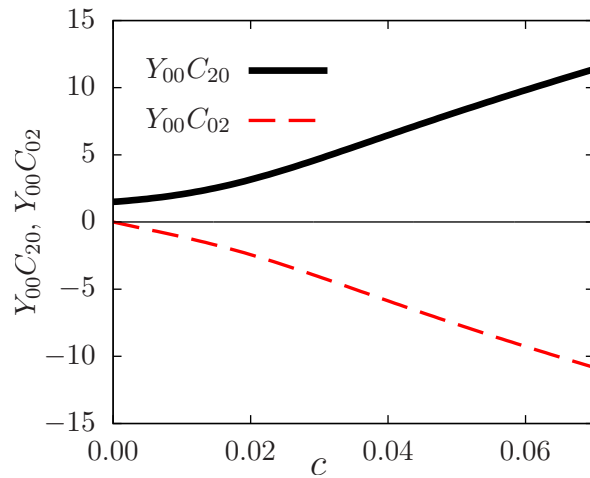


Figure 3.9: Coefficients $Y_{00}C_{20}$ (Eqs. (B.9) and (B.17)) and $Y_{00}C_{02}$ (Eqs. (B.9) and (B.18)) in Eq. (3.36) as functions of the coupling constant c .

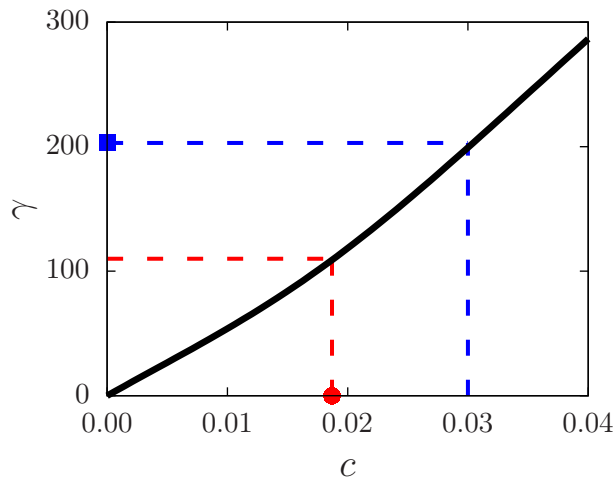


Figure 3.10: Dependence of the phenomenological coupling coefficient γ introduced in Ref. [102] (see Eq. (3.37)) on the microscopic coupling constant c as it follows from Eq. (3.38). The red circle denotes the value of $c \simeq 0.019$, which corresponds to the estimate of $\gamma \simeq 110$ given in Ref. [148]. The blue square denotes the value of $\gamma \simeq 203$, which corresponds to the estimate of $c \simeq 0.03$ based on the parameters used in Ref. [148]. Under ideal circumstances, the blue and the red dashed lines coincide.

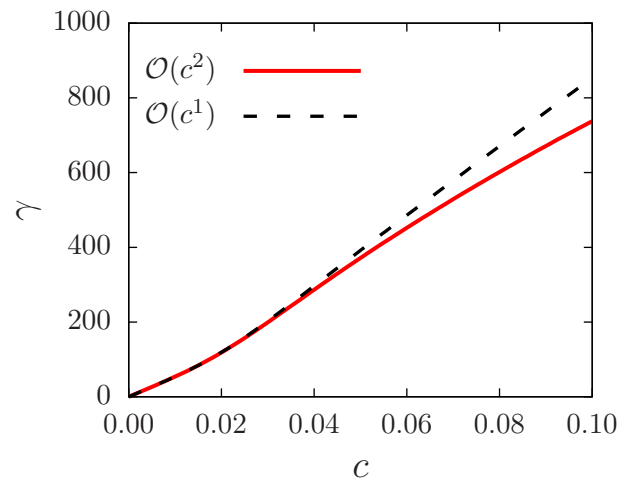


Figure 3.11: Comparison of the values of γ calculated by using in Eq. (3.14) only the first-order term in c (black dashed line, $\mathcal{O}(c^1)$) or both the first- and the second-order term in c (red solid line, $\mathcal{O}(c^2)$). The larger c , the more does the first-order theory overestimate the value of γ .

3.4 Discussion

Inspired by an expression introduced in Ref. [102], the present study derives a Landau-like free energy density of ferronematics in terms of the magnetization \mathbf{M} and the nematic director \mathbf{n} . The derivation starts from a density functional theory (DFT) which describes colloids suspended in a nematic liquid crystal (NLC). The coupling between the colloids and the NLC is modeled in terms of a one-particle potential (see Eq. (3.14)), which in the DFT framework plays the role of an external field. It depends on the orientation of the colloid and on the local nematic director field $\mathbf{n}(\mathbf{r})$. Motivated by the high dilution of the colloidal suspensions under consideration, a direct colloid-colloid interaction is neglected. Accordingly, the theory can be formulated in terms of a relatively simple local density functional. The one-particle potential in Eq. (3.14) is derived from the perturbation expansion (Eq. (3.10)) of the free energy in terms of the small parameter c , which represents the strength of the coupling of the NLC to the surface of a single colloidal particle (see Eq. (3.4)). In the present study the expansion of the free energy in terms of powers of c , together with the corresponding analytical expression for the nematic director profile around a colloidal particle, is determined. The term $\propto c^1$ in the expansion derived here is equivalent to the expression derived elsewhere (see Ref. [144]) for the different case of thin rods with tangential coupling. Using numerical methods, the range of values of the coupling constant c is estimated, within which the weak coupling limit (Eq. (3.10)) is accurate. It is shown that the next-order term is proportional to $(\sin(3\theta))^2$ with θ introduced in Fig. 3.1.

In the next step, the expression in Eq. (3.14) for the one-particle potential is used to establish the density functional in Eq. (3.1) of noninteracting discs subjected to an external field. Four possible kinds of pair interactions are neglected: (i) the direct dipole-dipole interaction due to the presence of magnetic moments; (ii) the steric repulsive interaction; (iii) the van der Waals interaction; and (iv) the effective elastic interaction induced by the NLC. On one hand, the dipole-dipole and the van der Waals interactions are negligibly small compared to the thermal energy $k_B T$ for the mean distances between the disc centers as given in Ref. [148]. Moreover, the steric interaction is disregarded due to its short-ranged character and therefore due to the low impact onto mesoscopic properties of a very dilute colloidal solution. On the other hand, the effective elastic interaction might be important even for dilute solutions because the effective elastic interaction for two discs, which are both inclined with respect to the far-field director, is described by a long-ranged Coulomb-like pair potential [149]. Here, we have neglected it nevertheless in order to keep the theory analytically tractable.

Deriving the free energy density in terms of powers of $|\mathbf{M}|$ and of the scalar product $\mathbf{M} \cdot \mathbf{n}$ appears to be out of analytic reach because the integral in Eq. (3.20) and thus $Z(\mathbf{h})$

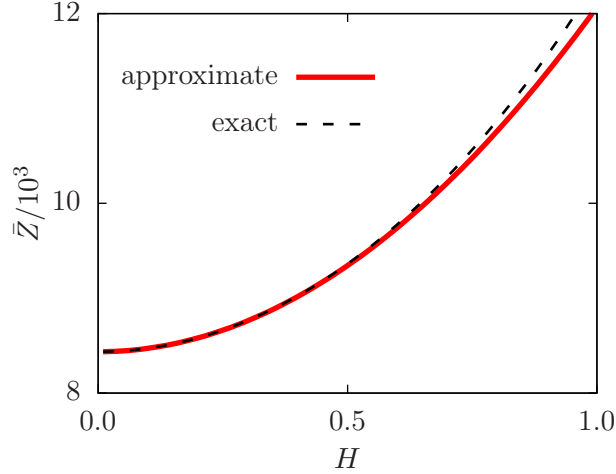


Figure 3.12: Comparison of the exact generating function $\bar{Z}(H, u)$ given by Eq. (3.20) (black dashed line) and its quadratic approximation provided in Eq. (3.25) (red solid line) for $c = 0.05$ and $u = 1$.

cannot be calculated analytically. Hence, in Eq. (3.25) the approximation of $Z(\mathbf{h}) = \bar{Z}(H, u)$ by a second-degree polynomial in terms of the variables $H := m|\mathbf{h}|$ and $u := \mathbf{n} \cdot \mathbf{h}/|\mathbf{h}|$ is introduced. The quality of this quadratic approximation is high for small values of H and it becomes poorer upon increasing H . Note, however, that in the present study large values of H are not needed. Indeed, whereas one can show that within the present model one has $|\mathbf{M}| \rightarrow \infty$ for $H \rightarrow \infty$, this limit is not realized in the context of the experimental situation under consideration, because the colloids carry a finite magnetic dipole moment m and their suspension in the NLC is given by a finite number density ρ_{iso} , so that $|\mathbf{M}(\mathbf{r})| \leq m\rho_{\text{iso}}$ at any point \mathbf{r} (for reason of simplicity assuming only very small segregation effects). Therefore one should not consider the whole range of H but only up to a certain value H_{max} , defined such that $|\mathbf{M}|/(m\rho_{\text{iso}}) \leq T(H_{\text{max}})/Y_{00} := 1$ holds (see the definition of T in the paragraph below Eq. (3.24), and see Eq. (3.24)). According to the second line of Eq. (3.26), H_{max} is a function of $u \in [-1, 1]$, i.e., of the cosine of the angle between the effective magnetic field \mathbf{h} and the nematic director \mathbf{n} of the NLC (see below Eq. (3.24)). Figure 3.12 shows a comparison of the exact generating function $\bar{Z}(H, u)$ (black dashed line) with the one calculated within the quadratic approximation (red solid line) in the interval $H \in [0, H_{\text{max}}(u)]$ for $u = 1$, i.e., for the case that the magnetization is parallel to the nematic director. It turns out that the difference between the exact generating function and its quadratic approximation increases with H but that it remains below 10% for the whole range of physically reasonable values of H . Thus the quadratic approximation in Eq. (3.25) provides a reasonable, at least qualitatively correct description of the free energy density of ferronematics.

The free energy-density obtained in the present study (Eq. (3.36)) and the one in Eq. (3.37) proposed in Ref. [102] share two main features: (i) In the absence of the

coupling between the magnetization \mathbf{M} and the nematic director \mathbf{n} , the suspension is in the paramagnetic phase, and (ii) the ferromagnetic properties are generated by a coupling of the magnetization and the nematic director via a term proportional to $(\mathbf{M} \cdot \mathbf{n})^2$. The comparison of the coefficients multiplying $(\mathbf{M} \cdot \mathbf{n})^2$ allows one to obtain an expression for the phenomenological coupling parameter γ (Eq. (3.37)) in terms of the microscopic coupling constant c (Eq. (3.38)). A slight inconsistency between the estimates for γ and for the anchoring energy W from Ref. [148] is found (Fig. 3.10). The reasons for this discrepancy encompass both the simplifications used in the present study (such as thin discs, monodisperse disc size, neglect of elastic pair interactions) as well as those applied in the theoretical model used in Ref. [148], e.g., the simplified form of the coupling of the director field to the colloid surface.

Chapter 4

Ferronematic slab in external magnetic fields

The behavior of a uniformly magnetized ferronematic slab is investigated numerically in a situation in which an external magnetic field is applied parallel and antiparallel, respectively, to its initial magnetization direction. The employed numerical method allows one to determine hysteresis curves, from which a critical magnetic field strength (i.e., the one at which the ferronematic sample becomes distorted) as function of the system parameters can be inferred. Two possible mechanisms of switching the magnetization by applying a magnetic field in the antiparallel direction are observed and characterized in terms of the coupling constant between the magnetization and the nematic director as well as in terms of the coupling strength of the nematic liquid crystal and the walls of the slab. Suitably prepared walls allow one to combine both switching mechanisms in one setup, such that one can construct a cell the magnetization of which can be reversibly switched off.

4.1 Introduction

Ferronematics, i.e., suspensions of anisotropic ferromagnetic particles dispersed in a nematic liquid crystal (NLC), attract both theoretical [94, 95, 153, 96, 154, 155, 97, 156] and experimental [100, 102, 148, 157, 158, 159] interest due to their ability to exhibit fluidity due to the solvent as well as macroscopic magnetization due to the colloidal inclusions. The anisotropic nature of the solvent implies broken rotational symmetry as compared to a simple isotropic liquid. The interaction of the anisotropic ferromagnetic colloids with the solvent depends on the orientation of the former with respect to the nematic director of the latter. As a result, the individual magnetic moments of the colloids become effectively trapped around the two possible orientations of the nematic order. Therefore, suitably prepared samples can exhibit a macroscopically ferromagnetic phase. The phase

behavior of this complex system follows from its free energy density. The authors of Ref. [102] proposed a phenomenological expression thereof which is formulated in terms of the magnetization \mathbf{M} and the nematic director \mathbf{n} . A similar expression was derived analytically starting from a microscopic description of the system [160]:

$$f(\mathbf{M}, \mathbf{n}) = \frac{a}{2} |\mathbf{M}|^2 - \frac{1}{2} \gamma \mu_0 (\mathbf{M} \cdot \mathbf{n})^2 - \mathbf{M} \cdot \mathbf{B} \quad (4.1)$$

where $\mu_0 = 4\pi \times 10^{-7}$ N/A² is the permeability of vacuum, $a > 0$ is a constant which depends on properties of both the nematic medium and the colloids (for an explicit form see Ref. [160]), $\gamma \geq 0$ measures the coupling between the magnetization and the nematic director, and $\mathbf{B} = B\mathbf{e}_x$ is the external magnetic field. Note that here γ is independent of the magnetization \mathbf{M} , i.e., Eq. (4.1) describes the coupling between \mathbf{M} and \mathbf{n} to lowest order in \mathbf{M} . Both a and γ are functions of the microscopic coupling constant $c := WR/K$ where W is the anchoring strength measuring the interaction energy of the NLC per surface area of a single colloid, R is the radius of a colloidal particle modeled as a thin disc (i.e., a disc whose thickness is much smaller than its radius such that the interaction of the rim with the NLC medium can be disregarded), and K is the elastic constant of the NLC within the one-elastic-constant approximation. (The value of $K = 3.5 \times 10^{-12}$ N, corresponding to the twist elastic constant of 5CB [148], is used throughout the current study if not specified otherwise.)

One of the interesting results of the experiments reported in Ref. [102] was the observation of a complex response of the ferronematic slab to a uniform external magnetic field, which depends on the initial state of the sample: If, on one hand, the sample was prepared by quenching the NLC solvent from the isotropic into the nematic phase in the absence of an external magnetic field, the colloids formed *various* magnetic domains within which $\mathbf{M} \parallel \mathbf{n}$. If, on the other hand, the NLC solvent was quenched in the presence of a uniform magnetic field, a *single* domain formed with the entire sample being magnetized in one direction with $\mathbf{M} \parallel \mathbf{n}$. Applying thereafter a uniform external magnetic field opposite to the direction of the magnetization of the single-domain sample yielded a complex, optically observable response of a nonuniform director field.

Here we focus on the case of single-domain samples. So far such samples have been thoroughly investigated theoretically in the situation in which the external magnetic field is applied *perpendicular* to the initial magnetization of the sample [94, 95, 154]. Also the dynamics of such a configuration was investigated experimentally [161, 162, 163]. A *thresholdless* distortion of the nematic was observed. Moreover, the authors of Refs. [94, 95, 154] considered infinitely strong anchoring at the walls and external magnetic fields up to magnitudes strong enough to directly interact with the magnetically anisotropic NLC molecules.

Our aim is to investigate in detail the behavior of a monodomain sample exposed to

a uniform external magnetic field which is applied in the direction *antiparallel* to the initial magnetization. Moreover, we consider only magnetic fields of small (≤ 25 mT) amplitudes, such that the direct magnetic field influence on the NLC can be neglected. It was observed experimentally [102, 148] that, like for common ferromagnets, ferronematics exhibit hysteresis in the magnetic properties as a function of the external field. Moreover, the critical field, i.e., the magnetic field strength at which the ferronematic becomes distorted (for a more precise definition see Sec. 4.3.1 below), is another feature of the ferronematic sample. We obtain the hysteresis curves numerically by using a conjugate-gradient technique in order to minimize an appropriate free energy functional of the ferronematic in slab geometry. From the hysteresis curves one can infer the value of the critical magnetic field as function of the parameters of the model and compare them with the expressions derived in Ref. [102]. In our previous study [160] we derived the dependence of the coupling parameter γ on the microscopic coupling c which in turn depends on the particle size. Having obtained the critical field as a function of γ allows us to relate it to the size of the colloids and therefore one can potentially tune the value of the critical field by tuning the mean of the size distribution of the particles used.

It turns out that the switching process of the considered ferronematic slab from one phase to the other takes place according to one of two possible scenarios which we shall discuss. In the first scenario, regions nucleate near the system walls in which the magnetization is flipped, whereas the nematic director is kept in place by the walls. In the second scenario, the nematic director follows the magnetization, i.e., it makes a full rotation by 180° , everywhere throughout the sample.

Finally, we propose a novel technique which can be used, e.g., in data storage devices. It is based on magnetic fields which control the magneto-optical properties of ferronematic cells, and thus allows one to switch between magnetized and demagnetized states by applying a uniform magnetic field of suitable orientation.

The chapter is organized as follows. In Sec. 4.2 we introduce the free energy functional in order to describe the system and the numerical method to minimize it. Section 4.3.1 contains the description of the first of the two switching mechanism as well as the results concerning the critical magnetic field and its dependence on the parameters of the model. In Sec. 4.3.2 we present the second switching mechanism and provide a map which relates the parameters of the model to the character of the switching. In Sec. 4.3.3 we report that a combination of the two mechanisms leads to a sample the magnetization of which can be reversibly switched off by using the external magnetic field. The role of the phenomenon of segregation is discussed in Sec. 4.4. In Sec. 4.5 we conclude the chapter by discussing the main results.

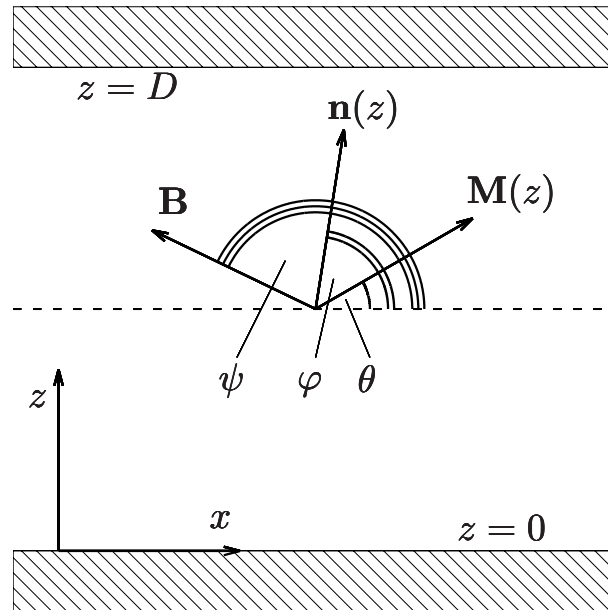


Figure 4.1: Sketch of a ferronematic in a slab of width D . The x -direction corresponds to the (lateral) easy direction of the liquid crystalline medium. Due to lateral translational invariance, all profiles depend only on the normal coordinate z . The nematic director $\mathbf{n}(z)$, the magnetization $\mathbf{M}(z)$, and the external magnetic field \mathbf{B} are parallel to the x - z -plane and their directions with respect to the positive x -direction are described by the angles $\varphi(z)$, $\theta(z)$, and ψ , respectively.

4.2 Numerical model

We consider the experimental setup studied in Ref. [102]. It consists of a ferronematic confined by two parallel and planar walls at a distance D with \mathbf{e}_x as the so-called easy axis at both surfaces, which imposes a parallel orientation of the nematic director there (see Fig. 4.1). We assume that the sample was prepared in the presence of a homogeneous external magnetic field $\mathbf{B} = B\mathbf{e}_x$ in the direction parallel to the easy axis \mathbf{e}_x of the walls (i.e., $B > 0$), thus producing a single domain of the ferromagnetic phase. In the following the effect of applying an external magnetic field in the direction opposite to the one used during this preparation (i.e., $B < 0$) is investigated numerically. The system is described by two spatially varying fields: the director field $\mathbf{n}(\mathbf{r})$ and the magnetization field $\mathbf{M}(\mathbf{r})$. We assume the absolute value of the magnetization is spatially constant, $|\mathbf{M}(\mathbf{r})| = \text{const} = m\rho_{\text{iso}}$ (where m is the absolute value of the magnetic moment of a single colloid, here taken to be 3×10^{-18} A m² [102], and ρ_{iso} is the number density of the colloids dispersed in the isotropic phase of the liquid crystal during the preparation of the sample (see Refs. [102] and [160]), i.e., segregation effects are assumed to be small [164]. (For a discussion of the possible influence of segregation see Sec. 4.4.) Due to translational invariance in the lateral x - y -plane all physical quantities depend on the

normal coordinate z only. We consider that both $\mathbf{n}(z)$ and $\mathbf{M}(z)/(m\rho_{\text{iso}})$ are parallel to the x - z -plane [165], so that they can be described by the angles $\varphi(z)$ and $\theta(z)$, respectively (see Fig. 4.1). The initial configuration is given by the uniform profiles $\varphi(z) = 0$ and $\theta(z) = 0$, which corresponds to an unstable state when a uniform magnetic field \mathbf{B} is applied in the direction $\psi = \pi$ (see Fig. 4.1). In terms of the profiles φ and θ the free energy functional of the system is given by

$$\frac{1}{S}\beta\mathcal{F}[\varphi, \theta] = \beta F_{\text{ferr}}[\varphi, \theta] + \beta F_{\text{elas}}[\varphi] + \beta F_{\text{surf}}[\varphi], \quad (4.2)$$

where S is the surface area of one of the glass plates, $\beta := 1/(k_{\text{B}}T)$,

$$\beta F_{\text{ferr}}[\varphi, \theta] = \int_0^D dz \beta f(\mathbf{M}(z), \mathbf{n}(z)) \quad (4.3)$$

with the free energy density f given by Eq. (4.1), which is the contribution due to the *ferronematic*,

$$\beta F_{\text{elas}}[\varphi] = \frac{1}{2}\beta K \int_0^D dz \left(\frac{d\varphi(z)}{dz} \right)^2, \quad (4.4)$$

is the contribution due to the elastic distortions of the liquid crystal, and

$$\beta F_{\text{surf}}[\varphi] = -\frac{1}{2}\beta W_{\text{wall}} (\cos(\varphi(0))^2 + \cos(\varphi(D))^2) \quad (4.5)$$

is the contribution due to the coupling of the liquid crystal to the glass plates.

The equilibrium profiles $\varphi(z)$ and $\theta(z)$ correspond to the minimum of the free energy in Eq. (4.2), which has been determined numerically by using the Fletcher-Reeves-Polak-Ribiere general function minimization algorithm [111]. The absolute value $|\mathbf{M}|$ of the magnetization is assumed to have a constant value $m\rho_{\text{iso}}$ and is taken to be independent of the external field \mathbf{B} throughout Sec. 4.3. For the discussion of the problem in the case of a spatially varying $|\mathbf{M}|$ see Sec. 4.4.

We have used the following parameter values: $K = 3.5 \times 10^{-12}$ N, $\rho_{\text{iso}} = 1.5 \times 10^{19}$ m⁻³, $m = 3 \times 10^{-18}$ A m², and $T = 300$ K. These values are consistent with experimental data reported in Refs. [102, 148]. The thickness D of the slab is taken to be 20 μm throughout Sec. 4.3. Thicker slabs are considered in Sec. 4.4 [166, 90].

4.3 Results

4.3.1 Switching mechanism I and the critical field

The experiments in Refs. [102, 148] demonstrate that, upon applying a uniform external magnetic field to the setup described in Sec. 4.2 (see also Fig. 4.1), there is a nonvanishing critical magnetic field strength $\mathbf{B}_{\text{cr}} = B_{\text{cr}}\mathbf{e}_x$ such, that for $B < B_{\text{cr}} < 0$ ($B > B_{\text{cr}} > 0$) in the case of an initial magnetization pointing along the positive (negative) x -direction,

elastic distortions of the liquid crystal matrix occur. The occurrence of such a critical magnetic field strength B_{cr} can be explained qualitatively in terms of a diverging relaxation time of the fluctuations of the nematic director field \mathbf{n} (or φ) (see Ref. [102]). Here we aim at exploring the dependence of B_{cr} on the coupling constant γ and the wall anchoring strength W_{wall} [167]. Moreover, we are also interested in the intermediate metastable states preceding the switches of the magnetization field \mathbf{M} to the ground state parallel to the external field \mathbf{B} .

Figure 4.2 shows the hysteresis curve of the spatially averaged projection of the magnetization \mathcal{M} onto the x -axis,

$$\mathcal{M} := \frac{1}{D} \int_0^D dz \cos \theta(z), \quad (4.6)$$

as function of the component of the external magnetic field \mathbf{B} along the x -axis for the particular choice of the coupling constant $\gamma = 240$ (which corresponds to a value of the microscopic coupling constant $c \approx 0.035$ [160]) and of the wall anchoring strength $W_{\text{wall}} = 3.1 \times 10^{-5} \text{ J/m}^2$; this choice of the parameters is reasonable in the context of available experimental data (see Refs. [102], [148], and [160]). In order to investigate the switching process of the magnetization in the ferromagnetic phase as function of the external magnetic field, Fig. 4.3 displays the orientation profiles $\varphi(z)$ and $\theta(z)$ for a series of intermediate metastable states corresponding to the hysteresis loop in Fig. 4.2.

For initially saturated samples with $\mathcal{M} = 1$, the magnetization does not change significantly in the presence of x -components of the magnetic field $B > B_{\text{cr}}$, whereas for $B < B_{\text{cr}}$ there is a noticeable deviation of the x -component of the spatially averaged magnetization \mathcal{M} from the initial saturation value (see Fig. 4.2). This defines a critical magnetic field strength $B_{\text{cr}} < 0$. For $B > B_{\text{cr}}$ both the magnetization and the nematic director field profiles, i.e., $\theta(z)$ and $\varphi(z)$, de facto do not deviate from the saturated ones (see Fig. 4.3(a)). While the magnetization tends to align with the external magnetic field, due to the interaction described by the coupling constant γ it is dragging the nematic director field along. At $B = B_{\text{cr}}$ the metastable state corresponding to the unperturbed nematic director becomes unfavorable compared to the metastable state corresponding to the perturbation induced in the interior of the slab (see Fig. 4.3(b)). We note that the saturated sample with $\mathcal{M} = 1$ in a magnetic field in the negative x -direction with $B = B_{\text{cr}}$ corresponds to a saddle point of the free energy so that spontaneous symmetry breaking induced by fluctuations leads to perturbations of the magnetization orientation profile $\theta(z)$ with either $\theta(z) > 0$ or $\theta(z) < 0$. In the following we focus only on the first case, while the second, conjugated one, follows from changing signs. It is the perturbed nematic director field which manifests itself as a brightening of the sample when viewed with crossed polarizers as in the experiment reported in Ref. [102], and it occurs only due to the coupling of the magnetization field \mathbf{M} to the nematic director field \mathbf{n} . The external

magnetic field imposes a torque onto the magnetization field which in turn leads to a torque onto the nematic director field. The latter is opposing the torque generated by the walls of the cell and which is transmitted due to the elasticity of the NLC (Eq. (4.4)). Upon increasing the external magnetic field the variations inside the slab become more and more pronounced for both the magnetization and the nematic director field. However, in the case of soft anchoring [168] (distinct from the case of infinitely strong anchoring, see Ref. [85]) at the surface of the colloid, the angle between the magnetization and the nematic director is nonzero for $B < B_{\text{cr}}$ (see Figs. 4.1 and 4.3), i.e., $\theta \neq \varphi$.

Before reaching the magnetic phase with the sample being magnetized along the field in negative x -direction, the system passes through the metastable state (3) in Fig. 4.2, in which the magnetization profile $\theta(z)$ has a peculiar form (see Figs. 4.3(c) and 4.4). In this metastable state the magnetization in the interior of the sample is aligned along the magnetic field. Within certain transition regions close to the walls the orientation of the magnetization interpolates between the direction along the magnetic field and the opposite direction. These transition regions occur because the magnetization is coupled to the nematic director field, which is aligned along the easy axis ($\varphi = 0$) at the walls. The width of these transition regions grows upon increasing the external magnetic field strength so that eventually the minimum of the free energy given by Eq. (4.2) corresponds to the magnetization being oriented parallel to the external magnetic field in the entire slab ($\theta = \pi$). Concerning the transition regions following observations can be made: (i) Due to the soft coupling between the colloids and the nematic director field of the NLC the ground state, in which the entire sample is magnetized along the external field, is attained by means of “switching” the magnetization locally, i.e., by inverting the direction of the magnetization (and thus of the orientation of the magnetic colloids) without the simultaneous rotation of the local nematic director field [169]. (ii) Layers of the incipient ferronematic phase are nucleated in the regions close to the walls due to the interplay between elastic and magnetic torques and because the coupling energy is invariant with respect to an inversion of the magnetization.

Naturally the question arises concerning the dependences of the critical magnetic field strength B_{cr} on the coupling constant γ and on the wall anchoring W_{wall} . Here we define B_{cr} as the magnetic field strength at which the spatially averaged magnetization \mathcal{M} equals 0.97; note that $\mathcal{M} = 1$ in the saturated state. This definition differs from the one used in Refs. [102, 148], where B_{cr} is defined as the magnetic field strength at which the relaxation time of thermal fluctuations of the direction of \mathbf{n} diverges. Here we do not consider dynamic processes, instead we propose the above alternative definition of B_{cr} . Obviously, the choice of 0.97 for the threshold value contains some degree of arbitrariness. However, as can be inferred from the steep slope of the hysteresis loop close to state (1) in Fig. 4.2, no significant changes are expected to occur by choosing different threshold

values not too much less than unity. Figure 4.5 shows the dependence of B_{cr} on the coupling constant γ and the wall anchoring strength W_{wall} . One can infer from Fig. 4.5 that for fixed W_{wall} the critical field B_{cr} increases upon increasing γ . Indeed, for a given value of W_{wall} , the magnetization field is aligned with the nematic director field, the rotation of which is opposed by the torque imposed by the walls. The system sustains the alignment for increasing external magnetic field strengths which in their turn are due to an increasing strength of the coupling γ between the magnetization and the nematic director field. One can also infer from Fig. 4.5 that the critical field B_{cr} depends rather weakly on the wall anchoring strength W_{wall} : Within the considered range of the anchoring strengths, $W_{\text{wall}} \in [0.5 \times 10^{-5}, 10 \times 10^{-5}] \text{ J/m}^2$, for fixed γ the critical field strength B_{cr} varies by $\approx 0.1 \text{ mT}$. For large values of W_{wall} the critical field reaches a plateau (see Fig. 4.6 (a)) and it becomes independent of the wall anchoring W_{wall} .

Figure 4.6 illustrates these trends of the critical magnetic field strength B_{cr} via cuts in Fig. 4.5 for $\gamma \approx 195$ (see Fig. 4.6(a)) and $W_{\text{wall}} = 4 \times 10^{-5} \text{ J/m}^2$ (see Fig. 4.6(b)). Moreover, Fig. 4.6(c) displays the dependence of B_{cr} on the microscopic coupling constant c (see below Eq. (4.1)). Finally, Fig. 4.6(b) compares the values of the critical magnetic field B_{cr} as defined in the present approach (circles) with the corresponding expression given in Ref. [102],

$$B_{\text{cr}}^{[102]} = \frac{\pi^2 \gamma \mu_0 K M_s}{\pi^2 K + \gamma \mu_0 M_s^2 D^2}, \quad (4.7)$$

where $M_s := m\rho_{\text{iso}}$ is the magnetization of the saturated sample, obtained in the limit $W_{\text{wall}} \rightarrow \infty$. (Here, we consider the particular NLC used for the experiments in Refs. [102, 148] and therefore a fixed value of the elastic constant K . Although the variation of the expression given here as function of the elastic constant of the NLC is interesting, we leave this issue for future work due to the highly non-trivial occurrences of K .) Remarkably, $B_{\text{cr}} \approx B_{\text{cr}}^{[102]}$ appears to hold although the two definitions of the critical magnetic field strength differ and although $B_{\text{cr}}^{[102]}$ in Eq. (4.7) does not take the dependence on W_{wall} into account.

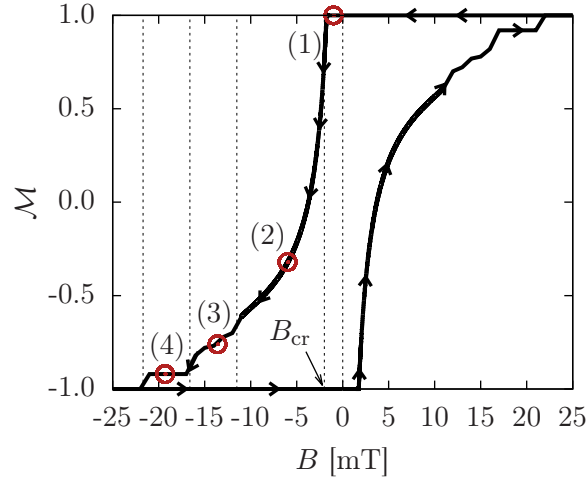


Figure 4.2: Hysteresis of the spatially averaged magnetization \mathcal{M} along the x -direction (see Eq. (4.6)) of the ferronematic slab as function of the x -component B of the external magnetic field \mathbf{B} . Negative values of \mathcal{M} or B correspond to orientations in the negative x -direction (see Fig. 4.1). For initially saturated samples with $\mathcal{M} = 1$ (i.e., magnetized in the positive x -direction) there is a nonvanishing critical magnetic field $B_{\text{cr}} < 0$ (indicated in the plot) such that for $B \in [B_{\text{cr}}, 0]$ the magnetization \mathcal{M} does not respond to the external field. Upon increasing the field in the negative x -direction (i.e., for $B < B_{\text{cr}}$, left branch of the loop) the system evolves through a series of qualitatively distinct metastable states (red circles) corresponding to the profiles displayed in Fig. 4.3 and eventually reaches saturation along the negative x -direction (i.e., $\mathcal{M} = -1$). Gradually lowering the magnitude $|B|$ of the magnetic field does not influence the magnetization of the sample (i.e., for $B < 0$, see the part of the loop along $\mathcal{M} = -1$). After $B = 0$ is crossed, the situation is identical to the one described above up to a change of sign of B and \mathcal{M} (right branch of the loop). Dotted vertical lines separate regions of qualitatively different metastable states. Note that state (1) corresponds to $B_{\text{cr}} < B < 0$. $W_{\text{wall}} = 3.1 \times 10^{-5} \text{ J/m}^2$, $\gamma = 240$, $K = 3.5 \times 10^{-12} \text{ N}$, $\rho_{\text{iso}} = 1.5 \times 10^{19} \text{ m}^{-3}$, $m = 3 \times 10^{-18} \text{ A m}^2$, and $T = 300 \text{ K}$

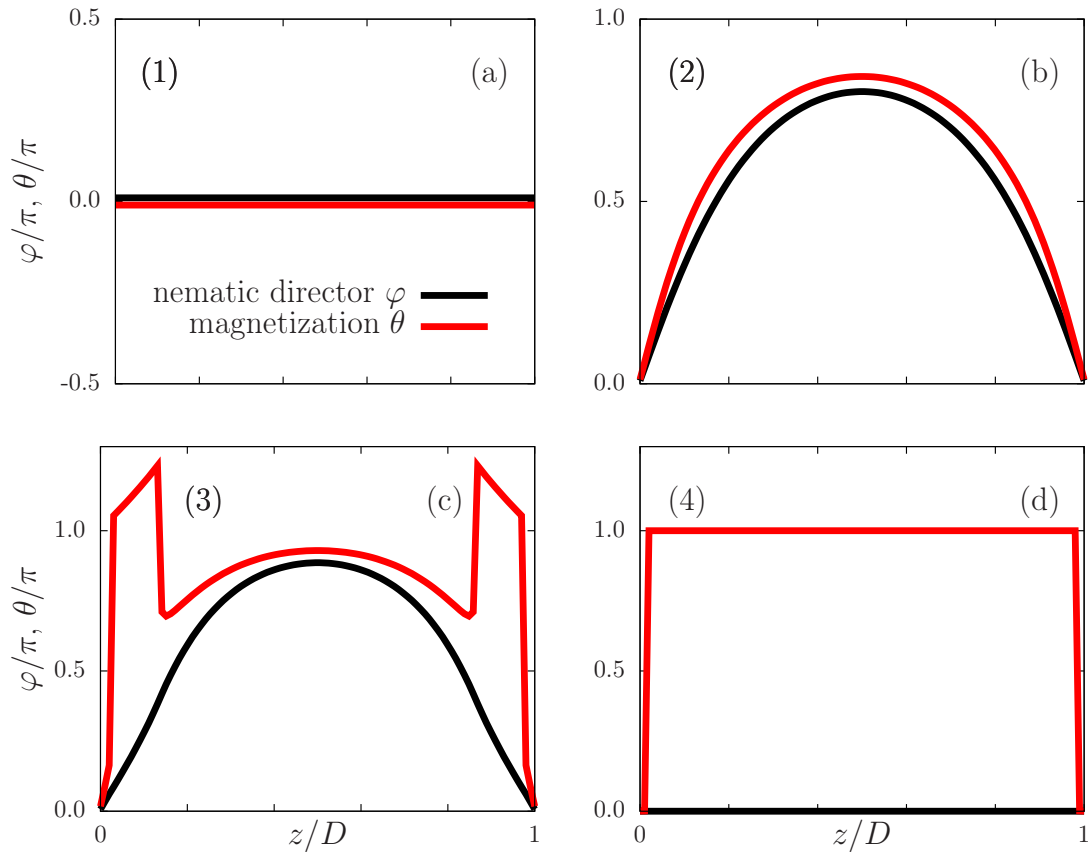


Figure 4.3: Qualitatively distinct metastable states of the ferronematic along the hysteresis curve in Fig. 4.2 in terms of the profiles $\varphi(z)$ of the nematic director field (black lines) and $\theta(z)$ of the local magnetization (red lines). State (1) (see the numbered states in Fig. 4.2): For magnetic fields B along the x -direction with components $B > B_{\text{cr}}$ the saturated profiles $\mathcal{M} = 1$ are unperturbed by B . State (2): For magnetic field components $B < B_{\text{cr}}$ both profiles deviate significantly from the saturated ones. Note that the profiles in panel (1) correspond to a saddle point of the free energy so that spontaneous symmetry breaking can occur from state (1) to state (2) (i.e., the magnetization and the director start to rotate in either clockwise or counterclockwise direction, see Fig. 4.1). The equally probable profiles which correspond to the same projection \mathcal{M} and thus correspond to the same points (1)-(4) on the hysteresis loop (see Fig. 4.2), are obtained by the map $(\varphi, \theta) \mapsto (-\varphi, -\theta)$ for the profiles (a)-(d). State (3): Upon further increasing the magnetic field strength in the negative x -direction, layers form near the walls where the magnetization interpolates between the direction along (θ large) and opposite (θ small) to the magnetic field. The coupling of the magnetization and the director causes $\theta > \pi$ within the layers. State (4): For even stronger magnetic fields the entire slab (besides thin layers near the walls, which require yet higher fields to switch) is magnetized along the direction of the magnetic field, i.e., $\theta = \pi$. The values of the system parameters are the same as in Fig. 4.2.

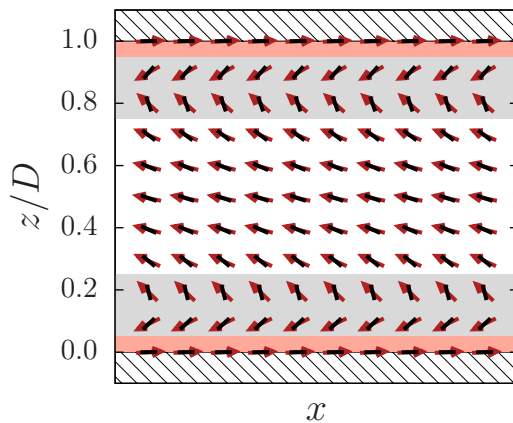


Figure 4.4: Explicit magnetization field (red arrows) and nematic director field (black rods) of the pretransitional metastable state (3) (see Figs. 4.2 and 4.3(c)) of the ferronelectric in between two glass walls (hatched regions). While in the interior of the slab (white region) the magnetization field (red arrows) is, to a large extent, aligned with the external magnetic field in the negative x -direction, close to the walls (grey regions) its orientation interpolates between the configurations being parallel and antiparallel to the magnetic field. This is due to the coupling to the nematic director field (black rods), which is aligned along the easy direction at the walls. Upon further increasing the strength of the external magnetic field in the negative x -direction ($B < B_{\text{cr}} < 0$), the grey regions widen and eventually produce an almost uniformly magnetized sample (see Fig. 4.3(d)). The pale red regions denote thin layers very close to the walls which switch last.

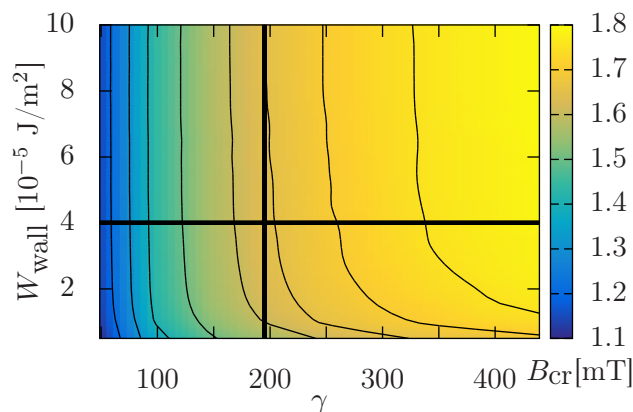


Figure 4.5: The dependence of the critical magnetic field strength B_{cr} on the coupling constant γ and on the anchoring strength W_{wall} at the walls. The color code denotes values of B_{cr} measured in units of mT. The thin black curves are contour lines; from left to right $B_{\text{cr}} = 1.2, 1.3, 1.4, 1.5, 1.6, 1.65, 1.7, 1.75$ mT. The thick black lines correspond to the cuts in Fig. 4.6(a) and (b) for $\gamma \approx 195$ and $W_{\text{wall}} = 4 \times 10^{-5} \text{ J/m}^2$, respectively (the values of the remaining parameters are the same as in Fig. 4.2).

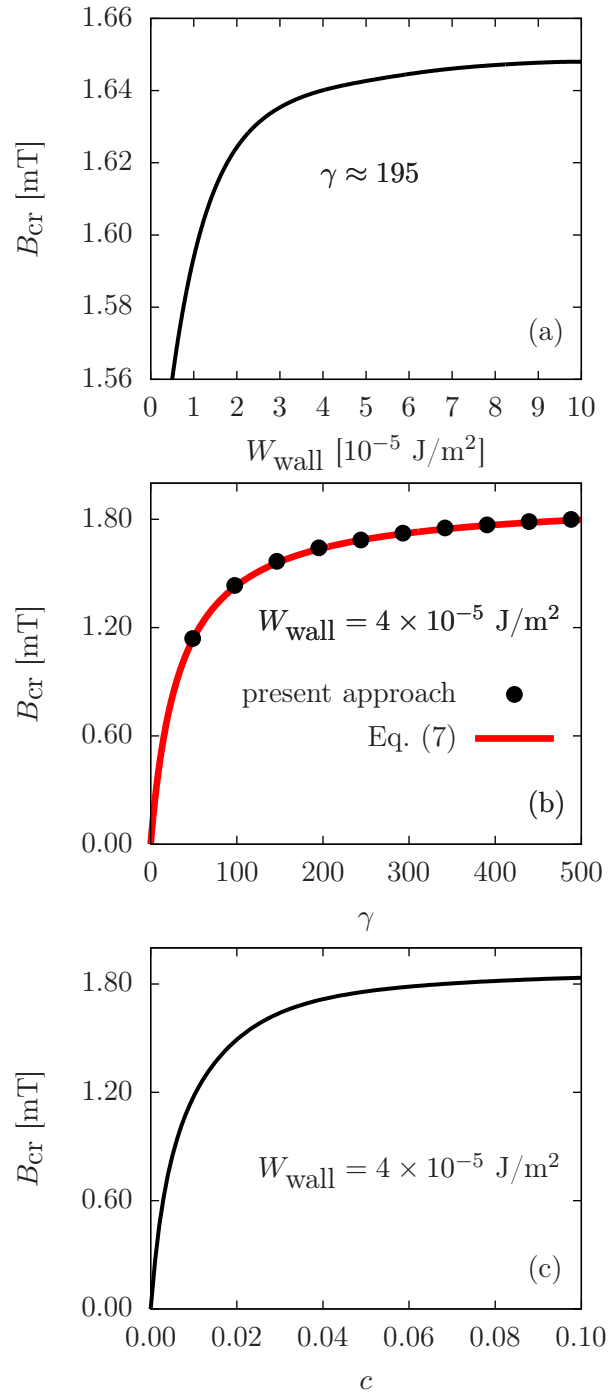


Figure 4.6: Dependence of the critical magnetic field strength B_{cr} (a) on the wall anchoring strength W_{wall} (along the thick vertical black line in Fig. 4.5, i.e., for $\gamma \approx 195$), (b) on the coupling constant γ (present approach and Eq. (4.7) along the thick horizontal black line in Fig. 4.5, i.e., for $W_{\text{wall}} = 4 \times 10^{-5}$ J/m 2), and (c) on the microscopic coupling constant c (see below Eq. (4.1), $W_{\text{wall}} = 4 \times 10^{-5}$ J/m 2). The values of the remaining parameters are the same as in Fig. 4.2.

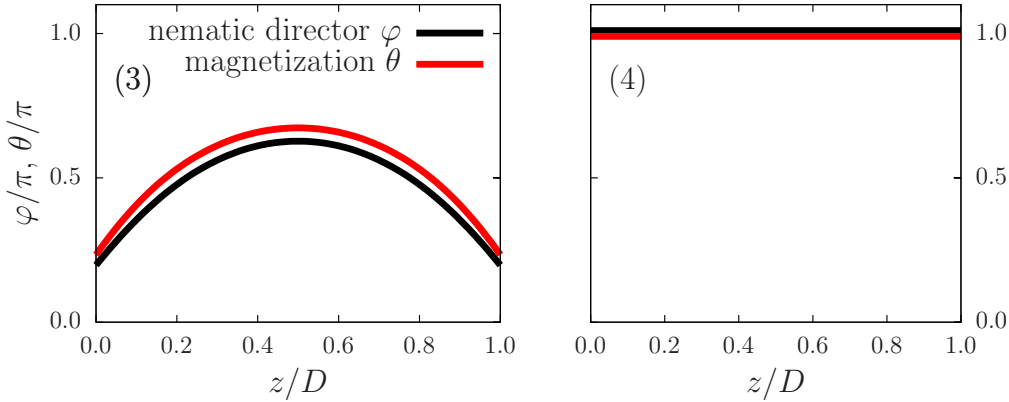


Figure 4.7: Final two stages of switching mechanism II for the magnetization in an initially oppositely oriented external magnetic field for $\gamma = 240$ and $W_{\text{wall}} = 0.1 \times 10^{-5} \text{ J/m}^2$ (the values of the remaining parameters are the same as in Fig. 4.2). It is characterized by a nematic director field with significant elastic distortions throughout the sample. Even at the surface rotations of the nematic director with respect to the easy axis occur due to the weak anchoring at the walls (note $\varphi \neq 0$ and $\theta \neq 0$ in the left panel). For sufficiently strong magnetic fields both the magnetization field and the nematic director rotate by the angle π (see right panel). The panels are denoted by “(3)” and “(4)” in order to make the comparison easier with the corresponding panels in Fig. 4.3 describing switching mechanism I. Note that $\theta \neq \varphi$ even directly at the walls.

4.3.2 Switching mechanism II

In Sec. 4.3.1 we revealed a mechanism of switching the sample magnetization in the case of large values of the wall anchoring strength W_{wall} . Here we show another possible mechanism which corresponds, however, to small values of W_{wall} . For suitable combinations of γ and W_{wall} the magnetization field is able to drag the nematic director field along, thereby inducing a large change of the angle φ compared with the initial configuration. For small values of W_{wall} the anchoring at the wall is so weak, that the nematic director field at the surface of the walls is able to deviate from the direction of the easy axis and to rotate with the magnetic field due to the coupling between the magnetization and the nematic director.

We have performed calculations analogous to those described in Sec. 4.3.1 but for small values of the anchoring strength W_{wall} at the sample walls. It turns out that for values $W_{\text{wall}} < 0.5 \times 10^{-5} \text{ J/m}^2$ there are corresponding values of the coupling constant γ which produce a switching mechanism which is qualitatively different from the one described in the previous section. In this mechanism the early stages of the switching are similar to those described in the previous section (see Fig. 4.3(1) and (2)). However, the subsequent stage, as displayed in Fig. 4.7(3), is qualitatively different in the sense that the system does not separate in distinct spatial regions with different orientations of

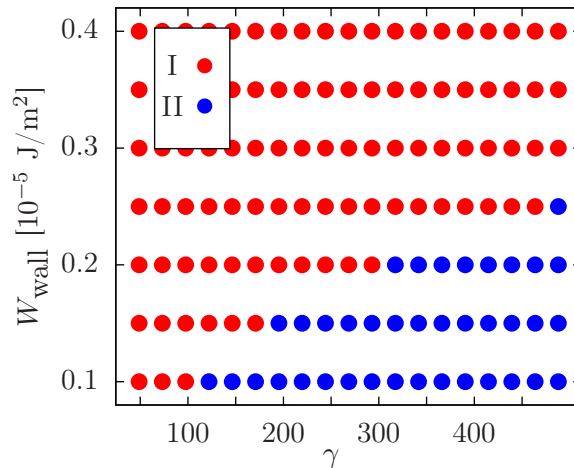


Figure 4.8: Regions of dominance for the two switching mechanisms between two ferromagnetic phases in terms of the coupling constant γ and the wall anchoring strength W_{wall} , which is the same for both walls. (The values of the remaining parameters are the same as in Fig. 4.2.) The region denoted as "I" (full red circles) corresponds to switching mechanism I in which the magnetization leaves the nematic director field behind (see Sec. 4.3.1). The region denoted as "II" (full blue circles) corresponds to switching mechanism II in which the nematic director field is weakly coupled to the sample walls and therefore is able to follow the magnetization.

the magnetization (compare with Fig. 4.3(3)). Obviously, the change in character of the switching mechanism is directly related to the anchoring at the walls being too weak to prevent the liquid crystal from rotating along with the magnetization field. This weakness is revealed also by nonzero angles φ and θ at the walls.

At such low anchoring strengths the torque imposed on the liquid crystal director by the walls cannot compete with the drag imposed by the rotating magnetization field and it is energetically more favorable for the director at the walls to flip its orientation. The regions of dominance for the two switching mechanisms are depicted in Fig. 4.8, where a map spanned by the coordinates $(\gamma, W_{\text{wall}} = W_{\text{wall}}^{(1)} = W_{\text{wall}}^{(2)})$ marks region "I" (corresponding to switching mechanism I, for which the director field returns back to its initial configuration upon increasing the external magnetic field and reaching the saturation of the magnetization in the direction of the field) and region "II" (corresponding to switching mechanism II, for which the director field follows the magnetization). Within our numerical approach switching mechanism II is observed only for values of the wall anchoring W_{wall} which are significantly smaller than the one estimated from the experiment [148], i.e., $W_{\text{wall}}^{\text{exp}} \approx (3.40 \pm 0.11) \times 10^{-5} \text{ J/m}^2$. Therefore, we expect switching mechanism I to be the one realized experimentally.

The segregation of colloids might play an important role. Segregation amounts to a redistribution of the colloids dispersed in the liquid crystal. This effect is caused by the

opportunity to lower the free energy of the magnetic colloids in an external magnetic field by migrating away from regions in which the liquid crystal prevents alignment along the external field. Thereby energy is gained by accomplishing alignment at the expense of the entropic contribution due to denser packing which is proportional to $\rho \log \rho$, where ρ is the local number density of the colloids (see Ref. [160]). Although segregation is neglected in Sec. 4.3, we nonetheless do not expect segregation to influence our results qualitatively (see Sec. 4.4). On the other hand, quantitative changes are conceivable, i.e., the map in Fig. 4.8 might be affected.

4.3.3 Confining walls with different anchoring strengths

In this section we study a combination of switching mechanisms I and II described in Secs. 4.3.1 and 4.3.2, respectively, by considering a strong anchoring strength at one wall and a weak one at the other, sharing the same easy axis. Thus the system is described by three parameters (assuming a , T , K , D , m , and ρ_{iso} to be fixed): (i) coupling constant γ , (ii) the anchoring strength at one of the walls, and (iii) the ratio of the anchoring strengths at the two walls. Note that introducing different but still uniform and parallel anchorings at the walls renders the system still effectively one-dimensional along the z -direction and hence from a numerical point of view its complexity does not change.

Adding a third parameter (i.e., the ratio of the anchoring strengths at the two walls $w := W_{\text{wall}}^{(1)}/W_{\text{wall}}^{(2)}$) introduces a third dimension to the map considered in Fig. 4.8. The cut of this three-dimensional map along $w = 1$ produces the two-dimensional map shown in Fig. 4.8. While the two-dimensional map in Fig. 4.8 exhibits only two switching regions (I and II), in the three-dimensional parameter space the situation can be more involved. It is reasonable to expect that if both $W_{\text{wall}}^{(1)}$ and $W_{\text{wall}}^{(2)}$ become infinitely strong, the magnetization of the sample switches according to mechanism I. If, on the other hand, $W_{\text{wall}}^{(1)}, W_{\text{wall}}^{(2)} \rightarrow 0$ one can expect that the magnetization of the sample switches according to mechanism II. However, pairs $(W_{\text{wall}}^{(1)}, W_{\text{wall}}^{(2)})$ can exist such that the magnetization in the vicinity of one wall would switch according to mechanism I and the magnetization in the vicinity of the other wall would switch according to mechanism II. Thus, the three-dimensional parameter space consists of *three* regions: dominance of mechanism I, II, and their combination.

The line separating the two regions in Fig. 4.8 becomes a two-dimensional manifold in the three-dimensional parameter space $(W_{\text{wall}}^{(1)}, w, \gamma)$. In the vicinity of the plane $w = 1$ this manifold, which is separating the regions “I” and “II”, is considered to be perpendicular to the plane $w = 1$ and only the two regions “I” and “II” occur. Therefore, if one would like to find a point $(W_{\text{wall}}^{(1)}, w, \gamma)$ that belongs to the region, which corresponds to the combination of the two switching mechanisms, it is necessary to pick the value of w significantly different from 1. To this end, for fixed γ it seems to be natural to take as an

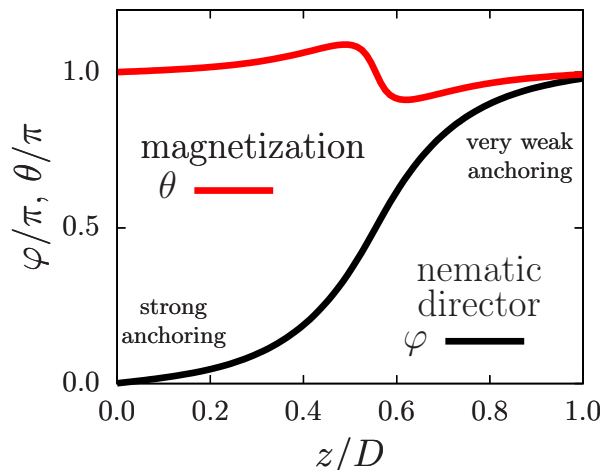


Figure 4.9: Orientation profiles $\varphi(z)$ (nematic director, black line) and $\theta(z)$ (magnetization, red line) for $B \leq -12$ mT (with the sample initially magnetized along the positive x -direction). There is a gradual variation of the nematic director from one wall to the other. The parameters are chosen as $\gamma = 240$, $W_{\text{wall}}^{(1)} = 10^{-5}$ J/m² (see $z = 0$), and $W_{\text{wall}}^{(2)} = 0.1 \times 10^{-5}$ J/m² (see $z = D$), $K = 9 \times 10^{-12}$ N [170]; the values of the remaining parameters are the same as in Fig. 4.2.

estimate the anchoring at one of the walls from region “I” in Fig. 4.8 and the anchoring at the other wall from region “II” in Fig. 4.8. It has turned out that for $D = 20$ μm (for a discussion concerning larger values of D see Sec. 4.4) the combination $W_{\text{wall}}^{(1)} = 10^{-5}$ J/m² and $W_{\text{wall}}^{(2)} = 0.1 \times 10^{-5}$ J/m² (i.e., $w = 10$) yields profiles $\varphi(z)$ (nematic director) and $\theta(z)$ (magnetization) which consist of one part due to switching mechanism I and another part due to switching mechanism II. Figure 4.9 shows the actual profiles (i.e., for magnetic field strengths $B \leq -12$ mT and for the initial magnetization pointing into the positive x -direction) of the magnetization and of the nematic director field for $\gamma = 240$, $W_{\text{wall}}^{(1)} = 10^{-5}$ J/m², and $W_{\text{wall}}^{(2)} = 0.1 \times 10^{-5}$ J/m², where superscript (1) denotes the wall at $z = 0$ and superscript (2) denotes the wall at $z = D$. Both the orientation field $\varphi(z)$ of the nematic director and the orientational field $\theta(z)$ of the magnetization have a nontrivial form. The nematic director field profile exhibits a smooth rotation by an angle of π from one wall to the other. According to Fig. 4.9, the wall with the strong anchoring at $z/D = 0$ is able to align the nematic director along the easy axis there ($\varphi = 0$), while the magnetization field is switching to the negative x -direction parallel to the external field (compare Sec. 4.3.1). On the other side, the weak anchoring at $z/D = 1$ in Fig. 4.9 allows the nematic director there to follow the magnetization ($\theta = \pi$ implies $\varphi = \pi$; compare Sec. 4.3.2). This provides a situation in which $\varphi = 0$ at one wall and $\varphi = \pi$ at the other. The elastic contribution in Eq. (4.4) ensures that no singularities occur in the interior of the slab so that there is a smooth crossover between the two boundary values.

In the middle ($z \approx 0.55D$) of the sample the magnetization field exhibits an interface

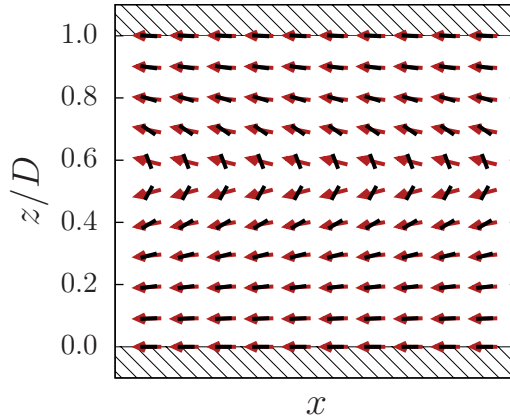


Figure 4.10: Vector fields corresponding to Fig. 4.9. The notation is the same as in Fig. 4.4. Note the distortion of the nematic director field (black rods) in the interior and the interface between two magnetization (red arrows) domains at $z \approx 0.55D$ due to the combination of the switching mechanisms I and II. Basically throughout the whole sample the magnetization has reached the switched state in negative x -direction. $\gamma = 240$, $W_{\text{wall}}^{(1)} = 10^{-5} \text{ J/m}^2$ (see $z = 0$), and $W_{\text{wall}}^{(2)} = 0.1 \times 10^{-5} \text{ J/m}^2$ (see $z = D$), $K = 9 \times 10^{-12} \text{ N}$ [170] (the values of the remaining parameters are the same as in Fig. 4.2).

between two halves of the slab (see Fig. 4.10). The orientation of the magnetization within the two halves differs only in how the magnetization approaches the value $\theta = \pi$ in the vicinity of the center of the slab. This behavior of the magnetization field profile is caused by the necessity to be compatible with the nematic director profile in the center region. This means that the rotation of the nematic director in the interior of the slab forces the magnetization direction to reach its value $\theta = \pi$ at $z \approx D/2$ either from $\theta > \pi$ at $z \lesssim D/2$ or from $\theta < \pi$ at $z \gtrsim D/2$ (see the red curve in Fig. 4.9). In the situation of Fig. 4.9, upon switching off the external magnetic field, we found that the system relaxes into a state with a uniform nematic director field and two domains with the magnetization pointing into opposite directions (see Fig. 4.11(c)) [170]. The position of the interface between these two domains depends on the position of the interface plane formed while the magnetic field was still on [171]. Application of the external magnetic field to the two-domain configuration opens up two possibilities: (i) If the external magnetic field is applied in the same direction as the field used to create the two-domain sample, the resulting state is identical to the one in Fig. 4.9. (ii) If, on the other hand, the magnetic field is applied opposite to the direction of the magnetic field used to create the two-domain sample, one of the domains (i.e., the one the magnetization of which is opposite to the external field) switches. This yields a uniform sample both in terms of the nematic director and the magnetization field, thus returning the system to its initial state. These steps are summarized in Fig. 4.11. Note that the states shown in Figs. 4.11 (a) and 4.11 (d) are identical. Also note that the state depicted in Fig. 4.11 (a) exhibits saturated magnetization $\mathcal{M} = 1$ (Eq. (4.6))

whereas the state depicted on Fig. 4.11 (c) exhibits $\mathcal{M} \ll 1$. Since one can restore the initial state (see Fig. 4.11 (a)) from the two-domain state (see Fig. 4.11(c)) by applying an external magnetic field $B > 0$, one is able to cycle through three states (see Figs. 4.11 (a), (b), and (c)). Accordingly, this ferronematic cell with two walls of different anchoring strength can be put in either of two states (i.e., magnetized or demagnetized) by using an external magnetic field of suitable direction. This opens up the possibility, e.g., to use an array of such cells for storage of binary information with a "bit" being represented by the state of the cell (magnetized/demagnetized) or as a spatially resolving magnetic field detector with memory function.

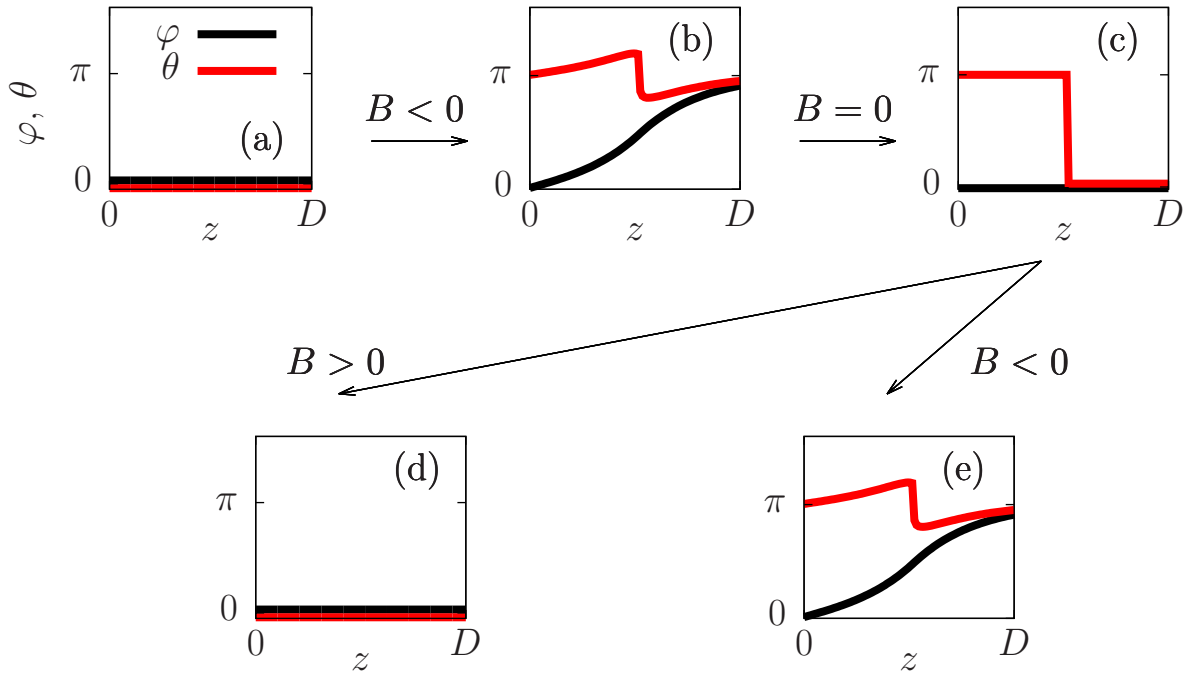


Figure 4.11: Orientational profiles $\varphi(z)$ (nematic director, black line) and $\theta(z)$ (magnetization, red line) in a ferronematic cell with walls of different anchoring strength, as discussed in Sec. 4.3.3. The initial state (a) is a uniformly magnetized ferronematic slab, i.e., the director field ($\varphi = 0$, black line) and the magnetization field ($\theta = 0$, red line) are uniform. Upon application of an external magnetic field $\mathbf{B} = B\mathbf{e}_x$ in the direction opposite to the initial magnetization direction (i.e., $B < 0$) transfers the sample into the disturbed state (b) (compare Fig. 4.9). After suddenly switching off the external field (i.e., for $B = 0$) the system relaxes into the state (c) in which the nematic director is uniform; that part of the sample, which is close to the wall with strong anchoring, retains its magnetization direction $\theta \approx \pi$ whereas the magnetization near the wall with weak anchoring follows the relaxation of the nematic director and attains $\theta = 0$. Thus having two halves of the sample being magnetized in opposite directions yields zero overall sample magnetization, i.e., $\mathcal{M} \ll 1$. This configuration offers two options: (i) The application of an external magnetic field in the direction of the initial magnetization (i.e., $B > 0$) returns the sample to the initial, uniform state (d)=(a) with magnetization $\mathcal{M} = 1$. (ii) The application of an external magnetic field in the direction opposite to the initial magnetization (i.e., $B < 0$) produces the disturbed state (e)=(b). The fact that the states (d) and (a) are identical allows one to cycle through the states (a), (b), and (c) by applying the external magnetic field \mathbf{B} in suitable directions. The width of the interface between two domains in (c) is not larger than the numerical grid discretization, i.e., less than $D/100$. The values of the parameters are the same as in Fig. 4.9.

4.4 Segregation effects

It was pointed out by Brochard and de Gennes [85] that anisotropic magnetic colloids tend to move away from regions of the NLC where distortions of the director field prevent

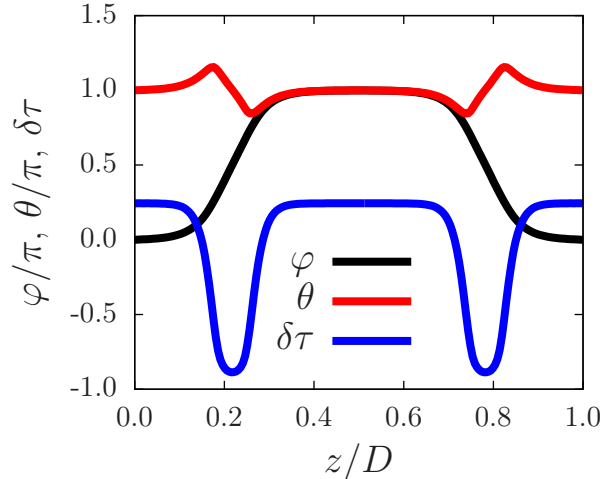


Figure 4.12: Results of the numerical minimization of the functional in Eq. (4.2) with segregation effects included (see Eqs. (4.12) and (4.13)). The sample thickness is $D = 120 \mu\text{m}$, the wall anchoring is $W_{\text{wall}} = 3.4 \times 10^{-5} \text{ J/m}^2$ for both walls, the coupling constant is $\gamma = 240$, the external magnetic field is $B = 4 \text{ mT}$, and $a \approx 3.1 \times 10^{-4} \text{ N/A}^2$. (The values of the remaining parameters are the same as in Fig. 4.2.) Due to the large thickness D of the cell the switching mechanism I is now combined with the switching mechanism II even in the case that both walls provide strong anchoring. The particles are expelled (see the blue solid line) from the regions with strong gradients of the nematic director field φ (black solid line). The depletion layers (i.e., the minima of the blue solid line) are separated from the walls due to the soft anchoring between the magnetization and the nematic director field. This differs from the situation described in Ref. [85] in which the depletion layer is located in close vicinity of the wall.

them from minimizing their free energy in the external magnetic field. The segregation parameter defined as (see Ref. [85])

$$s := \beta m B \quad (4.8)$$

is greater than unity already for $B \gtrsim 1.4 \text{ mT}$ and therefore one can expect segregation to occur for external fields stronger than 1.4 mT . In the following we investigate the impact of segregation on the switching mechanisms I and II.

The present theoretical approach (see Eqs. (4.1) and (4.2)) includes the possibility of segregation to occur through the dependence of the magnetization field \mathbf{M} on the spatial coordinate z . In particular, we are interested in spatial inhomogeneities of the *absolute value* $|\mathbf{M}(z)|$ of the magnetization vector. It is convenient to introduce the dimensionless quantity $\tau(z) := |\mathbf{M}(z)|/(m\rho_{\text{iso}})$. So far all our results have been obtained in the limit $\tau(z) = \text{const} = 1$. If $\tau(z) \neq 1$, that part of the free energy density, which depends on it

(see Eq. (4.1) and Fig. 4.1), is given by

$$\begin{aligned} \beta f(\theta(z), \varphi(z), \tau(z)) = & \\ & \beta(m\rho_{\text{iso}})^2 \tau(z)^2 \left(\frac{a}{2} - \frac{1}{2} \gamma \mu_0 \cos(\theta(z) - \varphi(z)) \right)^2 \\ & - \beta m \rho_{\text{iso}} B \tau(z) \cos(\theta(z) - \psi). \end{aligned} \quad (4.9)$$

Concerning the segregation effects the value of a matters. According to Ref. [160] the value of $\gamma = 240$ implies $c \approx 0.035$ and therefore $a \approx 10 \times k_B T / (m^2 \rho_{\text{iso}}) \approx 3.1 \times 10^{-4} \text{ N/A}^2$ (concerning the definition of a in terms of c see Ref. [160]). Since the sample always contains a fixed number of magnetic colloids (i.e., neglecting aggregation) the field $\tau(z)$ is subject to the constraint (see Appendix C)

$$\frac{1}{D} \int_0^D dz \tau(z) = 1. \quad (4.10)$$

It is convenient to consider deviations $\delta\tau(z)$ from the homogeneous case, i.e.,

$$\tau(z) = 1 + \delta\tau(z), \quad (4.11)$$

which allows one to rewrite the free energy density in Eq. (4.9) as the sum of the free energy density evaluated for $\tau(z) = \text{const} = 1$ and the contribution due to segregation:

$$\begin{aligned} \beta f(\theta(z), \varphi(z), \tau(z)) = & \\ & \beta f(\theta(z), \varphi(z), \tau(z) = 1) + \beta f_{\text{seg}}(\theta(z), \varphi(z), \tau(z)), \end{aligned} \quad (4.12)$$

where $f_{\text{seg}}(\theta(z), \varphi(z), \tau(z))$ is defined as

$$\begin{aligned} \beta f_{\text{seg}}(\theta(z), \varphi(z), \tau(z)) := & \\ & \beta(m\rho_{\text{iso}})^2 \left(a - \gamma \mu_0 \cos(\theta(z) - \varphi(z)) \right)^2 \\ & - \beta m \rho_{\text{iso}} B \cos(\theta(z) - \psi) \delta\tau(z) \\ & + \beta(m\rho_{\text{iso}})^2 \left(\frac{a}{2} - \frac{1}{2} \gamma \mu_0 \cos(\theta(z) - \varphi(z)) \right)^2 \delta\tau(z)^2. \end{aligned} \quad (4.13)$$

The constraint in Eq. (4.10) turns into

$$\int_0^D dz \delta\tau(z) = 0. \quad (4.14)$$

We express $\delta\tau(z)$ in terms of a Fourier series:

$$\delta\tau(z) = \frac{a_0}{2} + \sum_{n=1}^{\infty} \left[a_n \cos\left(\frac{2\pi n z}{D}\right) + b_n \sin\left(\frac{2\pi n z}{D}\right) \right]. \quad (4.15)$$

Equation (4.14) implies $a_0 = 0$. The functional in Eq. (4.2) is minimized with respect to the fields $\theta(z)$ and $\varphi(z)$ and the coefficients a_n and b_n , $n \in \{1, 2, \dots, N\}$. The number

of coefficients N to be taken into account has to be chosen. It is reasonable to set the minimum wavelength in the Fourier series to be larger than the colloid diameter $d \sim 100$ nm. Therefore, N has to be smaller than $N_{\max} = [D/d]$ where $[x]$ denotes the integer part of x . For a slab of thickness $D = 20 \mu\text{m}$ one has $N_{\max} = 200$.

It turned out that for slab thicknesses $D < 60 \mu\text{m}$ the equilibrium profile $\tau(z)$ obtained from Eq. (4.9) takes negative values, i.e., $\delta\tau(z) < -1$, which contradicts its physical meaning $\tau(z) \sim |\mathbf{M}(z)| \geq 0$. This behavior is related to the absence of contributions in $\tau(z)$ beyond quadratic order. However, for slab thicknesses $D \geq 60 \mu\text{m}$ the algorithm does provide the profiles $\theta(z)$ and $\varphi(z)$ together with a physically reasonable segregation profile $\delta\tau(z)$. Figure 4.12 shows the calculated profiles for $D = 120 \mu\text{m}$, equal walls with strong anchoring $W_{\text{wall}} = 3.4 \times 10^{-5} \text{ J/m}^2$, coupling constant $\gamma = 240$, and external magnetic field $B = 4 \text{ mT}$. It is evident that switching mechanism I is observed even in the presence of segregation effects. The density of magnetic colloids is largely reduced (with $\delta\tau(z)$ close to -1) in the regions of nonzero gradient of the director profile. An important difference to the case of infinitely strong coupling of the colloids to the liquid crystal (see Ref. [85]) is the *depletion layer* being shifted away from the walls towards the interior of the sample. The functional form of the profiles $\varphi(z)$ and $\theta(z)$ obtained for asymmetric pairs of walls with strong and weak anchoring (see Fig. 4.9 in Sec. 4.3.3) is found at both walls for sufficiently thick slabs. We have performed a series of calculations for different slab thicknesses D in order to determine for which thickness the pure switching mechanism I turns into a combination of mechanisms I and II (see Fig. 4.12); we have found $D = 95 \pm 5 \mu\text{m}$. This observation opens the possibility to manipulate the sample magnetization in a manner similar to that described in Sec. 4.3.3 but without the need to use a second, weakly anchored wall. However, the state of nonzero net magnetization is not necessarily saturated, but it might exhibit $\mathcal{M} < 1$. In order to have nonetheless a state with the magnetization $\mathcal{M} \approx 1$, one would need to adjust the system parameters (e.g., wall anchoring, elastic constant of the NLC etc.) such that each region of switched magnetization in the vicinity of the walls (see Fig. 4.12) takes up $\approx 25\%$ of the slab thickness.

We have also performed a calculation for the case of two walls with equally weak anchoring. We found that segregation did not have a qualitative impact in that case either. Therefore we expect that the results of Secs. 4.3.1 and 4.3.2 are not affected qualitatively by segregation.

4.5 Summary and conclusions

In this analysis we have studied theoretically a ferronematic confined between two planar, parallel walls which impose an easy axis on the NLC director field. Inspired by the

experimental studies reported in Refs. [102, 148], the system is subjected to an external magnetic field. The ferronematic is an anisotropic polar fluid and thus the system is characterized by the relative directions of the NLC director, the easy axes due to the walls, the magnetization, and the external magnetic field. We have considered the situation in which the ferronematic is initially prepared with a uniform magnetization along the easy axis of the NLC. Subsequently an external magnetic field is applied in the direction opposite to the magnetization. This choice of the geometry reduces the theoretical description to an effectively one-dimensional one. The experiments reported in Refs. [102, 148] showed that for such a setup there exists a critical external magnetic field $B_{\text{cr}} > 0$ such that for magnetic field strengths $|\mathbf{B}| < B_{\text{cr}}$ the sample remains unperturbed. The authors of Ref. [102] also provided the expression in Eq. (4.7) for the critical magnetic field strength in terms of the coupling γ between the magnetization and the nematic director field. This critical magnetic field strength, which increases upon increasing γ , has been determined as that magnetic field strength for which the relaxation rate of long-wavelength fluctuations of the nematic director field vanish.

Here we study the system by numerical minimization of the corresponding free energy functional in Eq. (4.2). The numerical minimization is performed by using the Fletcher-Reeves-Polak-Ribiere general function minimization algorithm. It is obvious, that the global minimum of the free energy functional in Eq. (4.2) before the external magnetic field has been applied is the initial state of the ferronematic being uniformly magnetized along the easy axis. Once the magnetic field is applied in the direction opposite to the initial magnetization, this state becomes only a local (metastable) minimum. The new global minimum is the ferronematic magnetized in the direction of the field. By means of a conjugate gradient algorithm one is able to search for the local minimum of the free energy and therefore to identify metastable states of the system. This is particularly useful in the present context, because this way one can investigate possible intermediate orientation profiles between the initial, now metastable, state with a uniform magnetization in the positive x -direction, i.e., opposite to the magnetic field $\mathbf{B} = B\mathbf{e}_x$ pointing into the negative x -direction, i.e., $B < 0$, and the final stable state with the magnetization in the direction along the magnetic field, i.e., in negative x -direction ($B < 0$).

Figure 4.2 shows the dependence of the dimensionless magnetization \mathcal{M} (Eq. (4.6)) of the metastable state described above on the strength of the external magnetic field for particular values of the coupling constant γ and of the anchoring strength W_{wall} at a wall. One observes hysteresis of the magnetization for which a critical magnetic field strength B_{cr} can be identified as the one for which significant deviations from the saturation magnetization $\mathcal{M} = 1$ occur. One can distinguish several, qualitatively different, intermediate states (red circles in Fig. 4.2). First, for a magnetic field $\mathbf{B} = B\mathbf{e}_x$, with component B in the direction of the initial magnetization ($B > 0$), the sample remains practically

unperturbed for $B > B_{\text{cr}}$ ($B_{\text{cr}} < 0$), i.e., for the magnetic field either along the initial magnetization ($B > 0$) or sufficiently weak in the direction opposite to the initial magnetization ($B < 0$) (see Fig. 4.3(1)). Upon decreasing the component B of the magnetic field $\mathbf{B} = B\mathbf{e}_x$ further (i.e., making it less positive or more negative), the torque imposed on the NLC by the walls is no longer able to keep the ferronematic in the initial unperturbed state and thus the profiles become perturbed (see Fig. 4.3(2)). These states correspond to the brightening of the sample when viewed via crossed polarizers [102]. If one decreases the magnetic field component B even further (i.e., making B even more negative), one encounters the interesting metastable state shown in Fig. 4.3(3). In this state, near each wall a layer is formed within which the nematic director is close to the easy axis and the magnetization has inverted its direction, pointing along the external magnetic field (i.e., in negative x -direction). This flipping of the magnetization is energetically favorable for a sufficiently large strength $|\mathbf{B}| = |B|$ of the magnetic field pointing in the direction opposite to the initial magnetization (i.e., pointing into the negative x -direction), because the contribution to the free energy (Eq. (4.1)) of the coupling between the magnetization and the nematic director is invariant upon inversion of the magnetization, $\mathbf{M} \mapsto -\mathbf{M}$, but the contribution of the coupling between the magnetization and the external magnetic field is not. When the external magnetic field becomes even stronger (i.e., B becomes even more negative and $|B|$ even larger), the regions of flipped magnetization expand into the interior of the system, eventually giving rise to the whole sample (except for thin layers in the very vicinity of the walls) being magnetized along the magnetic field. The qualitatively different scenario, which we refer to as switching mechanism II, occurs if the wall anchoring W_{wall} is too weak to prevent the nematic director field from following the rotating magnetization. In accordance to Figs. 4.3(3) and 4.3(4), in this scenario the final stages of the switching are not realized. Figure 4.7 illustrates how the final stages (3) and (4) of the switching mechanism II are realized, according to which the magnetization *and* the director field rotate in parallel.

Figure 4.8 shows whether certain combinations of wall anchoring strengths $W_{\text{wall}}^{(1)} = W_{\text{wall}}^{(2)} = W_{\text{wall}}$ as well as of the coupling constant γ lead to switching mechanism I or II. According to the map in Fig. 4.8 the switching mechanism I is the dominant one in the experiments described in Refs. [102, 148] ($W_{\text{wall}}^{\text{exp}} \approx 3.4 \times 10^{-5} \text{ J/m}^2$). It has to be noted that actual wall surfaces are not ideal and therefore the anchoring strength may vary across the surface. Hence, it is possible that the anchoring can be weak (or strong) in the vicinity of isolated imperfections while far away from them the anchoring is strong (or weak). Moreover, one can consider the situation that two neighboring regions of the wall surface, one of which exhibits strong anchoring and the other one weak anchoring, can cause the nucleation of surface defects of the liquid crystal if an external magnetic field is applied. Indeed, upon switching on an external magnetic field, the nematic director close to regions

with strong anchoring does not switch its direction whereas the director close to regions with weak anchoring rotates in order to follow the direction of the magnetization. Thus, a mismatch of the director orientation will occur at the boundary separating the two regions of the wall surface. Such a surface defect was observed in the experiment (see Ref. [102]) which might indicate the role of imperfections of the wall (such as inhomogeneities of the coating, the use of spacers, etc.). The numerical method used here can, in principle, be utilized in order to investigate such a situation. However, this would require to consider a fully three-dimensional setup, thereby increasing the numerical complexity significantly.

The dependences of the critical magnetic field strength B_{cr} on the coupling constant γ and on the (equal) wall anchoring strength W_{wall} are presented in Figs. 4.5 and 4.6. On one hand, B_{cr} increases as function of W_{wall} and, on the other hand, it also increases as function of γ , which is consistent with the results of Ref. [102]. In Fig. 4.6(b) a comparison of the critical magnetic field strength B_{cr} as defined here with that introduced in Ref. [102] (see Eq. (4.7)) shows good agreement, although the two expressions involve different properties of the ferronematic.

Within a recently developed theory of ferronematics [160] one can relate the coupling coefficient γ to the microscopic coupling c (see below Eq. (4.1)) which depends on the size of the colloids in the suspension. Figure 4.6(c) shows the dependence of B_{cr} on the microscopic coupling c for a particular value of the wall anchoring strength W_{wall} . This allows one to vary the critical magnetic field by tuning the mean value of the size distribution of the colloids participating in the ferronematic.

Combining two walls with different anchoring strengths allows one to design a sample such that its switching mechanism is a superposition of type I and type II. The resulting nematic director and magnetization field profiles (see Figs. 4.9 and 4.10) are obtained by applying an external magnetic field. In turn, switching off this field divides the sample into two domains with opposite magnetizations (see Fig. 4.11 (c)), rendering a sample with zero net magnetization. The initial state (i.e., the magnetized slab) can be restored by applying an external magnetic field of suitable direction to the two-domain sample. This cycle can be repeated arbitrarily, thus facilitating the switching between two states (magnetized/demagnetized slab) by using a uniform magnetic field only. This opens application perspectives such as storage of information and magnetic fields detection.

Similar controllable magnetic slabs can be constructed by using two walls with equally strong anchoring for samples of larger thickness ($D \geq 95 \mu\text{m}$ for $\gamma = 240$, $K = 3.5 \times 10^{-12}$ N, and $W_{\text{wall}} = 3.4 \times 10^{-5}$ J/m²). We have found segregation to be *quantitatively* different from the case of walls with infinitely strong anchoring and of infinitely strong coupling of the colloids to the NLC (see Ref. [85]). However, segregation effects do not affect the switching mechanisms qualitatively.

Chapter 5

Conclusions and outlook

In the present work we carried out a theoretical study of ferronematics, i.e., dilute colloidal suspensions of anisotropic magnetic colloids in nematic liquid crystals. The mesoscopic free energy density of ferronematics has been derived from a microscopic liquid state theory (see Chap. 3). Then this free energy density has been applied to the particular geometry of a ferronematic contained in between two planar and parallel walls.

A ferronematic is an example of a complex fluid. It has two distinct components: the nematic liquid crystal as a host and magnetic particles as colloidal inclusions. Both components possess anisotropic properties. The analytical description of this system on the level of individual particles of the smaller species (i.e., the liquid crystal molecules) is practically impossible. Therefore an effective theory is established in the present study within which the NLC is treated as a continuous anisotropic medium and characterized by the spatially varying director field $\mathbf{n}(\mathbf{r})$. We assumed homeotropic anchoring of the liquid crystal to the surface of the colloidal particle, i.e., the director $\mathbf{n}(\mathbf{s})$ at point \mathbf{s} of the surface of the colloid prefers to point along the normal to the surface at point \mathbf{s} . However, the anchoring was assumed to be “soft”, i.e., deviations of $\mathbf{n}(\mathbf{s})$ from the preferred direction were not forbidden, albeit they would cause an energy penalty.

A colloid was modelled as a very thin disc that carries a point magnetic dipole $m\boldsymbol{\omega}$ in its center (see Fig. 3.1). The magnetic moment was taken to be parallel to the normal to the surface of the disc. Once immersed into a homogeneous nematic, such a disc-like colloid adopts a certain equilibrium *orientation* due to the homeotropic anchoring on its surface. In the particular case considered in this study the equilibrium orientation corresponds to the uniform nematic director $\mathbf{n}_0 = \text{const}$ and the colloid that is oriented such that its surface is perpendicular to \mathbf{n}_0 . A change in equilibrium orientation of the colloidal disc would correspond to a change of the boundary conditions from the standpoint of the NLC and therefore an orientational free energy that corresponds to the change in the energy of the colloid-NLC system with respect to the equilibrium configuration has to be inferred. This one-particle potential has been derived in Sec. 3.2.2. The corresponding expression is

a power series in terms of a microscopic coupling constant c (see Sec. 3.2.2 for definition). The range of c where the derived orientational free energy is valid has been numerically assessed (see Sec. 3.3.1). The value of c that corresponds to the experimental parameters reported in Refs. [102, 148] is below the threshold value and thus the expression for the orientational free energy can be used.

We found evidence that the orientational free energy can be expressed as a series $\sum_{n=1}^{\infty} y_n(c)(\mathbf{n}_0 \cdot \boldsymbol{\omega})^{2n}$, where the coefficients $y_n(c)$ are polynomials of degree n in terms of the microscopic coupling c . For small values of c only the lowest orders n should be considered (we considered orders up to $n = 2$ in the present study). It is not possible to find the coefficients y_n for $n > 2$ analytically, however they can, in principle, be inferred numerically as functions of c using, e.g., an approach described in the present work, i.e., a finite element method that minimizes the free energy of the disc-like colloid in the center of a cubic cell filled with an NLC.

Since it is sufficient to keep only terms up to $n = 2$ (see Sec. 3.3.1) to describe the colloidal system of the experiments reported in Refs. [102, 148] we can use the obtained *analytical* expression for the orientational free energy as a one-body potential or *external potential* in the density functional (see Sec. 2.1) of the colloids. The functional corresponds to that of an ideal gas since particle interactions were disregarded. Neglecting pair interactions is well justified in the case of van der Waals, magnetic dipole-dipole, and steric hard core interactions due to the high dilution of the colloids. On the other hand, neglection of the *effective elastic interaction* (see Sec. 1.2.3) is less justified due to its long range Coulomb-like nature. Note, however, that it is proportional to the product of the torques that act on each colloid (see Sec. 1.2.3) and in the case of very thin colloids these torques can be calculated through the derivative $dF(\theta)/d\theta$, where $F(\theta)$ is the orientational free energy of a single colloid (see Sec. 3.2.2) with $\theta = \arccos(\mathbf{n}_0 \cdot \boldsymbol{\omega})$, and thus the corresponding effective elastic pair interaction is proportional to c^2 that is small when c is small.

The density functional of the magnetic colloids, depends on the density profile $\rho(\mathbf{r}, \boldsymbol{\omega})$ and the director profile $\mathbf{n}(\mathbf{r})$ (through the external potential term) while the phenomenological free energy of the ferronematic (see Eq. (1.33)) is a functional of the magnetization $\mathbf{M}(\mathbf{r})$ and the nematic director $\mathbf{n}(\mathbf{r})$. We derived the function of the required variables, i.e., $\mathbf{M}(\mathbf{r})$ and $\mathbf{n}(\mathbf{r})$, by minimizing the density functional *under the constraint* that a prescribed magnetization field $\mathbf{M}(\mathbf{r})$ is realized (see Sec. 3.2.3). The corresponding constrained minimization yields an Euler-Lagrange equation that includes an unknown Lagrange multiplier. We were able to express this Lagrange multiplier in terms of $\mathbf{M}(\mathbf{r})$ and $\mathbf{n}(\mathbf{r})$ through the approximation of the corresponding generating function Z (see Sec. 3.2.3) by a power series in powers of the absolute value of the Lagrange multiplier. We cut this infinite series after the quadratic order based on the argument that the sam-

ple cannot have an arbitrarily large magnetization $\mathbf{M}(\mathbf{r})$ due to only a finite number of colloids used in the experiments. That seems to introduce only a small error into the description. The final expression for the free energy density is similar to the phenomenological one proposed by Mertelj et. al. (see Ref. [102] and Eq. (1.33)). The contribution proportional to $|\mathbf{M}|^4$ is absent in the expression derived in the present study but this is without consequences since the coefficient in front of the contribution proportional to $|\mathbf{M}|^2$ is positive. The coupling between the magnetization field and the director field proportional to $(\mathbf{M}(\mathbf{r}) \cdot \mathbf{n}(\mathbf{r}))^2$ is present in the theory and the corresponding prefactor is calculated. Thus, the coupling constant γ of the phenomenological approach was identified and its dependence on the microscopic coupling c was therefore established. The value of γ inferred from our results roughly coincides with the one inferred from the fitting of experimental data reported in Refs. [102, 148]. The discrepancy is due to the simplifications adopted in the present study (monodispersity of colloids, neglect of the effective elastic interaction) as well as due to the assumptions made in the theory used in Refs. [102, 148] to fit the experimental data (monodispersity of colloids, simplified form of the coupling of the NLC to the magnetization field).

Comparing the Landau-like effective free energy density obtained in the present study to the free energy density of Burylov and Raikher (see Sec. 1.2.4 and Eq. (1.31)) one can point out the following differences. The Burylov-Raikher theory explicitly includes the volume fraction of the colloids as a spatially varying field whereas the effective Landau theory includes the volume fraction implicitly through the absolute value of the magnetization field $|\mathbf{M}|$. Furthermore, the Burylov-Raikher theory contains a term that is proportional to the logarithm of the volume fraction and the effective Landau theory contains terms that are proportional to the powers of the volume fraction (i.e., of $|\mathbf{M}|$). A consequence of this fact is that the Burylov-Raikher theory is defined only in the physically reasonable domain of positive volume fractions whereas the effective Landau theory formally allows negative values. Therefore additional care should be taken when the effective Landau free energy density is minimized and the volume fraction is allowed to vary. A logarithmic term is present in the density functional of the colloids (see Sec. 3.2.3) which suggests that the effective Landau theory represents a next level of coarse-graining compared to the Burylov-Raikher theory.

A challenging but interesting way to extend the approach used in this study is to include the effective elastic interactions. Although the corresponding potential is proportional to the small quantity c^2 (see above) it may have quantitative consequences for $c > 0.1$. The term proportional to c^2 in the one-particle elastic potential derived in Sec. 3.2.2 was shown to not have an impact on the coupling constant γ for $c < 0.04$. As c is increased (which, for instance, would correspond to increasing the size of the colloids) the higher order term (i.e., $\propto c^2$) will influence the value of γ . When the value of c is

increased beyond 0.5 the microscopic distortions of the NLC around each individual particle would extend further away from the particle such that two distortion “clouds” from two different particles will have a significant overlap even for dilute solutions. It would be interesting to see if it is possible to incorporate this effect into the expression for γ . We may also speculate that the inclusion of the effective pair potential may result in the appearance of the non-local terms of the kind $\propto (\mathbf{M}(\mathbf{r}) \cdot \mathbf{M}(\mathbf{r}'))$ in the effective free energy.

In Chap. 4 we investigated a particular geometry, i.e., a ferronematic between two parallel and planar walls. This geometry is used in all the experimental realizations of ferronematics to date. Despite its simplicity a rich behavior can be observed due to the complexity of the fluid itself. We considered the situation in which the ferronematic is placed between the walls that impose a non-degenerate easy direction. Moreover, the ferronematic is assumed to be prepared in the presence of a weak bias magnetic field such that after the quench of the liquid into the nematic phase all individual colloids align their magnetic moments in the same direction yielding a uniformly magnetized monodomain sample (also after the bias field is switched off). Note that an alternative initial condition is possible in which the external bias field is *not* applied and the sample exhibits a polydomain structure with two kinds of domains within which magnetization points in two opposite directions (for details see Ref. [102]). Such an initial condition was not considered in the present study.

We assumed that both confining walls interact with the NLC, i.e., impose an easy axis along which the nematic director prefers to align. The *direction* of the easy axis was kept the same for both walls at all times and was chosen to be in the lateral direction. However the *anchoring strength* could be either the same for both walls or it could have a distinct value on each wall. The symmetry of the problem implies that the physical quantities change only in the transverse direction, i.e., in the direction perpendicular to the slab.

The appropriate energy functional has been constructed. The contribution due to the ferronematic is described by the free energy density derived in Chap. 3. The *macroscopic* distortions of the liquid crystal are taken into account in the form of the usual Oseen-Zöcher-Frank elastic energy functional that takes a particularly simple form (see Eq. (4.4)) when the nematic director can be described by a single angle, i.e., by a *scalar* spatially varying field. Finally, the interaction of the NLC with the walls is described by the Rapini-Papoular potential (see Eqs. (1.28) and (4.4)).

It is worth mentioning that since a one-elastic-constant approximation is used throughout the current study it is reasonable to consider the NLC distortions according to Fig. 4.1. In the actual experiment (see Refs. [102, 148]) the relevant distortion mode is the twist deformation because the corresponding elastic constant is smaller compared to elastic constants of the bend and the splay deformation. In the context of Fig. 4.1 it would mean that the director field rotates *in the plane* of the slab (i.e., in the xy -plane) and not

in the xz -plane. It is obvious that the mathematical formulation of the problem is left unaffected (within the one-elastic-constant approximation) up to an interpretation of the angle $\phi(z)$ (see Fig. 4.1) as the angle of twist instead of the angle of bend.

The choice of the direction of the external magnetic field relative to the direction of the initial uniform magnetization has a direct impact on the behavior of the system. The situation in which the magnetic field is applied *perpendicular* to the initial magnetization has been extensively studied in the literature. A *thresholdless* distortion of the NLC has been observed in this case. This study, on the other hand, considers the situation in which the magnetic field is applied in the direction *antiparallel* to the direction of the initial magnetization. The same setup was considered experimentally by Mertelj et al. (see Ref. [102]). It was found in the experiment that the NLC is not distorted until a certain *threshold* magnitude of the magnetic field (called the “critical field” B_{cr}) is used which is analogous to the usual ferromagnets. It was argued by the authors of Ref. [102] that the existence of the critical field can be explained in terms of the diverging relaxation time of the fundamental thermal fluctuations of the nematic director.

First, we considered the simpler case in which the anchoring strength at both walls was the same. We have obtained the dependence of the projection of the magnetization on the direction of the external magnetic field during sample preparation numerically. The obtained curves are hysteresis loops and therefore confirm the experimental findings. The hysteresis curves obtained in the present study feature a critical magnetic field $B_{\text{cr}} > 0$. We observed that upon applying an external magnetic field $\mathbf{B} = B\mathbf{e}_x$ with $B < 0$ to the sample that is magnetized along the positive x -direction the ferronematic does not exhibit a macroscopic distortion of the NLC director until a certain critical value of the external field amplitude is reached, i.e., for $B \in [-B_{\text{cr}}, 0]$. Once $B < -B_{\text{cr}}$ the NLC director is distorted due to its coupling to the magnetization field (see the term proportional to $[\mathbf{M}(\mathbf{r}) \cdot \mathbf{n}(\mathbf{r})]^2$ in the effective Landau free energy density in Eq. (3.36)). Our approach allows us to vary the parameters of the model. We focused on the dependence of the results on the anchoring strength at the walls and the coupling constant γ . We studied the dependence of the critical field on these two parameters (see Fig. 4.5). We found that the value of the critical field increases upon increasing the anchoring strength W_{wall} at the walls and plateaus for larger values ($W_{\text{wall}} \approx 10 \times 10^{-5} \text{ J/m}^2$). The latter finding inspired the comparison to the expression of the critical field derived in Ref. [102] for the case of infinite anchoring strength (see Eq. (4.7)). The comparison is shown in Fig. 4.6(b) as a function of the coupling constant γ . Remarkably, the expression in Eq. (4.7) perfectly describes the results obtained numerically in the present study for $W_{\text{wall}} = 4 \times 10^{-5} \text{ J/m}^2$ although the value of the anchoring used is finite and there is no dynamics included and therefore the explanation of the nature of the critical field due to the diverging relaxation time of the director field fluctuations cannot be applied.

The connection between the coupling constant γ and the microscopic coupling constant c that has been established in Chap. 3 can be used to plot B_{cr} as a function of c . The dependence $B_{\text{cr}}(c)$ is useful because it allows one to tune the value of the critical field by tuning the mean size of the colloids used (recall the definition of c in Eq. (3.4)).

The numerical algorithm used in the present study (see Sec. 2.2) allowed us to obtain the intermediate metastable states that the system passes through before it reaches the stable equilibrium. In the considered setup the stable equilibrium corresponds to the slab that is uniformly magnetized along the negative x -direction (given that the initial magnetization points along the positive x -direction and the external magnetic field is applied in the negative x -direction). We found that the system can follow two qualitatively distinct paths before reaching the common equilibrium configuration. In the first scenario, or *switching mechanism*, the magnetization field forms layers near the walls in which its direction flips to that along the field, however, the director field is kept from rotating along with the magnetization by the anchoring to the walls. These regions of the flipped magnetization direction grow towards the interior of the slab as the magnitude of the external field is gradually increased. Eventually, the magnetization through the entire slab is rotated along the field and thus the equilibrium is reached.

In the second switching mechanism which corresponds to the weak anchoring of the NLC to the walls, the director field follows the magnetization and makes a 180° turn. We calculated the map (see Fig. 4.8) that shows which switching mechanism dominates for given values of γ and W_{wall} . The second switching mechanism is found to dominate only for anchoring strengths at the walls of less than about $\sim 0.2 \times 10^{-5}$ J/m² and therefore we expect the first switching mechanism to dominate in the experiment reported in Ref. [102] (the estimated wall anchoring is $W_{\text{wall}}^{\text{exp}} = 3.4 \times 10^{-5}$ J/m²).

As a natural extension of the problem we considered the situation in which walls have different values of the anchoring strength W_{wall} assigned to them, i.e., the wall at $z = 0$ is characterized by the anchoring strength $W_{\text{wall}}^{(1)}$ and the wall at $z = D$ (where D is the width of the slab) is characterized by the anchoring strength $W_{\text{wall}}^{(2)}$. We found a triple $(\gamma, W_{\text{wall}}^{(1)}, W_{\text{wall}}^{(2)})$ that produces a switching mechanism that is a superposition of the first and the second switching mechanisms (see Sec. 4.3.3). This means that the layer of the switched magnetization is created near the wall with the strong anchoring (in the sense that it corresponds to the first switching mechanism) whereas the nematic director rotates along with the magnetization in the vicinity of the wall with the weak anchoring (in the sense that it corresponds to the second switching mechanism). The resulting profile features a smooth distortion of the nematic director (see Fig. 4.9) and does not change significantly if the field is increased further. If now, the external field is suddenly switched off (corresponds to the conjugate gradient minimization with $B = 0$ and the profiles in Fig. 4.9 as the initial condition) the elastic distortion of the NLC relaxes and the magne-

tization in the vicinity of the wall with the weak anchoring follows the director rotation. This relaxation yields a slab with one part being magnetized along the positive x -direction and another part being magnetized along the negative x -direction (see Fig. 4.11(c)). Obviously, the integrated x -component of the magnetization of such a slab is significantly less than that of a slab that is uniformly magnetized. The experimental realization of such a system would be very interesting. If, moreover, one manages to adjust the parameters of the experimental system such that each part of the *two-domain* slab takes roughly 50% of the slab thickness the integrated x -component of the magnetization will be close to zero. Remarkably, if an external magnetic field in the *positive x -direction* is applied to the two-domain sample the system is brought back into the uniformly magnetized, monodomain state (see Fig. 4.11(d)). Therefore, one can cycle through the three states just described (see Figs. 4.11(a), 4.11(b), and 4.11(c)) by applying an external magnetic field in the suitable directions. The described quantitative idea can be utilized in, for instance, a memory device. A unit of information in such a device (i.e., a “bit”) can be assigned to the projection of the magnetization of the slab. One could assign a logical value “0” to the state with small magnetization of the slab (see Fig. 4.11(c)) and a logical value “1” to the state with large magnetization of the slab (see Fig. 4.11(a)) or vice versa. The array of such cells would code binary information. The change of the information content of the cell would be done by applying an external magnetic field of the suitable orientation to the cell. Another hypothetical possibility for an application is that of a spatially resolving small magnetic field detector composed of an array of such cells.

In the analysis of the behavior of the ferronematic slab summarized above we have neglected *segregation* of the colloids. This effect amounts to the redistribution of the colloids in the slab in order to minimize their magnetic energy. Indeed, if the colloidal particle prefers to rotate in order to align its magnetic moment along the external magnetic field it may find it difficult due to the nematic director in its vicinity. If, however, there is a region in which the director field is such that it is compatible with the rotation of the colloid, the particle can be forced to migrate into that region. A collection of particles can therefore create an *inhomogeneity* in the density profile. The negative energy gain due to the alignment of the magnetic moment along the magnetic field can negate the positive entropic energy penalty due to the inhomogeneity. The possibility for such a non-homogeneous spatial distribution of the colloids corresponds to having a non-constant *absolute value* of the magnetization vector $|\mathbf{M}(\mathbf{r})|$. We performed numerical minimizations with the segregation effects taken into account. Unfortunately, the algorithm returned unphysical results (i.e., $|\mathbf{M}(\mathbf{r})| < 0$) for slab thicknesses $D < 60 \mu\text{m}$. We attribute this unphysical behavior to the lack of terms $|\mathbf{M}(\mathbf{r})|^n$, $n > 2$, in the effective free energy density (see Chap. 3). For slabs thicker than $60 \mu\text{m}$ the algorithm returns physically reasonable profiles. We found that the segregation does not influence the two switching mechanisms

qualitatively. Moreover, for slab thicknesses $D > 95 \mu\text{m}$ and *equal* strong anchoring at *both* walls the algorithm yields a profile that is a combination of both switching mechanisms (see Fig. 4.12). We argue, that for sufficiently thick slabs the interior of the slab is sufficiently far away from both walls and the nematic director there is not influenced by the anchoring at the walls and thus can follow the magnetization rather easily. This way the interior of the slab switches according to the second switching mechanism even though the ferronematic in the vicinity of the walls may switch according to the first mechanism. This observation opens up the possibility to build a cell that can reversibly switch off its magnetization (see above) *without* the need to have two walls with different anchoring. In order to have a very small magnetization in one of the states, the regions in the vicinity of the walls that switch according to the first switching mechanism (see Fig. 4.12) have to take up $\approx 25\%$ of the slab thickness each. The segregation manifests itself in the significant reduction of the density of the colloids in the regions where the nematic director is nonuniform, i.e., in the regions where the gradient of the nematic director is large (see minima of the blue curve in Fig. 4.12). These regions of the reduced density of the colloidal particles are called *depletion layers*. Interestingly, the depletion layer in the case of the wall with the strong anchoring is *separated* from the wall. Compare this to the situation considered by Brochard and de Gennes [85], where the infinite anchoring to the wall was assumed and moreover an assumption of infinite anchoring of the nematic director to the surface of the colloids was used. The authors of Ref. [85] found the depletion layer in the *close vicinity* of the wall. The difference originates from the assumption of soft anchoring between the nematic director and the surface of the colloids used in the present work. Indeed, this allows the magnetization to flip and thus enables the first switching mechanism. Within the layers of the flipped magnetization the nematic director is able to adopt a close-to-uniform configuration (see Fig. 4.12) and therefore the gradient of the director is shifted towards the interior of the slab. As a result, colloids are expelled from the layers that are separated from the wall. It would be very interesting to observe the described combination of the switching mechanisms and the depletion layers by optical means in the experiment.

A possible extension of the present numerical analysis would be to consider a *poly-domain* sample as an initial condition. It means that the magnetization vector can vary not only along the transverse direction Oz but also in the lateral xy -plane. This makes all quantities functions of the three-dimensional spatial coordinate $\mathbf{r} \in \mathbb{R}^3$ and therefore significantly complicates the numerical treatment. On the other hand a very rich behavior can be expected if one considers walls with equal anchoring and a thin slab (the situation reported in the experiment in Ref. [102]), walls with different anchoring, or thicker slabs.

Chapter 6

Summary

In the present thesis we were concerned with a particular type of a soft matter system — a ferronematic, i.e., a colloidal suspension of magnetic anisotropic particles in a nematic liquid crystal. This two-component complex fluid exhibits anisotropic properties which are due to both the dispersion medium (i.e., an NLC) and the dispersed phase (i.e., anisotropic colloidal particles). A *microscopic* theory of such sophisticated system derived within the statistical mechanics formalism that would describe *macroscopic* behavior (i.e., for example, the response to external fields) is a demanding if not impossible task. An alternative approach to formulating a theoretical model of ferronematics is to consider an *effective* description instead. This amounts to obtaining an expression for the free energy of the system after some degree of coarse-graining was performed. Examples of such effective descriptions have been proposed before in the form of the Burylov-Raikher theory (see Ref. [90] and Eq. (1.31)) and the phenomenological effective theory due to Mertelj et al. (see Ref. [102] and Eq. (1.33)). The former, however, did not consider the proper connection between the volume fraction of the magnetic inclusions and the local magnetization field (notice that the last term in Eq. (1.33) includes the second power of the local magnetization direction and only the first power of the volume fraction). The latter, on the other hand, contained unknown expansion coefficients (see coefficients a and b in Eq. (1.33)) and a phenomenological coupling constant γ . Thus, neither theory offered a consistent and rigorous link between the *microscopic* parameters of the fluid (i.e., the elastic constant, the anchoring strength of the NLC to the surface of the colloid, the size of the colloid, and the magnitude of the magnetic moment of the colloid) and the corresponding parameters (e.g., the coupling constant γ in Eq. (1.33)) in the effective free energy that governs the *macroscopic* behavior. The present work establishes this missing link.

In Chap. 3 we derive an expression similar to that in Eq. (1.33) starting from a microscopic fluid theory. The fluid is viewed as a collection of non-interacting magnetic discs. The NLC was taken into account as a continuous dispersion medium that interacts

with the colloids and is described by the nematic director $\mathbf{n}(\mathbf{r})$. Each colloid is coupled to the nematic environment through the *anchoring* of the NLC molecules at the colloidal surface. We considered the case of homeotropic anchoring, i.e., the nematic director prefers to point perpendicular to the surface of the colloid. This implies that the rotation of the colloid dispersed in the nematic induces distortions of the liquid crystalline material and therefore the existence of an effective elastic one-body potential. This potential was derived explicitly in Sec. 3.2.2 by considering the free energy of *microscopic* distortions. The validity of the derived one-body elastic potential was checked numerically and we found that it is valid as long as the microscopic coupling constant c (see Sec. 3.2.2 for definition) is sufficiently small (i.e., when $c < 0.1$ which is fulfilled for the parameters reported in Ref. [102]). The effective one body elastic potential was shown to be a power series in c . The first order contribution coincides with the earlier result (see Ref. [144]) for the case of long rod-like particles with planar anchoring due to the topological similarity of this case with the case of a very thin disc with the homeotropic anchoring. The second order term was derived using an analogy between the corresponding boundary problem and the electrostatic problem of finding the potential of a uniformly charged disc.

The effective one-body elastic potential has been interpreted as an external potential that acts on the orientational degrees of freedom of colloidal particles. The corresponding density functional was minimized under the constraint of a prescribed magnetization profile $\mathbf{M}(\mathbf{r})$. The resulting Euler-Lagrange equation contained a Lagrange multiplier which was not possible to eliminate in general. A quadratic approximation was adopted that allowed an elimination of the Lagrange multiplier in an analytical way. This approximation was shown to not introduce large errors in the description. As a result, a free energy density that depends on two spatially varying macroscopic fields, i.e, the magnetization field $\mathbf{M}(\mathbf{r})$ and the director field $\mathbf{n}(\mathbf{r})$, was derived. This expression contains terms proportional to $|\mathbf{M}(\mathbf{r})|^2$ and $(\mathbf{M}(\mathbf{r}) \cdot \mathbf{n}(\mathbf{r}))^2$ and thus can be directly compared to the expression due to Mertelj et al. (see Eq. (1.33)). The expressions for the coefficient a and the coupling constant γ in terms of microscopic parameters of the fluid were inferred. The absence of the term proportional to $|\mathbf{M}(\mathbf{r})|^4$ is without consequences because the coefficient of $|\mathbf{M}(\mathbf{r})|^2$ was shown to be positive. The explicit dependence of the coupling constant γ on the microscopic coupling constant c suggested that γ is not influenced by the inclusion of the terms $\propto c^n$, $n > 1$, for $c < 0.04$ in the effective one-body elastic potential and already a linear in c term is sufficient in this case.

In Chap. 4 we used the free energy density derived in Chap. 3 to investigate the behavior of a uniformly magnetized ferronematic placed between two parallel and planar walls. This setup is relevant in the context of the experiments in Refs. [102, 148] and represents a simple case of a confined ferronematic. We assumed that the walls are coupled to the NLC and impose an easy axis on the nematic director. The presence

of several relevant directions (i.e., the direction of the initial magnetization, the easy axis direction, and the direction of the external magnetic field) yields a rich variety of possible types of macroscopic response and therefore the behavior is strongly affected by the particular choice of the mutual orientations between these relevant directions. For instance, when the external magnetic field is applied *perpendicular* to the direction of the initial magnetization of the uniformly magnetized sample one observes a *thresholdless* distortion of the ferronematic (see Sec. 1.2.4 for the literature review). On the other hand, we were concerned with the case in which the external field is applied in the direction *antiparallel* to the direction of the initial magnetization. It was shown experimentally (see Ref. [102]) that in this case there exists a *critical* magnetic field B_{cr} , i.e., there is a *threshold* field before which the ferronematic remains unperturbed by the field. We obtained the corresponding critical field as a function of the coupling constant γ and the anchoring strength of the NLC to the walls W_{wall} numerically by minimizing the appropriate energy functional (see Eq. (4.2)). The obtained hysteresis loops (i.e., $\mathcal{M}(B)$, where \mathcal{M} is the dimensionless x -component of the sample's magnetization (see Fig. 4.1) and B is the magnitude of the magnetic field) are similar to those produced in the experiment. The calculated dependence $B_{\text{cr}}(\gamma, W_{\text{wall}})$ (see Fig. 4.5) showed that the critical field increases as γ or W_{wall} increase. However, the absolute value of the increase as a function of the anchoring strength W_{wall} is only of the order of 10^{-2} mT for $W_{\text{wall}} \geq 1 \times 10^{-5}$ J/m² and it seems to reach a plateau $B_{\text{cr}} = B_{\text{cr}}(\gamma)$ for large values of the wall anchoring (for $W_{\text{wall}} > 8 \times 10^{-5}$ J/m² provided $\gamma \approx 195$ (see Fig. 4.6(a))). The authors of Ref. [102] derived an expression for B_{cr} assuming that $W_{\text{wall}} = \infty$ (i.e., rigid anchoring of the NLC at the walls). We compared the result of our numerical approach to their expression for $W_{\text{wall}} = 4 \times 10^{-5}$ J/m² and plotted the comparison as a function of γ in Fig. 4.6(b). It is interesting that the results obtained by two completely different routes (numerical minimization of the free energy in the present work and the expression based on the argument that the relaxation time of the thermal fluctuations of the nematic director diverges at critical field) coincide almost perfectly even for *finite* value of the wall anchoring strength.

The dependence of the critical field on the coupling constant γ is important in the context of the experimental realization of the system. Indeed, using the results of Chap. 3, in particular, the connection between γ and the microscopic coupling constant c and, thus, particle size R , one can establish the dependence $B_{\text{cr}}(c)$ and therefore adjust the critical field by tuning the location of the maximum of the size distribution of colloids. An example of such a dependence for a particular value of $W_{\text{wall}} = 4 \times 10^{-5}$ J/m² is shown in Fig. 4.6(c).

The numerical algorithm implemented in the present study returns a local minimum of the free energy and thus is able to return metastable states of the system. The initial monodomain slab is the stable minimum when there is no external magnetic field applied.

Once the field in the direction antiparallel to the initial magnetization direction is applied the initial state becomes metastable and the global minimum corresponds to the uniform monodomain sample magnetized along the field. The states that correspond to each point of the hysteresis loop with $\mathcal{M} \neq \pm 1$ (see Fig. 4.2) can be viewed as a path that system follows before it adopts the equilibrium state. We found that if the anchoring strength W_{wall} at both walls is the same there are two possible paths that system can follow. Since the “path” connects two points in the state space that correspond to slabs that are uniformly magnetized in opposite directions we refer to each path as “switching mechanism”. We investigated which switching mechanism is realized as a function of W_{wall} and γ (see Fig. 4.8).

The first possibility, which we refer to as switching mechanism I, corresponds to larger wall anchoring strengths W_{wall} . The main distinct feature of this mechanism is the formation of layers near the walls in which the magnetization “flips” and orients in the direction along the field (see Fig. 4.3(c)). The nematic director, however, can not make a $\approx 180^\circ$ rotation because of the strong anchoring to the walls. As the external field increases these layers of the switched magnetization extend towards the interior of the slab until the magnetization through the entire slab is aligned along the external field.

The second possibility, which we refer to as switching mechanism II, corresponds to smaller values of the wall anchoring strength W_{wall} . Unlike the previous case, the layers of the flipped magnetization do not form when the switching mechanism II is realized. Instead, the magnetization field gradually rotates in order to align with the external field and is able to drag the nematic director along. The anchoring of the nematic to the walls is not strong enough to prevent the rotation of the director even in the close vicinity of the walls.

The regions of dominance of either switching mechanism as a function of W_{wall} and γ are shown in Fig. 4.8. It can be inferred that for the value of $\gamma \approx 200$ (roughly the value in the experiment reported in Ref. [102]) the switching mechanism II is realized only for very small anchoring strengths $W_{\text{wall}} \leq 0.2 \times 10^{-5} \text{ J/m}^2$, whereas the value of the anchoring estimated from the experiment ($W_{\text{wall}}^{\text{exp}} = 3.4 \times 10^{-5} \text{ J/m}^2$) is well above and therefore we conclude that the switching mechanism I is the one realized in the experiment.

An interesting question one can ask is what happens when walls with *different* anchoring strengths $W_{\text{wall}}^{(1)} \neq W_{\text{wall}}^{(2)}$ are combined in one system. This generalization does not increase the complexity of the problem from the numerical standpoint because it merely adds a nonhomogeneity of boundaries along the z -axis and thus the system remains effectively one-dimensional. We found a combination of $W_{\text{wall}}^{(1)}$, $W_{\text{wall}}^{(2)}$, and γ that produces an interesting result when exposed to the external magnetic field, i.e., the switching mechanism of such slab is neither I nor II but a *superposition* of both (see Fig. 4.9). Upon reaching a certain magnitude of the magnetic field the sample adopts a state in which

the magnetization is almost uniform and in the direction of the magnetic field while the nematic director is distorted (see Fig. 4.9). If we then suddenly switch off the field the sample exhibits two oppositely magnetized domains (see Fig. 4.11(c)). If the field is now applied again but in the *opposite* direction the sample is brought to the initial monodomain uniform state. Thus, one can, in principle, cycle between the monodomain and the two-domain states by applying the external magnetic field in suitable directions. This opens up a possibility of the hypothetical information storage device, made up of the collection of such ferronematic cells. Each cell would contain a binary bit of information coded in its magnetization, i.e., either $\mathcal{M} \approx 1$ (monodomain state) or $\mathcal{M} \ll 1$ (two-domain state).

The segregation effect (i.e., the spatial redistribution of the colloidal particles in magnetic field) was studied by allowing the absolute value of the magnetization $|\mathbf{M}|$ to vary with space, i.e., $|\mathbf{M}| = |\mathbf{M}(z)|$. The numerical algorithm returned unphysical results (i.e., $|\mathbf{M}| < 0$) for slabs thinner than $60 \mu\text{m}$. We explain this by the absence of higher order terms in $|\mathbf{M}|$ in the effective free energy of the ferronematic (see Chap. 3). The physically valid results were obtained for the slabs that are thicker than $60 \mu\text{m}$. The segregation was found to not influence the discussed switching mechanisms qualitatively. A formation of the depletion layer near the wall was found in the case of switching mechanism I. This layer, however, is separated from the wall unlike the case considered in Ref. [85] where the depletion layer is located directly near the wall. This effect is the consequence of the finite coupling of the nematic director and the magnetization field.

We found that for slabs thicker than $95 \mu\text{m}$ the combination of both switching mechanisms can be obtained even for two walls with *equal* and strong anchoring. This phenomenon becomes possible because for thicker slabs the interior regions of the slab are sufficiently far away from the strongly anchored walls and therefore can rotate along with the magnetization freely.

Chapter 7

Zusammenfassung

In der vorliegenden Dissertation haben wir uns mit einer bestimmten Art von weicher Materie beschäftigt — einer ferronematischen Substanz, d.h. eine kolloidale Suspension von anisotropen magnetischen Teilchen in einem nematischen Flüssigkristall (NLC). Dieses zwei-komponentige komplexe Fluid weist anisotrope Eigenschaften auf, die sowohl auf das Dispersionsmedium (ein NLC) als auch auf die dispergierte Phase (anisotrope kolloidale Teilchen) zurückzuführen sind. Eine *mikroskopische* Theorie eines solchen komplexen Systems, welche innerhalb des allgemeinen Formalismus der statistischen Mechanik abgeleitet wurde und das *makroskopische* Verhalten (z.B. die Reaktion auf externe Felder) beschreiben würde, ist eine anspruchsvolle, wenn nicht gar unmögliche Aufgabe. Ein alternativer Ansatz zur Formulierung eines theoretischen Modells der Ferronematen ist die Berücksichtigung einer *effektiven* Beschreibung. Dies bedeutet, dass ein Ausdruck für die freie Energie des Systems erhalten wird, nachdem ein gewisser Grad an Vergrößerung (coarse-graining) durchgeführt wurde. Beispiele für solche effektiven Beschreibungen wurden zuvor in Form der Burylov-Raikher-Theorie (siehe Ref. [90] und Gl. (1.31)) und der phänomenologischen Theorie von Mertelj et al. (siehe Ref. [102] und Gl. (1.33)) vorgeschlagen. Erstere berücksichtigte jedoch nicht den korrekten Zusammenhang zwischen dem Volumenanteil der magnetischen Einschlüsse und dem lokalen Magnetisierungsfeld (der letzte Term in Gl. (1.33) beinhaltet die zweite Potenz der lokalen Magnetisierungsrichtung und nur die erste Potenz des Volumenanteils). Letztere dagegen enthielt unbekannte Ausdehnungskoeffizienten (siehe die Koeffizienten a und b in Gl. (1.33)) und eine phänomenologische Kopplungskonstante γ . Somit bieten beide Theorien keine konsistente und rigorose Verbindung zwischen den mikroskopischen Parametern der Flüssigkeit (d.h. die elastische Konstante, die Stärke der Verankerung des NLC an der Oberfläche des Kolloids, die Größe des Kolloids und die Stärke des magnetischen Moments des Kolloids) und den entsprechenden Parametern (z.B. die Kopplungskonstante γ in Gl. (1.33)) in der *effektiven* freien Energie, die das makroskopische Verhalten beschreiben. Die vorliegende Arbeit stellt dieses fehlende Glied her.

In Kap. 3 leiten wir einen ähnlichen Ausdruck wie in Gl. (1.33) ab, ausgehend von einer mikroskopische Flüssigkeitstheorie. Das Fluid wird als eine Menge von nicht interagierenden magnetischen Scheiben betrachtet. Der NLC wurde als kontinuierliches Dispersionsmedium berücksichtigt, das in Wechselwirkung mit den Kolloiden steht, und durch den nematischen Direktor $\mathbf{n}(\mathbf{r})$ beschrieben wird. Jedes Kolloid ist an die nematische Umgebung durch die Verankerung (“anchoring”) der NLC-Moleküle an die kolloidalen Oberfläche gekoppelt. Wir betrachteten den Fall einer homöotropen Verankerung, d.h. der nematische Direktor bevorzugt, senkrecht zur Oberfläche des Kolloids zu stehen. Dies bedeutet, dass die Rotation des in der nematischen Substanz dispergierten Kolloids Verzerrungen des flüssigkristallinen Materials und damit das Vorhandensein eines effektiven elastischen Ein-Teilchen-Potenzials induziert. Dieses Potenzial wurde in Abschnitt 3.2.2 unter Berücksichtigung der freien Energie *mikroskopischer* Verzerrungen explizit abgeleitet. Die Validität des abgeleiteten elastischen Ein-Teilchen-Potenzials wurde numerisch überprüft und wir haben festgestellt, dass es gültig ist, solange die mikroskopische Kopplungskonstante c (Definition siehe Abschnitt 3.2.2) ausreichend klein ist (d.h. wenn $c < 0.1$ ist, was auf die Parameter in Ref. [102] zutrifft). Es konnte gezeigt werden, dass das effektive elastische Ein-Teilchen-Potenzial sich als Potenzreihe in c darstellen lässt. Aufgrund der topologischen Ähnlichkeit des vorliegenden Falles mit dem einer sehr dünnen Scheibe mit homöotroper Verankerung stimmt die erste Ordnung mit dem früheren Ergebnis (siehe Ref. [144]) für den Fall von langen stäbchenförmigen Teilchen mit planarer Verankerung überein. Die zweite Ordnung wurde aus einer Analogie zwischen dem entsprechenden Grenzwertproblem und der aus der Elektrostatik bekannten Aufgabenstellung, das Potenzial einer gleichmäßig geladenen Scheibe zu finden, abgeleitet.

Das effektive elastische Ein-Teilchen-Potenzial wurde als externes Potenzial interpretiert, welches auf die Orientierungsfreiheitsgrade von Kolloiden wirkt. Das entsprechende Dichtefunktional wurde unter der Einschränkung eines vorgegebenen Magnetisierungsprofils $\mathbf{M}(\mathbf{r})$ minimiert. Die daraus resultierende Euler-Lagrange-Gleichung enthielt einen Lagrange-Multiplikator, der im Allgemeinen nicht eliminiert werden konnte. Es wurde eine quadratische Approximation angenommen, die eine analytische Eliminierung des Lagrange-Multiplikators ermöglicht. Es konnte gezeigt werden, dass diese Näherung keine großen Fehler in der Beschreibung hervorruft. Dadurch wurde eine freie Energiedichte abgeleitet, die von zwei räumlich variierenden makroskopischen Feldern abhängt: dem Magnetisierungsfeld $\mathbf{M}(\mathbf{r})$ und dem Direktorfeld $\mathbf{n}(\mathbf{r})$. Dieser Ausdruck enthält Terme, die proportional zu $|\mathbf{M}(\mathbf{r})|^2$ und $(\mathbf{M}(\mathbf{r}) \cdot \mathbf{n}(\mathbf{r}))^2$ sind und somit direkt mit dem entsprechenden Ausdruck von Mertelj et al. verglichen werden können (siehe Gl. (1.33)). Die Ausdrücke für den Koeffizienten a und die Kopplungskonstante γ in Abhängigkeit der mikroskopischen Parameter der Flüssigkeit wurden abgeleitet. Das Fehlen des zu $|\mathbf{M}(\mathbf{r})|^4$ proportionalen Terms ist ohne Folgen, da der Koeffizient

von $|\mathbf{M}(\mathbf{r})|^2$ positiv ist. Die explizite Abhängigkeit der Kopplungskonstante γ von der mikroskopischen Kopplungskonstante c deutet an, dass γ nicht durch Terme $\propto c^n$, $n > 1$, für $c < 0.04$ im effektiven elastischen Ein-Teilchen-Potenzial beeinflusst wird und bereits ein Term linear in c in diesem Fall ausreichend ist.

In Kap. 4 haben wir die in Kap. 3 abgeleitete freie Energiedichte verwendet, um das Verhalten einer gleichmäßig magnetisierten ferronematischen Substanz, die zwischen zwei parallelen und planaren Wänden angeordnet ist, zu untersuchen. Dieser Aufbau ist von Relevanz für die Experimente in Refs. [102, 148] und stellt einen einfachen Fall einer begrenzten ferronematischen Substanz dar. Wir nahmen an, dass die Wände mit dem NLC gekoppelt sind und gaben dem nematischen Direktor eine Vorzugsrichtung vor. Die zahlreichen relevanten Richtungen (d.h. die Richtung der anfänglichen Magnetisierung, die Vorzugsrichtung des Direktors und die Richtung des äußeren Magnetfeldes) ermöglichen eine Vielfalt von makroskopischen Antworten des Systems und daher wird das Verhalten stark durch die konkrete Wahl der gegenseitigen Orientierungen zwischen diesen Richtungen beeinflusst. Wenn, zum Beispiel, das äußere Magnetfeld *senkrecht* zur Richtung der anfänglichen Magnetisierung der gleichmäßig magnetisierten Probe ausgerichtet wird, beobachtet man eine *schwellenlose* Verformung der ferronematischen Substanz (siehe Abschnitt 1.2.4 für eine Literaturübersicht). Andererseits haben wir uns mit dem Fall beschäftigt, dass das externe Feld *antiparallel* zur anfänglichen Richtung der Magnetisierung angelegt wird. Experimentell wurde gezeigt (siehe Ref. [102]), dass in diesem Fall ein *kritisches* Magnetfeld B_{cr} vorliegt, d.h. es gibt eine *Schwelle*, unterhalb derer die ferronematische Substanz vom Feld unbeeinflusst bleibt. Wir erhielten das kritische Feld in Abhängigkeit von der Kopplungskonstante γ und der Verankerungsstärke des NLC an den Wänden W_{wall} numerisch durch Minimierung des entsprechenden Energiefunktional (siehe Gl. (4.2)). Die erhaltenen Hystereseschleifen (d.h. $\mathcal{M}(B)$, wobei \mathcal{M} die dimensionslose x -Komponente der Magnetisierung der Probe (siehe Abb. 4.1) und B die Magnetfeldstärke ist) sind ähnlich zu denen, welche im Experiment erzeugt wurden. Die berechnete Abhängigkeit $B_{\text{cr}}(\gamma, W_{\text{wall}})$ (siehe Abb. 4.5) zeigte, dass das kritische Feld mit zunehmendem γ oder W_{wall} zunimmt. Der Absolutwert dieses Anstiegs in Abhängigkeit von der Verankerungsstärke W_{wall} liegt jedoch nur in der Größenordnung von 10^{-2} mT für $W_{\text{wall}} \geq 1 \times 10^{-5}$ J/m² und er scheint ein Plateau $B_{\text{cr}} = B_{\text{cr}}(\gamma)$ für starke Verankerung an der Wand zu erreichen (für $W_{\text{wall}} > 8 \times 10^{-5}$ J/m², falls $\gamma \approx 195$ (siehe Abb. 4.6(a))). Die Autoren von Ref. [102] leiteten einen Ausdruck für B_{cr} unter der Annahme ab, dass $W_{\text{wall}} = \infty$ (d.h. starre Verankerung des NLC an den Wänden). Wir verglichen das Ergebnis unseres numerischen Ansatzes mit ihrem Ausdruck für $W_{\text{wall}} = 4 \times 10^{-5}$ J/m² und stellten den Vergleich als Funktion von γ in Abb. 4.6(b) dar. Es ist interessant, dass die Ergebnisse, die durch zwei völlig unterschiedliche Ansätze gewonnen wurden (numerische Minimierung der freien Energie in der vorliegenden Ar-

beit und der Ausdruck auf der Grundlage des Arguments, dass die Relaxationszeit der thermischen Schwankungen des nematischen Direktors im kritischen Bereich divergieren), nahezu perfekt übereinstimmen, sogar für *endliche* Wert der Verankerungsstärke.

Die Abhängigkeit des kritischen Feldes von der Kopplungskonstante γ ist wichtig im Zusammenhang mit der experimentellen Realisierung des Systems. In der Tat, unter Verwendung der Ergebnisse von Kap. 3, insbesondere in Kenntniss des Zusammenhangs zwischen γ und der mikroskopischen Kopplungskonstanten c und damit der Teilchengröße R , kann man die Abhängigkeit $B_{\text{cr}}(c)$ bestimmen und damit das kritische Feld einstellen, indem man die Position des Maximums der Größenverteilung der Kolloide entsprechend anpasst. Ein Beispiel einer solchen Abhängigkeit für einen Wert $W_{\text{wall}} = 4 \times 10^{-5} \text{ J/m}^2$ ist in Abb. 4.6(c) dargestellt.

Der in der vorliegenden Studie implementierte numerische Algorithmus liefert ein lokales Minimum der freien Energie und ist somit in der Lage, metastabile Zustände des Systems zu finden. Die anfängliche Monodomäne ist das stabile Minimum, wenn kein externes Magnetfeld angelegt wird. Wenn das Feld antiparallel zur anfänglichen Magnetisierungsrichtung angelegt ist, wird der Ausgangszustand metastabil und das globale Minimum entspricht der einheitlichen Monodomäne, die entlang des Feldes magnetisiert ist. Die Zustände, die den einzelnen Punkten der Hystereseschleife mit $\mathcal{M} \neq \pm 1$ entsprechen (siehe Abb. 4.2) können als ein Weg betrachtet werden, welchem das System folgt, bevor es den Gleichgewichtszustand annimmt. Wir haben festgestellt, dass wenn die Verankerungsstärke W_{wall} an beiden Wänden gleich ist, es zwei mögliche Wege gibt, denen das System folgen kann. Da jeder “Weg” zwei Punkte im Zustandsraum verbindet, welche experimentellen Proben entsprechen, die gleichmäßig in entgegengesetzte Richtungen magnetisiert sind, bezeichnen wir jeden Weg als einen “Schaltmechanismus”. Wir untersuchten, welcher Schaltmechanismus in Abhängigkeit von W_{wall} und γ realisiert wird (siehe Abb. 4.8).

Die erste Möglichkeit, die wir als Schaltmechanismus I bezeichnen, entspricht größeren Werten von W_{wall} . Das wesentliche Merkmal dieses Mechanismus ist die Bildung von Schichten in der Nähe der Wände, in denen die Magnetisierung “umkippt” und in die Richtung entlang des Feldes ausgerichtet ist (siehe Abb. 4.3(c)). Der nematische Direktor kann jedoch aufgrund der starken Verankerung an den Wänden keine ca. 180° Rotation durchführen. Mit zunehmendem externen Feld erstrecken sich diese Schichten der geschalteten Magnetisierung hin zum Inneren der Probe, bis die Magnetisierung durch die gesamte Probe entlang des externen Feldes ausgerichtet ist.

Die zweite Möglichkeit, die wir als Schaltmechanismus II bezeichnen, entspricht kleineren Werten der “anchoring”-Stärke W_{wall} . Im Gegensatz zum vorherigen Fall werden die Schichten mit umgedrehter Magnetisierung nicht gebildet. Stattdessen dreht sich das Magnetisierungsfeld kontinuierlich, um sich entlang dem externen Magnetfeld

auszurichten. Dabei ist es in der Lage, den nematischen Direktor mitzudrehen. Die Kopplung der nematischen Substanz an die Wände ist nicht stark genug, um die Rotation des Direktors in Wandnähe zu unterdrücken.

Die “Dominanzgebiete” der beiden Schaltmechanismen in Abhängigkeit von W_{wall} und γ sind in Abb. 4.8 dargestellt. Es kann gefolgert werden, dass für den Wert von $\gamma \approx 200$ (ungefähr der Wert aus dem Experiment in Ref. [102]) der Schaltmechanismus II nur für sehr kleine Verankerungsstärken $W_{\text{wall}} \leq 0.2 \times 10^{-5} \text{ J/m}^2$ realisiert wird, während der aus dem Experiment geschätzte Wert $W_{\text{wall}}^{\text{exp}} = 3.4 \times 10^{-5} \text{ J/m}^2$ weit darüber liegt. Wir kommen daher zu dem Schluss, dass im Experiment der Schaltmechanismus I realisiert wird.

Eine interessante Frage, die man sich stellen kann, ist, was passiert, wenn Wände mit *unterschiedlichen* Verankerungsstärken $W_{\text{wall}}^{(1)} \neq W_{\text{wall}}^{(2)}$ in einem System kombiniert werden. Diese Verallgemeinerung bedeutet nicht, dass die Komplexität des Problems aus numerischer Sicht erhöht wird, weil lediglich eine Inhomogenität der Randbedingungen entlang der z -Achse hinzugefügt wird. Somit bleibt das System effektiv eindimensional. Als ein interessantes Ergebnis haben wir Werte für $W_{\text{wall}}^{(1)}$, $W_{\text{wall}}^{(2)}$, und γ gefunden, für die beim Anlegen eines externen Magnetfeldes nicht Schaltmechanismus I oder II, sondern eine *Kombination* beider vorliegt (siehe Abb. 4.9). Durch Erreichen einer bestimmten Stärke des Magnetfeldes nimmt die Probe einen Zustand an, in dem die Magnetisierung nahezu homogen ist und in Richtung des Magnetfeldes zeigt, während der nematische Direktor verzerrt ist (siehe Abb. 4.9). Wenn wir dann das Feld abrupt ausschalten, weist die Probe zwei entgegengesetzt magnetisierte Bereiche auf (siehe Abb. 4.11(c)). Wird das Feld nun wieder eingeschaltet, diesmal aber in *entgegengesetzter* Richtung, wird die Probe in den anfänglichen Zustand einer einheitlichen Monodomäne zurückgebracht. Somit kann man prinzipiell zwischen der Monodomäne und dem “Zwei-Domänen”-Zustand durch Anlegen eines äußeren Magnetfeldes in geeignete Richtungen wechseln. Dies eröffnet die Möglichkeit einer hypothetischen Informationsspeichervorrichtung, bestehend aus solchen ferronematischen Zellen. Jede Zelle würde ein Bit darstellen, welches durch die Magnetisierung kodiert ist, d.h. entweder $\mathcal{M} \approx 1$ (Monodomäne) oder $\mathcal{M} \ll 1$ (Zustand mit zwei Domänen).

Der Segregationseffekt (d.h. die räumliche Umverteilung der kolloidalen Teilchen im magnetischen Feld) wurde untersucht, durch Betrachten eines räumlich variierenden Betrages der Magnetisierung, d.h. $|\mathbf{M}| = |\mathbf{M}(z)|$. Für Kolloidabstände kleiner als $60 \mu\text{m}$ lieferte der numerische Algorithmus unphysikalische Ergebnisse (d.h. $|\mathbf{M}| < 0$). Wir erklären dies durch das Fehlen von Termen höherer Ordnung in $|\mathbf{M}|$ in der effektiven freien Energie der ferronematischen Substanz (siehe Kap. 3). Die physikalisch gültigen Ergebnisse wurden für Kolloidabstände größer als $60 \mu\text{m}$ erhalten. Es wurde festgestellt, dass die Segregation die diskutierten Schaltmechanismen qualitativ nicht beeinflusst. Im

Fall von Schaltmechanismus I wurde die Bildung einer Verarmungsschicht (“depletion layer”) in der Nähe der Wand festgestellt. Diese Schicht ist jedoch etwas von der Wand entfernt, im Gegensatz zu jener in Ref. [85], welche sich direkt an der Wand befindet. Dieser Effekt ist die Folge der endlichen Kopplungsstärke des nematischen Direktors und des Magnetisierungsfeldes.

Wir haben festgestellt, dass für Abstände größer als $95 \mu\text{m}$ die Kombination beider Schaltmechanismen auch bei zwei Wänden mit der *selben* starken Verankerung erreicht werden kann. Möglich wird dieses Phänomen, da bei größeren Abständen der Bereich inmitten der Kolloide ausreichend weit von den Wänden entfernt ist. Daher kann sich der nematische Direktor gemeinsam mit der Magnetisierung frei drehen.

Appendix A

Boundary problems for $\alpha^{(0)}$ and $\alpha^{(1)}$

Solving the boundary problem in Eq. (3.8) analytically is difficult due to the nonlinearity of the boundary condition at the disc surface. However, the expansion in Eq. (3.9) of the scalar field α in terms of powers of the coupling constant c generates a set of boundary problems corresponding to $\alpha^{(0)}, \alpha^{(1)}, \dots$, which are much simpler. In the following the boundary problems for $\alpha^{(0)}$ and $\alpha^{(1)}$ are solved, and the free energy in Eq. (3.7) is determined by inserting the expansion into Eq. (3.9) up to terms $n \leq 1$, i.e., with the equilibrium expressions for $\alpha^{(0)}$ and $\alpha^{(1)}$.

A.1 Zeroth order in c

The boundary problem corresponding to $\alpha^{(0)}$ is posed as

$$\begin{cases} \nabla^2 \alpha^{(0)}(\mathbf{r}) = 0 & , \mathbf{r} \in \mathcal{V} \\ \nabla \alpha^{(0)}(\mathbf{s}) \cdot \boldsymbol{\nu}(\mathbf{s}) = 0 & , \text{at disc surface} \\ \alpha^{(0)}(\mathbf{r}) \simeq \theta & , |\mathbf{r}| \gg R. \end{cases} \quad (\text{A.1})$$

From Eq. (3.9) one infers $\alpha = \alpha^{(0)}$ for $c = 0$ which corresponds to the limit of a decoupling of the liquid crystal and the colloid. Therefore, in this limit the nematic director $\mathbf{n}(\mathbf{r})$ is not distorted by the presence of the colloidal disc, i.e., physical intuition leads to the uniform scalar field

$$\alpha^{(0)}(\mathbf{r}) = \theta. \quad (\text{A.2})$$

It can be readily verified that this is indeed the solution of Eq. (A.1).

A.2 First order in c

Using Eq. (A.2), the boundary problem corresponding to $\alpha^{(1)}$ is

$$\left\{ \begin{array}{ll} \nabla^2 \alpha^{(1)}(\mathbf{r}) = 0 & , \mathbf{r} \in \mathcal{V} \\ \nabla \alpha^{(1)}(\mathbf{s}) \cdot \boldsymbol{\nu}(\mathbf{s}) = \frac{\sin(2\alpha^{(0)}(\mathbf{s}))}{R} \\ & = \frac{\sin(2\theta)}{R} & , \text{ at disc surface} \\ \alpha^{(1)}(\mathbf{r}) \simeq 0 & , |\mathbf{r}| \gg R. \end{array} \right. \quad (\text{A.3})$$

By identifying $\alpha^{(1)}(\mathbf{r})$ with an electrostatic potential $\lambda\varphi(\mathbf{r})$, where λ is a constant with the dimension of an inverse voltage, one can map Eq. (A.3) into the problem of finding the electrostatic potential φ of a thin, uniformly charged disc with radius R and surface charge density $\sigma = -\varepsilon_0 \sin(2\theta)/(\lambda R)$. This is given by [150]

$$\varphi(\rho, z) = \frac{\sigma R}{\varepsilon_0} \int_0^\infty \frac{dk}{k} J_0(k\rho) J_1(kR) \exp(-k|z|), \quad (\text{A.4})$$

where $\rho := \sqrt{x^2 + y^2}$ is the distance from the z -axis and where J_i denotes the Bessel function of order i . With the necessary replacements one obtains the solution of Eq. (A.3) in the form

$$\alpha^{(1)}(\rho, z) = -\sin(2\theta) \int_0^\infty \frac{dk}{k} J_0(k\rho) J_1(kR) \exp(-k|z|). \quad (\text{A.5})$$

A.3 Free energy

By using Eq. (A.2) in Eq. (3.9), the expansion of the scalar field α in terms of powers of the coupling constant c is given by

$$\alpha(\mathbf{r}) = \theta + c\alpha^{(1)}(\mathbf{r}) + \mathcal{O}(c^2). \quad (\text{A.6})$$

Inserting this expression into the free energy functional in Eq. (3.7) one obtains

$$\begin{aligned} \frac{F[\alpha]}{KR} &= \frac{c^2}{2R} \int_{\mathcal{V}} d^3r [\nabla \alpha^{(1)}(\mathbf{r})]^2 + \frac{c}{R^2} \int_{\partial\mathcal{V}} d^2s [\sin(\alpha(\mathbf{s}))]^2 \\ &+ \mathcal{O}(c^3), \end{aligned} \quad (\text{A.7})$$

where

$$\begin{aligned} [\sin(\alpha(\mathbf{s}))]^2 &= [\sin(\theta + c\alpha^{(1)}(\mathbf{s}) + \mathcal{O}(c^2))]^2 \\ &= [\sin\theta + c\cos\theta\alpha^{(1)}(\mathbf{s}) + \mathcal{O}(c^2)]^2 \\ &= (\sin\theta)^2 + 2c\sin\theta\cos\theta\alpha^{(1)}(\mathbf{s}) + \mathcal{O}(c^2). \end{aligned} \quad (\text{A.8})$$

In order to calculate the volume integral in Eq. (A.7) one can use Green's first identity

$$\begin{aligned} & \int_{\mathcal{V}} d^3r \left[\alpha^{(1)}(\mathbf{r}) \nabla^2 \alpha^{(1)}(\mathbf{r}) + \nabla \alpha^{(1)}(\mathbf{r}) \cdot \nabla \alpha^{(1)}(\mathbf{r}) \right] \\ &= \int_{\partial \mathcal{V}} d^2s \alpha^{(1)}(\mathbf{s}) \nabla \alpha^{(1)}(\mathbf{s}) \cdot \boldsymbol{\kappa}(\mathbf{s}) \end{aligned} \quad (\text{A.9})$$

where $\boldsymbol{\kappa}(\mathbf{s})$ is the outer normal at the point $\mathbf{s} \in \partial \mathcal{V}$. The first term in the volume integral in Eq. (A.9) vanishes due to the first line of Eq. (A.3). Moreover,

$$\int_{\partial \mathcal{V}} d^2s \alpha^{(1)}(\mathbf{s}) \nabla \alpha^{(1)}(\mathbf{s}) \cdot \boldsymbol{\kappa}(\mathbf{s}) = \int_{|\mathbf{s}|=\text{const} \gg R} d^2s \alpha^{(1)}(\mathbf{s}) \nabla \alpha^{(1)}(\mathbf{s}) \cdot \boldsymbol{\kappa}(\mathbf{s}) - \int_{\text{disc}} d^2s \alpha^{(1)}(\mathbf{s}) \nabla \alpha^{(1)}(\mathbf{s}) \cdot \boldsymbol{\nu}(\mathbf{s}), \quad (\text{A.10})$$

where $\boldsymbol{\nu}(\mathbf{s}) = -\boldsymbol{\kappa}(\mathbf{s})$ is the normal of the disc surface. The first integral on the right-hand side of Eq. (A.10) vanishes due to the third line of Eq. (A.3). This leads to

$$\frac{c^2}{2R} \int_{\mathcal{V}} d^3r \left[\nabla \alpha^{(1)}(\mathbf{r}) \right]^2 = -\frac{c^2}{2R} \int_{\text{disc}} d^2s \alpha^{(1)}(\mathbf{s}) \nabla \alpha^{(1)}(\mathbf{s}) \cdot \boldsymbol{\nu}(\mathbf{s}). \quad (\text{A.11})$$

Finally, by using Eqs. (A.3), (A.8), and (A.11), Eq. (A.7) turns into

$$\begin{aligned} \frac{F[\alpha]}{KR} &= \int_{\text{disc}} d^2s \left[\frac{c}{R^2} (\sin \theta)^2 + \frac{2c^2}{R^2} \sin \theta \cos \theta \alpha^{(1)}(\mathbf{s}) - \frac{c^2}{2R} \alpha^{(1)}(\mathbf{s}) \nabla \alpha^{(1)}(\mathbf{s}) \cdot \boldsymbol{\nu}(\mathbf{s}) \right] + \mathcal{O}(c^3) \\ &= 2\pi c (\sin \theta)^2 + \frac{c^2}{2R^2} \sin(2\theta) \int_{\text{disc}} d^2s \alpha^{(1)}(\mathbf{s}). \end{aligned} \quad (\text{A.12})$$

Inserting Eq. (A.5) with $z = 0$ into the last integral one obtains

$$\begin{aligned} \int_{\text{disc}} d^2s \alpha^{(1)}(\mathbf{s}) &= 2 \int_0^R d\rho \rho \int_0^{2\pi} d\varphi (-\sin(2\theta)) \int_0^\infty \frac{dk}{k} J_0(k\rho) J_1(kR) \\ &= -4\pi R \sin(2\theta) \int_0^\infty \frac{dk}{k^2} (J_1(kR))^2 \\ &= -\frac{16}{3} R^2 \sin(2\theta), \end{aligned} \quad (\text{A.13})$$

(the prefactor of 2 in front of the integral in the first term on the right-hand side of Eq. (A.13) accounts for the two faces of the disc surface) so that

$$\begin{aligned} \frac{F}{KR} &= 2\pi c (\sin \theta)^2 - \frac{8}{3} c^2 (\sin(2\theta))^2 + \mathcal{O}(c^3) \\ &= \text{const} - (2\pi c + \frac{32}{3} c^2) (\mathbf{n}_0 \cdot \boldsymbol{\omega})^2 + \frac{32}{3} c^2 (\mathbf{n}_0 \cdot \boldsymbol{\omega})^4 + \mathcal{O}(c^3), \end{aligned} \quad (\text{A.14})$$

which, upon ignoring the irrelevant constant term, leads to Eq. (3.10).

Appendix B

Quadratic approximation of the generating function $Z(\mathbf{h})$

In the following we provide a detailed derivation of Eq. (3.29) within the quadratic approximation (see Eq. (3.25)) of the generating function introduced in Eq. (3.20).

The generating function $Z(\mathbf{h})$ in Eq. (3.20) can be rewritten as

$$Z(\mathbf{h}) = \int d^2\omega f(\mathbf{n}(\mathbf{r}) \cdot \boldsymbol{\omega}) \exp(\mathbf{h} \cdot m\boldsymbol{\omega}) \quad (\text{B.1})$$

with $f(x) := \exp(A_1x^2 + A_2x^4)$.

As a first step, we show that $Z(\mathbf{h})$ is an even function $\bar{Z}(H, u)$ of both $H := m|\mathbf{h}|$ and $u := \mathbf{n} \cdot \mathbf{h}/|\mathbf{h}|$. To this end we consider an appropriate coordinate system such that the z -axis points along the local director field $\mathbf{n}(\mathbf{r})$ and the x -axis is chosen in an arbitrary direction in the plane perpendicular to $\mathbf{n}(\mathbf{r})$. (Note the difference in the meaning of θ and α between Eq. (B.2) and Fig. 3.1.)

$$\mathbf{n} = \begin{bmatrix} 0 \\ 0 \\ 1 \end{bmatrix}, \quad \boldsymbol{\omega} = \begin{bmatrix} \sin \theta \cos \varphi \\ \sin \theta \sin \varphi \\ \cos \theta \end{bmatrix}, \quad \mathbf{h} = \frac{H}{m} \begin{bmatrix} \sin \alpha \cos \beta \\ \sin \alpha \sin \beta \\ \cos \alpha \end{bmatrix} =: \frac{H}{m} \mathbf{v} \quad (\text{B.2})$$

so that $|\mathbf{v}| = 1$ and $u = \mathbf{n} \cdot \mathbf{v} = \cos \alpha$. With this choice Eq. (B.1) takes the form

$$\begin{aligned} Z(\mathbf{h}) &= \int_0^\pi d\theta \sin \theta f(\cos \theta) \int_0^{2\pi} d\varphi \exp [H(\sin \alpha \sin \theta \cos(\varphi - \beta) + \cos \alpha \cos \theta)] \\ &= 2\pi \int_{-1}^1 dx f(x) I_0(H\sqrt{1-u^2}\sqrt{1-x^2}) \exp(Hux) \\ &=: \bar{Z}(H, u), \end{aligned} \quad (\text{B.3})$$

where I_0 is a modified Bessel function of order 0 (see Ref. [151], Eq. (8.431.3)). Since $f(x)$ is an even function of x , one can infer from Eq. (B.3) that $\bar{Z}(H, u)$ is an even function of both H and u .

Using Eq. (3.22) one can express the magnetization \mathbf{M} in terms of H and u :

$$\frac{\mathbf{M}}{\zeta} = \frac{\partial Z}{\partial \mathbf{h}} = \frac{\partial H}{\partial \mathbf{h}} \frac{\partial \bar{Z}}{\partial H} + \frac{\partial u}{\partial \mathbf{h}} \frac{\partial \bar{Z}}{\partial u} \quad (\text{B.4})$$

with

$$\begin{aligned} \frac{\partial H}{\partial h_i} &= \frac{\partial}{\partial h_i} m |\mathbf{h}| = m \frac{h_i}{|\mathbf{h}|} \\ \Rightarrow \frac{\partial H}{\partial \mathbf{h}} &= m \frac{\mathbf{h}}{|\mathbf{h}|} = m \mathbf{v} \end{aligned} \quad (\text{B.5})$$

and

$$\begin{aligned} \frac{\partial u}{\partial h_i} &= \frac{\partial}{\partial h_i} \frac{\mathbf{n} \cdot \mathbf{h}}{|\mathbf{h}|} = \frac{n_i}{|\mathbf{h}|} - (\mathbf{n} \cdot \mathbf{h}) \frac{h_i}{|\mathbf{h}|^3} \\ \Rightarrow \frac{\partial u}{\partial \mathbf{h}} &= \frac{1}{|\mathbf{h}|} \left(\mathbf{n} - \frac{\mathbf{n} \cdot \mathbf{h}}{|\mathbf{h}|} \frac{\mathbf{h}}{|\mathbf{h}|} \right) = \frac{m}{H} (\mathbf{n} - u \mathbf{v}). \end{aligned} \quad (\text{B.6})$$

In the next step, we consider the quantities $T = |\mathbf{M}|/(m\zeta)$ and $t = \mathbf{n} \cdot \mathbf{M}/(m\zeta)$ which are related to H and u via

$$\begin{aligned} t &= \frac{\mathbf{n} \cdot \mathbf{M}}{m\zeta} = u \frac{\partial \bar{Z}}{\partial H} + \frac{1-u^2}{H} \frac{\partial \bar{Z}}{\partial u} \\ T^2 &= \left(\frac{\mathbf{M}}{m\zeta} \right)^2 = \left(\frac{\partial \bar{Z}}{\partial H} \right)^2 + \frac{1-u^2}{H^2} \left(\frac{\partial \bar{Z}}{\partial u} \right)^2. \end{aligned} \quad (\text{B.7})$$

Since an analytical expression for the integral in Eq. (3.20) is not available, it is rewritten as a series in powers of $|\mathbf{h}|$:

$$\begin{aligned} Z(\mathbf{h}) &= \int d^2 \omega \exp(A_1(\mathbf{n} \cdot \boldsymbol{\omega})^2 + A_2(\mathbf{n} \cdot \boldsymbol{\omega})^4) \exp(\mathbf{h} \cdot m \boldsymbol{\omega}) \\ &= \int d^2 \omega \exp(A_1(\mathbf{n} \cdot \boldsymbol{\omega})^2 + A_2(\mathbf{n} \cdot \boldsymbol{\omega})^4) \sum_{k=0}^{\infty} \frac{1}{k!} (\mathbf{h} \cdot m \boldsymbol{\omega})^k \\ &= \sum_{k=0}^{\infty} \frac{1}{(2k)!} \int d^2 \omega \exp(A_1(\mathbf{n} \cdot \boldsymbol{\omega})^2 + A_2(\mathbf{n} \cdot \boldsymbol{\omega})^4) (\mathbf{h} \cdot m \boldsymbol{\omega})^{2k} \\ &= \sum_{k=0}^{\infty} Z_k(H, u). \end{aligned} \quad (\text{B.8})$$

We note that $Z_k = 0$ for k odd. Since here the ultimate goal is to derive Eq. (3.29), expressions of H and u in terms of T and t are required, which are obtained by inverting the map $(H, u) \rightarrow (T, t)$ in Eq. (B.7). However, an inversion of Eq. (B.7) in closed form is feasible only when the series in Eq. (B.8) is restricted to sufficiently low orders. In the following only the terms $Z_k(H, u)$ with $k \leq 1$ are considered. The term $Z_{k=0}(H, u)$ in

Eq. (B.8) is given by

$$\begin{aligned}
Z_0(H, u) &= \int d^2\omega \exp(A_1(\mathbf{n} \cdot \boldsymbol{\omega})^2 + A_2(\mathbf{n} \cdot \boldsymbol{\omega})^4) \\
&= \int_0^{2\pi} d\varphi \int_0^\pi d\theta \sin\theta \exp(A_1 \cos^2\theta + A_2 \cos^4\theta) \\
&= 2\pi \int_{-1}^1 dx \exp(A_1 x^2 + A_2 x^4) \\
&=: 2\pi \mathcal{I}_0(A_1, A_2) \\
&=: Y_{00},
\end{aligned} \tag{B.9}$$

whereas the term $Z_{k=1}(H, u)$ in Eq. (B.8) is given by

$$\begin{aligned}
Z_1(H, u) &= \frac{1}{2} \int d^2\omega \exp(A_1(\mathbf{n} \cdot \boldsymbol{\omega})^2 + A_2(\mathbf{n} \cdot \boldsymbol{\omega})^4) (\mathbf{h} \cdot m\boldsymbol{\omega})^2 \\
&= \frac{H^2}{2} \int d^2\omega \exp(A_1(\mathbf{n} \cdot \boldsymbol{\omega})^2 + A_2(\mathbf{n} \cdot \boldsymbol{\omega})^4) (\sin\alpha \sin\theta \cos(\varphi - \beta) + \cos\alpha \cos\theta)^2 \\
&= \frac{H^2}{2} \int d^2\omega \exp(A_1(\cos\theta)^2 + A_2(\cos\theta)^4) \left[(\sin\alpha \sin\theta \cos(\varphi - \beta))^2 + \right. \\
&\quad \left. 2 \sin\alpha \cos\alpha \sin\theta \cos\theta \cos(\varphi - \beta) + \right. \\
&\quad \left. (\cos\alpha \cos\theta)^2 \right] \\
&= \frac{H^2}{2} \int_{-1}^1 dx \exp(A_1 x^2 + A_2 x^4) \left[\pi(1 - x^2)(\sin\alpha)^2 + 2\pi x^2(\cos\alpha)^2 \right] \\
&= \pi \frac{H^2}{2} \left[(1 - u^2) \int_{-1}^1 dx \exp(A_1 x^2 + A_2 x^4) + (3u^2 - 1) \int_{-1}^1 dx x^2 \exp(A_1 x^2 + A_2 x^4) \right] \\
&=: \pi \frac{H^2}{2} \left[(1 - u^2) \mathcal{I}_0(A_1, A_2) + (3u^2 - 1) \mathcal{I}_1(A_1, A_2) \right] \\
&=: Y_{10} H^2 + Y_{12} H^2 u^2
\end{aligned} \tag{B.10}$$

with

$$Y_{10} := \frac{\pi}{2} (\mathcal{I}_0 - \mathcal{I}_1), \quad Y_{12} := \frac{\pi}{2} (3\mathcal{I}_1 - \mathcal{I}_0). \tag{B.11}$$

This leads to the ‘‘quadratic’’ approximation

$$\begin{aligned}
\bar{Z}(H, u) &\approx Z_0(H, u) + Z_1(H, u) \\
&= Y_{00} + Y_{10} H^2 + Y_{12} H^2 u^2.
\end{aligned} \tag{B.12}$$

Inserting Eq. (B.12) into Eq. (B.7) one obtains

$$\begin{cases} t^2 &= 4(Y_{10} + Y_{12})^2 H^2 u^2 \\ T^2 &= 4Y_{10}^2 H^2 + (8Y_{10}Y_{12} + 4Y_{12}^2) H^2 u^2. \end{cases} \tag{B.13}$$

which leads to

$$\begin{cases} H^2 u^2 &= \frac{t^2}{4(Y_{10}+Y_{12})^2} \\ H^2 &= \frac{1}{4Y_{10}^2} \left(T^2 - \frac{t^2(2Y_{10}Y_{12}+Y_{12}^2)}{(Y_{10}+Y_{12})^2} \right). \end{cases} \quad (\text{B.14})$$

Finally, that part of the integrand in Eq. (3.23), which depends on Z , is

$$\begin{aligned} \mathbf{h} \cdot \frac{\partial Z}{\partial \mathbf{h}} - Z &= H \frac{\partial \bar{Z}}{\partial H} - \bar{Z} \\ &= C_{00} + C_{20} T^2 + C_{02} t^2, \end{aligned} \quad (\text{B.15})$$

where

$$C_{00} := -Y_{00} \quad (\text{B.16})$$

$$C_{20} := \frac{1}{4Y_{10}} \quad (\text{B.17})$$

$$C_{02} := -\frac{Y_{12}/Y_{10}}{4(Y_{10} + Y_{12})}, \quad (\text{B.18})$$

which, upon insertion into Eq. (3.23), leads to Eq. (3.27). Equation (3.29) follows from expressing T and t in terms of $|\mathbf{M}|$ and $\mathbf{M} \cdot \mathbf{n}$.

As expected, the quadratic approximation becomes poorer the larger H is. However, it turns out to be a reasonable approximation within the physically relevant range of H (see Sec. 3.4). In contrast, if in Eq. (B.8) one keeps terms with $k > 1$, $(T(H, u))^2$ and $(t(H, u))^2$ in Eq. (B.13) are polynomials of at least degree 2 in H^2 and $H^2 u^2$. In this case H^2 and $H^2 u^2$ are not polynomials in T^2 and t^2 , which implies that Eq. (B.15), and therefore the integrand given in Eq. (3.36) for Eq. (3.29), is not represented by a polynomial and thus cannot be compared with the expression in Eq. (3.37).

Appendix C

Constraint of the field $\tau(z)$

In this Appendix we derive Eq. (4.10).

The spatially varying magnetization field $\mathbf{M}(z)$ was defined in Ref. [160] as

$$\mathbf{M}(z) = \int d^2\omega \, m\omega \rho(z, \omega), \quad (\text{C.1})$$

where m is the magnitude and ω the direction of the magnetic moment of a single colloid and $\rho(z, \omega)$ is the number density of colloids in a layer around point z and oriented in direction ω . We *assume* that in a small layer around a given point z all individual magnetic moments point in one direction, i.e., the direction of $\mathbf{M}(z)$:

$$\rho(z, \omega) = g(z)\delta(\omega - \omega_0(z)), \quad (\text{C.2})$$

with $\omega_0(z) := \mathbf{M}(z)/|\mathbf{M}(z)|$ and $g(z)$ is the number density of colloids at point z regardless of their orientation. From the definition of ρ_{iso} it follows

$$\rho_{\text{iso}} = \frac{1}{D} \int_0^D dz \int d^2\omega \, \rho(z, \omega) = \frac{1}{D} \int_0^D dz \, g(z). \quad (\text{C.3})$$

Noting that

$$|\mathbf{M}(z)| = mg(z) \quad (\text{C.4})$$

and defining $\tau(z) := |\mathbf{M}(z)|/(m\rho_{\text{iso}}) = g(z)/\rho_{\text{iso}}$, Eq. (C.3) can be written in the form of Eq. (4.10):

$$1 = \frac{1}{D} \int_0^D dz \frac{g(z)}{\rho_{\text{iso}}} = \frac{1}{D} \int_0^D dz \, \tau(z). \quad (\text{C.5})$$

Using the definition $\delta\tau(z) := \tau(z) - 1$ (see Eq. (4.11)) this is equivalent to (see Eq. (4.14))

$$\int_0^D dz \, \delta\tau(z) = 0. \quad (\text{C.6})$$

Bibliography

- [1] R. J. Bushby and O. R. Lozman. *Discotic liquid crystals 25 years on*. Curr. Op. Coll. Interf. Sci. **7**, 343 (2002).
- [2] S. Laschat, A. Baro, N. Steinke, F. Giesselmann, C. Hägele, G. Scalia, R. Judele, E. Kapatsina, S. Sauer, A. Schreivogel, and M. Tosoni. *Discotic liquid crystals: from tailor-made synthesis to plastic electronics*. Angew. Chem. Int. Ed. **46**, 4832 (2007).
- [3] S. Kawano, M. Kato, S. Soumiya, M. Nakaya, J. Onoe, and K. Tanaka. *Columnar liquid crystals from a giant macrocycle mesogen*. Angew. Chem. Int. Ed. **57**, 167 (2018).
- [4] T. Kato, T. Yasuda, Y. Kamikawa, and M. Yoshio. *Self-assembly of functional columnar liquid crystals*. Chem. Commun. **7**, 729 (2009).
- [5] R. A. Reddy and C. Tschierske. *Bent-core liquid crystals: polar order, superstructural chirality and spontaneous desymmetrization in soft matter systems*. J. Mater. Chem. **16**, 907 (2006).
- [6] A. Metere, S. Sarman, T. Ooppelstrup, and M. Dzhugutov. *Formation of a columnar liquid crystal in a simple one-component system of particles*. Soft Matter **11**, 4606 (2015).
- [7] P. G. Cummins, D. A. Dunmur, and D. A. Laidler. *The dielectric properties of nematic 44' n-pentylcyanobiphenyl*. Mol. Cryst. Liq. Cryst. **30**, 109 (1975).
- [8] D. Meyerhofer. *Elastic and dielectric constants in mixtures of nematic liquid crystals*. J. Appl. Phys. **46**, 5084 (1975).
- [9] C. Maze. *Determination of nematic liquid crystal elastic and dielectric properties from the shape of a capacitance-voltage curve*. Mol. Cryst. Liq. Cryst. **48**, 273 (1978).
- [10] A. Bogi and S. Faetti. *Elastic, dielectric and optical constants of 4'-pentyl-4-cyanobiphenyl*. Liq. Cryst. **28**, 729 (2001).
- [11] R. Williams. *Liquid crystal in an electric field*. Nature **199**, 273 (1963).

- [12] P. D. Berezin, I. N. Kompanets, V. V. Nikitin, and S. A. Pikin. *Orienting effect of an electric field on nematic liquid crystals*. J. Exp. Theor. Phys. **37**, 305 (1972).
- [13] T. Kosa and P. Palffy-Muhoray. *Magnetic field induced deformations in nematic liquid crystals*. Liq. Cryst. Today **6**, 7 (1996).
- [14] A. Buka and W. H. De Jeu. *Diamagnetism and orientational order of nematic liquid crystals*. J. de Physique **43**, 361 (1982).
- [15] J. L. Keddie and A. F. Routh. *Fundamentals of latex film formation*. (Springer, 2010).
- [16] L. S. Palmer. *The chemistry of milk and dairy products viewed from a colloidal standpoint*. Ind. Eng. Chem. **16**, 631 (1924).
- [17] T. Tadros. *Encyclopedia of colloid and interface science*. (Springer-Verlag Berlin Heidelberg, 2013).
- [18] C. N. Likos. *Effective interaction in soft condensed matter physics*. Phys. Rep. **348**, 267 (2001).
- [19] J.-P. Hansen and I. R. McDonald. *Theory of simple liquids*. (Elsevier, 2006).
- [20] J. M. Brader. *Statistical mechanics of a model colloid-polymer mixture*. (PhD thesis, 2001).
- [21] M. Dijkstra, R. van Roij, and R. Evans. *Phase diagram of highly asymmetric binary hard-sphere mixtures*. Phys. Rev. E **59**, 5744 (1999).
- [22] M. Kardar and R. Golestanian. *The “friction” of vacuum, and other fluctuation induced forces*. Rev. Mod. Phys. **71**, 1233 (1999).
- [23] H. C. Hamaker. *The London-van der Waals attraction between spherical particles*. Physica **4**, 1058 (1937).
- [24] A. Gambassi, A. Maciolek, C. Hertlein, U. Nellen, L. Helden, C. Bechinger, and S. Dietrich. *Critical Casimir effect in classical binary liquid mixtures*. Phys. Rev. E **80**, 061143 (2009).
- [25] M. Labbe-Laurent and S. Dietrich. *Critical Casimir interactions between Janus particles*. Soft Matter **12**, 6621 (2016).
- [26] C. Gähwiller. *The viscosity coefficients of a room-temperature liquid crystal (MBBA)*. Phys. Lett. **36A**, 311 (1971).
- [27] I. Haller. *Elastic constants of the nematic liquid crystalline phase of p-Methoxybenzylidene-p-n-Butylaniline (MBBA)*. J. Chem. Phys. **57**, 1400 (1972).

- [28] R. Y. Dong, L. Friesen, and G. M. Richards. *Molecular order and dynamics of the nematogen MBBA. Modelling of deuterium NMR observables*. Mol. Phys. **81**, 1017 (1994).
- [29] K. Skarp, S. T. Lagerwall, and B. Stebler. *Measurements of hydrodynamic parameters for nematic 5CB*. Mol. Cryst. Liq. Cryst. **60**, 215 (1980).
- [30] J. D. Bunning, T. E. Faber, and P. L. Sherell. *The Frank constants of nematic 5CB at atmospheric pressure*. J. Physique **42**, 1175 (1981).
- [31] H.-G. Kreul, S. Urban, and A. Würflinger. *Dielectric studies of liquid crystals under high pressure: Static permittivity and dielectric relaxation in the nematic phase of pentylcyanobiphenyl (5CB)*. Phys. Rev. A **45**, 8624 (1992).
- [32] H. Stark. *Physics of colloidal dispersions in nematic liquid crystals*. Phys. Rep. **351**, 387 (2001).
- [33] P. G. de Gennes. *The physics of liquid crystals*. (Clarendon, Oxford, 1974).
- [34] S. Zumer and S. Kralj. *Influence of K_{24} on the structure of nematic liquid crystal droplets*. Liq. Cryst. **12**, 613 (1992).
- [35] G. P. Crawford, D. W. Allender, and J. W. Doane. *Surface elastic and molecular-anchoring properties of nematic liquid crystals confined to cylindrical cavities*. Phys. Rev. A **45**, 8693 (1992).
- [36] Z. S. Davidson, L. Kang, J. Jeong, T. Still, P. J. Collings, T. C. Lubensky, and A. G. Yodh. *Chiral structures and defects of lyotropic chromonic liquid crystals induced by saddle-splay elasticity*. Phys. Rev. E **91**, 050501-1 (2015).
- [37] Z. Kos and M. Ravnik. *Relevance of saddle-splay elasticity in complex nematic geometries*. Soft Matter **12**, 1313 (2016).
- [38] L. Tran, M. O. Lavrentovich, D. A. Beller, N. Li, K. J. Stebe, and R. D. Kamien. *Lassoing saddle splay and the geometrical control of topological defects*. PNAS **113**, 7106 (2016).
- [39] A. Ferrarini. *The theory of elastic constants*. Liq. Cryst. **37**, 811 (2010).
- [40] R. A. Drawhorn and N. L. Abbott. *Anchoring of nematic liquid crystals on self-assembled monolayers formed from alkanethiols on semitransparent films of gold*. J. Phys. Chem. **99**, 16511 (1995).
- [41] L. Komitov, C. Ruslim, Y. Matsuzawa, and K. Ichimura. *Photoinduced anchoring transitions in a nematic doped with azo dyes*. Liq. Cryst. **27**, 1011 (2000).

- [42] J. M. Brake, A. D. Mezera, and N. L. Abbott. *Active control of the anchoring of 4'-pentyl-4-cyanobiphenyl (5CB) at an aqueous-liquid crystal interface by using a redox-active ferrocenyl surfactant*. Langmuir **19**, 8629 (2003).
- [43] N. A. Lockwood, J. J. de Pablo, and N. L. Abbott. *Influence of surfactant tail branching and organization on the orientation of liquid crystals at aqueous-liquid crystal interfaces*. Langmuir **21**, 6805 (2005).
- [44] J. M. Geary, J. W. Goodby, A. R. Kmetz, and J. S. Patel. *The mechanism of polymer alignment of liquid crystal materials*. J. Appl. Phys. **62**, 4100 (1987).
- [45] D. W. Berreman. *Solid surface shape and the alignment of an adjacent nematic liquid crystal*. Phys. Rev. Lett. **28**, 1683 (1972).
- [46] M. Monkade, M. Boix, and G. Durand. *Order electricity and oblique nematic orientation on rough solid surfaces*. EPL **5**, 697 (1988).
- [47] J. Bechhoefer, B. Jerome, and P. Pieranski. *Systematic studies of the anchoring transition in nematic liquid crystals*. Phys. Rev. A **41**, 3187 (1990).
- [48] G. P. Bryan-Brown, C. V. Brown, I. C. Sage, and V. C. Hui. *Voltage-dependent anchoring of a nematic liquid crystal on a grating surface*. Nature **392**, 365 (1998).
- [49] J. H. Kim, M. Yoneya, and H. Yokoyama. *Tristable nematic liquid-crystal device using micropatterned surface alignment*. Nature **420**, 159 (2002).
- [50] I. Dozov, D. N. Stoenescu, S. Lamarque-Forget, and Ph. Martinot-Lagarde. *Planar degenerated anchoring of liquid crystals obtained by surface memory passivation*. Appl. Phys. Lett. **77**, 4124 (2000).
- [51] O. Ou Ramdane, Ph. Auroy, S. Forget, E. Raspaud, Ph. Martinot-Lagarde, and I. Dozov. *Memory-free conic anchoring of liquid crystals on a solid substrate*. Phys. Rev. Lett. **84**, 3871 (2000).
- [52] J.-H. Kim, M. Yoneya, and J. Yamamoto. *Surface alignment bistability of nematic liquid crystals by orientationally frustrated surface patterns*. Appl. Phys. Lett. **78**, 3055 (2001).
- [53] W. M. Gibbons and S.-T. Sun. *Optically generated liquid crystal gratings*. Appl. Phys. Lett. **65**, 2542 (1994).
- [54] J. Chen, P. J. Bos, H. Vithana, and D. L. Johnson. *An electro-optically controlled liquid crystal diffraction grating*. Appl. Phys. Lett. **67**, 2588 (1995).

- [55] L. M. Blinov, R. Barberi, G. Cipparrone, M. Iovane, A. Checco, V. V. Lazarev, and S. P. Palto. *Liquid crystal orientation by holographic phase gratings recorded on photosensitive Langmuir-Blodgett films*. *Liq. Cryst.* **26**, 427 (1999).
- [56] B. Wen, R. G. Petschek, and C. Rosenblatt. *Nematic liquid-crystal polarization gratings by modification of surface alignment*. *Appl. Opt.* **41**, 1246 (2002).
- [57] V. K. Gupta and N. L. Abbott. *Azimuthal anchoring transition of nematic liquid crystals on self-assembled monolayers formed from odd and even alkanethiols*. *Phys. Rev. E* **54**, R4540 (1996).
- [58] G. Barbero and G. Durand. *On the validity of the Rapini-Papoular surface anchoring energy form in nematic liquid crystals*. *J. de Physique* **47**, 2129 (1986).
- [59] P. Poulin, H. Stark, T. C. Lubensky, and D. A. Weitz. *Novel colloidal interactions in anisotropic fluids*. *Science* **275**, 1770 (1997).
- [60] E. M. Terentjev. *Disclination loops, standing alone and around solid particles, in nematic liquid crystals*. *Phys. Rev. E* **51**, 1330 (1995).
- [61] O. V. Kuskenok, R. W. Ruhwandl, S. V. Shiyanovskii, and E. M. Terentjev. *Director structure around a colloid particle suspended in a nematic liquid crystal*. *Phys. Rev. E* **54**, 5198 (1996).
- [62] R. W. Ruhwandl and E. M. Terentjev. *Monte Carlo simulation of topological defects in the nematic liquid crystal matrix around a spherical colloid particle*. *Phys. Rev. E* **56**, 5561 (1997).
- [63] S. V. Shiyanovskii and O. V. Kuskenok. *Structural transitions in nematic filled with colloid particles*. *Mol. Cryst. Liq. Cryst.* **321**, 45 (1998).
- [64] T. C. Lubensky, D. Pettey, N. Currier, and H. Stark. *Topological defects and interactions in nematic emulsions*. *Phys. Rev. E* **57**, 610 (1998).
- [65] H. Stark. *Director field configurations around a spherical particle in a nematic liquid crystal*. *Eur. Phys. J.* **10**, 311 (1999).
- [66] I. Musevic, M. Skarabot, U. Tkalec, M. Ravnik, and S. Zumer. *Two-dimensional nematic colloidal crystals self-assembled by topological defects*. *Science* **313**, 954 (2006).
- [67] P. Poulin, V. Cabuil, and D. A. Weitz. *Direct measurement of colloidal forces in an anisotropic solvent*. *Phys. Rev. Lett.* **79**, 4862 (1997).

- [68] U. Ognysta, A. Nych, V. Nazarenko, I. Musevic, M. Skarabot, M. Ravnik, S. Zumer, I. Poberaj, and D. Babic. *2D interactions and binary crystals of dipolar and quadrupolar nematic colloids*. Phys. Rev. Lett. **100**, 217803 (2008).
- [69] M. Skarabot, M. Ravnik, S. Zumer, U. Tkalec, I. Poberaj, D. Babic, N. Ostermann, and I. Musevic. *Interactions of quadrupolar nematic colloids*. Phys. Rev. E **77**, 031705 (2008).
- [70] K. Takahashi, M. Ichikawa, and Y. Kimura. *Force between colloidal particles in a nematic liquid crystal studied by optical tweezers*. Phys. Rev. E **77**, 020703 (2008).
- [71] T. Kishita, K. Takahashi, M. Ichikawa, J. Fukuda, and Y. Kimura. *Arrangement dependence of interparticle force in nematic colloids*. Phys. Rev. E **81**, 010701 (2010).
- [72] K. S. Korolev and D. R. Nelson. *Defect-mediated emulsification in two dimensions*. Phys. Rev. E **77**, 051702 (2008).
- [73] O. Guzman, E. B. Kim, S. Grollau, N. L. Abbott, and J. J. de Pablo. *Defect structure around two colloids in a liquid crystal*. Phys. Rev. Lett. **91**, 235507 (2003).
- [74] J. Fukuda, H. Stark, M. Yoneya, and H. Yokoyama. *Interaction between two spherical particles in a nematic liquid crystal*. Phys. Rev. Lett. **69**, 041706 (2004).
- [75] J. Fukuda and H. Yokoyama. *Separation-independent attractive force between like particles mediated by nematic-liquid-crystal distortions*. Phys. Rev. Lett. **94**, 148301 (2005).
- [76] N. M. Silvestre, P. Patricio, M. Tasinkevych, D. Andrienko, and M. M. Telo da Gama. *Colloidal discs in nematic liquid crystal*. J. Phys.: Cond. Matt. **16**, S1921 (2004).
- [77] F. R. Hung. *Quadrupolar particles in a nematic liquid crystal: Effects of particle size and shape*. Phys. Rev. E **79**, 021705 (2009).
- [78] M. Ravnik and S. Zumer. *Landau-de Gennes modelling of nematic liquid crystal colloids*. Liq. Cryst. **36**, 1201 (2009).
- [79] B. I. Lev and P. M. Tomchuk. *Interaction of foreign macrodroplets in a nematic liquid crystal and induced supermolecular structures*. Phys. Rev. E **59**, 591 (1999).
- [80] B. I. Lev, S. B. Chernyshuk, P. M. Tomchuk and H. Yokoyama. *Symmetry breaking and interaction of colloidal particles in nematic liquid crystals*. Phys. Rev. E **65**, 021709 (2002).

- [81] B. I. Lev, H. Yokoyama, S. B. Chernyshuk, and P. M. Tomchuk. *Symmetry breaking, elastic interaction and structures in nematic colloids*. Mol. Cryst. Liq. Cryst. **409**, 99 (2004).
- [82] V. M. Pergamenshik and V. A. Uzunova. *Colloidal nematostatics*. Cond. Matt. Phys. **13**, 33602 (2010).
- [83] V. M. Pergamenshik and V. A. Uzunova. *Coulomb-like interaction in nematic emulsions induced by external torques exerted on the colloids*. Phys. Rev. E **76**, 011707 (2007).
- [84] V. M. Pergamenshik and V. A. Uzunova. *Colloid-wall interaction in a nematic liquid crystal: The mirror-image method of colloidal nematostatics*. Phys. Rev. E **79**, 021704 (2009).
- [85] F. Brochard and P. G. de Gennes. *Theory of magnetic suspensions in liquid crystals*. J. de Physique **31**, 691 (1970).
- [86] J. Rault, P. E. Cladis and J. P. Burger. *Ferronematics*. Phys. Lett. **32A**, 199 (1970).
- [87] S.-H. Chen and N. M. Amer. *Observation of macroscopic collective behavior and new texture in magnetically doped liquid crystals*. Phys. Rev. Lett. **51**, 2298 (1983).
- [88] B. J. Liang and S.-H. Chen. *Electric-field-induced molecular reorientation of a magnetically biased ferronematic liquid-crystal film*. Phys. Rev. A **39**, 1441 (1989).
- [89] S. B. Chernyshuk, B. I. Lev, and H. Yokoyama. *Collective effects in doped nematic liquid crystals*. J. Exp. Theor. Phys. **93**, 760 (2001).
- [90] S. V. Burylov and Y. L. Raikher. *Macroscopic properties of ferronematics caused by orientational interactions on the particle surfaces. I. Extended continuum model*. Mol. Cryst. Liq. Cryst. **258**, 107 (1995).
- [91] A. N. Zakhlevnykh. *Threshold magnetic fields and Freedericksz transition in a ferronematic*. J. Magn. Magn. Mat. **269**, 238 (2004).
- [92] S. V. Burylov and A. N. Zakhlevnykh. *Magnetically induced bistable behavior of ferronematic liquid crystals*. Phys. Rev. E **88**, 052503 (2013).
- [93] S. V. Burylov and A. N. Zakhlevnykh. *Orientational energy of anisometric particles in liquid-crystalline suspensions*. Phys. Rev. E **88**, 012511 (2013).
- [94] V. I. Zadorozhnyi, A. N. Vasilev, V. Yu. Reshetnyak, K. S. Thomas, and T. J. Sluckin. *Nematic director response in ferronematic cells*. Europhys. Lett. **73**, 408 (2006).

- [95] V. I. Zadorozhnii, V. Yu. Reshetnyak, A. V. Kleshchonok, T. J. Sluckin, and K. S. Thomas. *Inverse Frederiks effect and bistability in ferronematic cells*. Mol. Cryst. Liq. Cryst. **475**, 221 (2007).
- [96] A. N. Zakhlevnykh and D. A. Petrov. *Weak coupling effects and re-entrant transitions in ferronematic liquid crystals*. J. Mol. Liq. **198**, 223 (2014).
- [97] A. N. Zakhlevnykh and D. A. Petrov. *Orientational transitions in antiferromagnetic liquid crystals*. Phys. Sol. St. **58**, 1906 (2016).
- [98] P. Kopchansky, I. Potocova, M. Koneracka, M. Timko, J. Jadzyn, G. Czechowski, and A. M. G. Jansen. *The structural instabilities of ferronematic based on liquid crystal with low negative magnetic susceptibility*. Phys. Stat. Sol. **236**, 450 (2003).
- [99] P. Kopchansky, N. Tomasovicova, M. Koneracka, M. Timko, V. Zavisova, N. Eber, K. Fodor-Csorba, T. Toth-Katona, A. Vajda, J. Jadzyn, E. Beaunon, and X. Chaud. *The structural instabilities in ferronematic based on liquid crystal with negative diamagnetic susceptibility anisotropy*. J. Magn. Magn. Mat. **322**, 3696 (2010).
- [100] N. Podoliak, O. Buchnev, O. Buluy, G. D'Alessandro, M. Kaczmarek, Y. Reznikov, and T. J. Sluckin. *Macroscopic optical effects in low concentration ferronematics*. Soft Matter **7**, 4742 (2011).
- [101] N. Podoliak, O. Buchnev, D. V. Bavykin, A. N. Kulak, M. Kaczmarek, and T. J. Sluckin. *Magnetite nanorod thermotropic liquid crystal colloids: synthesis, optics and theory*. J. Col. Int. Sci. **386**, 158 (2012).
- [102] A. Mertelj, D. Lisjak, M. Drofenik, and M. Copic. *Ferromagnetism in suspensions of magnetic platelets in liquid crystal*. Nature **504**, 237 (2013).
- [103] R. Evans. *The nature of the liquid-vapour interface and other topics in the statistical mechanics of non-uniform, classical fluids*. Adv. Phys. **28**, 143 (1979).
- [104] P. Hohenberg and W. Kohn. *Inhomogeneous electron gas*. Phys. Rev. **136**, B864 (1964).
- [105] N. D. Mermin. *Thermal properties of the inhomogeneous electron gas*. Phys. Rev. **137**, A1441 (1965).
- [106] J. A. Nelder and R. Mead. *A simplex method for function minimization*. Comp. J. **7**, 308 (1965).
- [107] M. J. D. Powell. *An efficient method for finding the minimum of a function of several variables without calculating derivatives*. Comp. J. **7**, 155 (1964).

- [108] R. P. Brent. *Algorithms for minimization without derivatives*. (Englewood Cliffs, NJ:Prentice-Hall, 1973).
- [109] D. Goldfarb. *A family of variable-metric methods derived by variational means*. Math. Comp. **24**, 23 (1970).
- [110] W. C. Davidson. *Variable metric method for minimization*. SIAM J. Optim. **1**, 1 (1991).
- [111] W. H. Press, S. A. Teukolski, W. T. Vetterling, and B. P. Flannery. *Numerical recipes in C++*. Second edition. Cambridge University Press (2002).
- [112] R. Fletcher and C. M. Reeves. *Function minimization by conjugate gradients*. Comp. J. **7**, 149 (1964).
- [113] J. R. Shewchuk. *An introduction to the conjugate gradient method without the agonizing pain*. Unpublished (1994).
- [114] T. Jonsson, J. Mattson, C. Djurberg, F. A. Khan, P. Nordblad, and P. Svedlindh, *Aging in a magnetic particle system*, Phys. Rev. Lett. **75**, 4138 (1995).
- [115] B. Groh and S. Dietrich, *Spatial structures of dipolar ferromagnetic liquids*, Phys. Rev. Lett. **79**, 749 (1997).
- [116] P. J. Camp and G. N. Patey, *Structure and scattering in colloidal ferrofluids*, Phys. Rev. E **62**, 5403 (2000).
- [117] H. W. Müller and M. Liu, *Structure of ferrofluid dynamics*, Phys. Rev. E **64**, 061405 (2001).
- [118] B. Huke and M. Lücke, *Magnetic properties of colloidal suspensions of interacting magnetic particles*, Rep. Prog. Phys. **67**, 1731 (2004).
- [119] V. S. Mendeleev and A. O. Ivanov, *Ferrofluid aggregation in chains under the influence of a magnetic field*, Phys. Rev. E **70**, 051502 (2004).
- [120] C. Holm and J.-J. Weis, *The structure of ferrofluids: A status report*, Curr. Opin. Colloid Interface Sci. **10**, 133 (2005).
- [121] C. Rablau, P. Vaishnav, C. Sudakar, R. Tackett, G. Lawes, and R. Naik, *Magnetic-field-induced optical anisotropy in ferrofluids: A time-dependent light-scattering investigation*, Phys. Rev. E **78**, 051502 (2008).
- [122] R. A. Trasca and S. H. L. Klapp, *Structure formation in layered ferrofluid nanofilms*, J. Chem. Phys. **59**, 084702 (2008).

- [123] I. Szalai, S. Nagy, and S. Dietrich, *Linear and nonlinear magnetic properties of ferrofluids*, Phys. Rev. E **92**, 042314 (2015).
- [124] C. Alexiou, R. Schmid, R. Jurgons, Ch. Bergemann, W. Arnold, and F. G. Parak, *Targeted Tumor Therapy with “Magnetic Drug Targeting”: Therapeutic Efficacy of Ferrofluid Bound Mitoxantrone*, in: S. Odenbach (ed.), *Ferrofluids*, Lecture Notes in Physics **594** (Springer, Berlin, 2002), p. 233.
- [125] N. A. Brusentsov, L. V. Nikitin, T. N. Brusentsova, A. A. Kuznetsov, F. S. Bayburtskiy, L. I. Shumakov, and N. Y. Jurchenko, *Magnetic fluid hyperthermia of the mouse experimental tumor*, J. Magn. Magn. Mat. **252**, 378 (2002).
- [126] Q. A. Pankhurst, J. Connolly, S. K. Jones, and J. Dobson, *Applications of magnetic nanoparticles in biomedicine*, J. Phys. D **36**, R167 (2003).
- [127] C. Scherer and A. M. Figueiredo Neto, *Ferrofluids: properties and applications*, Braz. J. Phys. **35**, 718 (2005).
- [128] J. Yao, J. Chang, D. Li, and X. Yang, *The dynamics analysis of a ferrofluid shock absorber*, J. Magn. Magn. Mat. **402**, 28 (2016).
- [129] R. Ravaud, G. Lemarquand, V. Lemarquand, and C. Depollier, *Ironless loudspeakers with ferrofluid seals*, Arch. Acoustics **33**, 3 (2008).
- [130] D.-Y. Kim, H.-S. Bae, M.-K. Park, S.-C. Yu, Y.-S. Yun, C. P. Cho, and R. Yamane, *A study of magnetic fluid seals for underwater robotic vehicles*, Int. J. Appl. Electromagnet. Mech. **33**, 857 (2010).
- [131] S. Odenbach, L. M. Pop, and A. Yu. Zubarev, *Rheological properties of magnetic fluids and their microstructural background*, GAMM-Mitt. **30**, 195 (2007).
- [132] M. T. Lopez-Lopez, A. Gomez-Ramirez, L. Rodriguez-Arco, J. D. G. Duran, L. Iskakova, and A. Zubarev, *Colloids on the frontier of ferrofluids. Rheological properties*, Langmuir **28**, 6232 (2012).
- [133] J.-P. Dery, E. F. Borra, and A. M. Ritcey, *Ethylene glycol based ferrofluid for the fabrication of magnetically deformable liquid mirrors*, Chem. Mater. **20**, 6420 (2008).
- [134] A. Zakinyan, O. Nechaeva, and Yu. Dikansky, *Motion of a deformable drop of magnetic fluid on a solid surface in a rotating magnetic field*, Exp. Therm. Fluid Sci. **39**, 265 (2012).
- [135] M. Shuai, A. Klittnick, Y. Shen, G. P. Smith, M. R. Tuchband, C. Zhu, R. G. Petscheck, A. Mertelj, D. Lisjak, M. Copic, J. E. MacLennan, M. A. Glaser, and N.

- A. Clark, *Spontaneous liquid crystal and ferromagnetic ordering of colloidal magnetic nanoparticles*, Nature Comm. **7**, 10349 (2015).
- [136] Y. Reznikov, O. Buchnev, and O. Tereshchenko, *Ferroelectric nematic suspension*, Appl. Phys. Lett. **82**, 1917 (2003).
- [137] M. Emdadi, J. B. Poursamad, M. Sahrai, and F. Moghaddas, *Behaviour of nematic liquid crystals doped with ferroelectric nanoparticles in the presence of an electric field*, Mol. Phys. **116**, 1650 (2018).
- [138] F. Li, O. Buchnev, C. I. Cheon, A. Glushchenko, V. Reshetnyak, Y. Reznikov, T. J. Sluckin, and J. L. West, *Orientational coupling amplification in ferroelectric nematic colloids*, Phys. Rev. Lett. **99**, 219901 (2007).
- [139] A volume fraction of 3×10^{-4} corresponds to a number density $\rho \approx 1.5 \times 10^{19} \text{ m}^{-3}$ if one considers disc-like particles of radius $R = 35 \text{ nm}$ and thickness 5 nm . This implies a mean distance between the centers of neighboring discs of the order of $r_{\text{mean}} \approx \rho^{-1/3} \approx 400 \text{ nm}$ which leads to a mean magnetic dipole-dipole interaction energy in units of $k_{\text{B}}T$ of (see Ref. [152]) $\beta\varphi_{\text{dd}} \approx \frac{\beta\mu_0 m^2}{4\pi r_{\text{mean}}^3} \approx 3 \times 10^{-3} \ll 1$. Moreover, for typical Hamaker constants $A \approx 1 \times k_{\text{B}}T$, the mean van der Waals interaction energy in units of $k_{\text{B}}T$ is (see Ref. [23]) $\beta\varphi_{\text{vdW}} \approx -\frac{\beta AR^2}{12r_{\text{mean}}^2} \approx 6 \times 10^{-4} \ll 1$.
- [140] V_{NLC} can be expected to be an even function of the particle normal $\boldsymbol{\nu}$ due to the inversion symmetry of the nematic phase (see Subsec. 3.2.2). This allows one to formulate V_{NLC} in terms of the orientation of the magnetic dipole $\boldsymbol{\omega} = \pm\boldsymbol{\nu}$.
- [141] C. Hayes, *Magnetic platelets in a nematic liquid crystal*, Mol. Cryst. Liq. Cryst. **36**, 245 (1976).
- [142] Y. Choi, H. Yokoyama, and J. S. Gwag, *Determination of surface nematic liquid crystal anchoring strength using nano-scale surface grooves*, Opt. Expr. **21**, 12135 (2013).
- [143] The nematic director field $\mathbf{n}(\mathbf{r})$ at position \mathbf{r} minimizes the Frank-Oseen functional in Eq. (3.5) which fulfills the boundary condition $\mathbf{n}(\mathbf{r}) = \mathbf{n}_0$ far away from the colloidal disc. The coupling, according to Eq. (3.2), of the NLC to the disc surface leads to a distortion of $\mathbf{n}(\mathbf{r})$ in the direction e_z of the disc normal. Hence, in order to avoid disadvantageous splay contributions, $\mathbf{n}(\mathbf{r})$ at any position \mathbf{r} has to be parallel to the space spanned by \mathbf{n}_0 and e_z (see Eq. (3.6)).
- [144] M. Tasinkevych, F. Mondiot, O. Mondain-Monval, and J.-C. Loudet, *Dispersion of ellipsoidal particles in a nematic liquid crystal*, Soft Matter **10**, 2047 (2014).

- [145] Having $\mathbf{M} = 0$ everywhere in the sample implies that the density profile $\bar{\rho}$ in Eq. (3.15) is an even function of $\boldsymbol{\omega}$ (i.e., there are as many particles with orientation $\boldsymbol{\omega}$ as there are particles with orientation $-\boldsymbol{\omega}$) which is only possible if $\lambda(\mathbf{r}, [0, \mathbf{n}]) = 0$, provided that $\mathbf{B} = 0$.
- [146] R. Wait and A. R. Mitchell, *Finite element analysis and applications* (John Wiley & Sons, Chichester, 1985).
- [147] Obviously, such a criterion can be chosen in various ways. Moreover, even in the context of the present choice, there is still some degree of freedom in choosing ε .
- [148] A. Mertelj, N. Osterman, D. Lisjak, and M. Copic, *Magneto-optic and converse magnetoelectric effects in a ferromagnetic liquid crystal*, *Soft Matter* **10**, 9065 (2014).
- [149] V. M. Pergamenshchik and V. O. Uzunova, *Coulomb-like interaction in nematic emulsions induced by external torques exerted on the colloids*, *Phys. Rev. E* **76**, 011707 (2007).
- [150] O. Ciftja and I. Hysi, *The electrostatic potential of a uniformly charged disk as the source of novel mathematical identities*, *Appl. Math. Lett.* **24**, 1919 (2011).
- [151] I. S. Gradshteyn and I. M. Ryzhik, *Table of integrals, series, and products* (Academic, New York, 1965).
- [152] J. D. Jackson, *Classical electrodynamics* (John Wiley & Sons, Inc., New York, 1962).
- [153] H. R. Brand and H. Pleiner. *Macroscopic behavior of ferronematic gels and elastomers*. *Eur. Phys. J. E* **37**, 122 (2014).
- [154] A. N. Zakhlevnykh and D. A. Petrov. *Orientational bistability in ferronematic liquid crystals with negative diamagnetic anisotropy*. *J. Magn. and Magn. Mat.* **393**, 517 (2015).
- [155] A. N. Boychuk, D. V. Makarov and A. N. Zaklevnykh. *Dynamics of liquid-crystalline magnetic suspension in a rotating magnetic field*. *Eur. Phys. J. E* **39**, 101 (2016).
- [156] A. N. Zakhlevnykh, M. S. Lubnin and D. A. Petrov. *A simple model of liquid-crystalline magnetic suspension of anisometric particles*. *J. Magn. and Magn. Particles* **431**, 62 (2017).
- [157] A. J. Hess, Q. Liu and I. Smalyukh. *Optical patterning of magnetic domains and defects in ferromagnetic liquid crystal colloids*. *Appl. Phys. Lett.* **107**, 071906 (2015).
- [158] A. Mertelj and D. Lisjak. *Ferromagnetic nematic liquid crystals*. *Liq. Cryst. Rev.* **5**, 1 (2017).

- [159] D. Manaila Maximean. *New grafted ferrite particles/liquid crystal composite under magnetic field*. J. Magn. and Magn. Mat. **452**, 343 (2018).
- [160] G. Zarubin, M. Bier and S. Dietrich. *Effective Landau theory of ferronematics*. J. Chem. Phys. **149**, 054505 (2018).
- [161] T. Potisk, D. Svensek, H. R. Brand, H. Pleiner, D. Lisjak, N. Osterman, and A. Mertelj. *Dynamic magneto-optic coupling in a ferromagnetic nematic liquid crystal*. Phys. Rev. Lett. **119**, 097802 (2017).
- [162] T. Potisk, A. Mertelj, N. Sebastian, N. Osterman, D. Lisjak, H. R. Brand, H. Pleiner, and D. Svensek. *Magneto-optic dynamics in a ferromagnetic nematic liquid crystal*. Phys. Rev. E **97**, 012701 (2018).
- [163] N. Sebastian, N. Osterman, D. Lisjak, M. Copic, and A. Mertelj. *Director reorientation dynamics of ferromagnetic nematic liquid crystals*. Soft Matter **14**, 7180 (2018).
- [164] Segregation effects can be neglected if the segregation parameter $\kappa := D/l$ is much larger than unity [96], where $l := \sqrt{K/(k_B T \rho_{\text{iso}})}$ is the segregation length [85]; for K see Eq. (4.4). In the present study one has $\kappa \approx 7$.
- [165] The NLC in the experiment analyzed in Ref. [102] exhibits twist deformations in the x - y -plane because the twist elastic constant is the smallest Frank modulus of that system. Here we consider the one-elastic-constant approximation so that the system can undergo another type of deformation (i.e., bending) instead. Except for exchanging “twist” by “bend” deformations the results are equivalent because the underlying mathematical model is identical.
- [166] The results of our study are valid only if the *collective* response mode [85] of the ferronematic is realized. The minimum number density of magnetic colloids which facilitates collective behavior is [90]

$$\rho_{\text{coll}} = \frac{1}{cD^2R} \quad (7.7)$$

which gives $\approx 10^{18} \text{ m}^{-3}$ for $c = 0.03$ (i.e., roughly the microscopic coupling constant in the experiment [102, 148]), $D = 20 \text{ }\mu\text{m}$, and $R = 100 \text{ nm}$. Due to $\rho_{\text{iso}} = 1.5 \times 10^{19} \text{ m}^{-3} > \rho_{\text{coll}}$ and because $D = 20 \text{ }\mu\text{m}$ is the minimum thickness used here, the assumption of occurrence of collective behavior is valid.

- [167] The positive constant a in Eq. (4.1) is unimportant as long as $|\mathbf{M}| = m\rho_{\text{iso}} = \text{const.}$ It becomes relevant otherwise, i.e., if segregation is taken into account (see Sec. 4.4).

[168] In the case of soft anchoring the interaction of the NLC with the wall surface is described by the free energy potential

$$F_s = W \int_{\partial\mathcal{V}} d\mathbf{s} [\mathbf{n}(\mathbf{s}) \times \boldsymbol{\nu}(\mathbf{s})]^2, \quad (7.8)$$

where $W > 0$ is the anchoring strength at the wall surface $\partial\mathcal{V}$, and $\boldsymbol{\nu}(\mathbf{s})$ is the easy axis direction at the surface point \mathbf{s} . In the case of a planar wall surface with constant easy axis the above expression reduces to the form used in Eq. (4.5). The soft anchoring at the surface of the colloids is taken into account implicitly within the derivation of the free energy density given in Eq. (4.1) [160].

[169] According to the numerical investigation of the one-particle elastic potential carried out in Ref. [160] one finds that as long as the weak anchoring regime ($c < 0.1$) is valid, the rotation of a single colloid is accompanied by the breaking of the surface anchoring at the surface of the colloid. For example, if the angle between the normal of the surface of the disc and the far-field director is $\pi/2$, the director at the surface is *parallel* to the surface while anchoring favors the perpendicular orientation. An alternative mechanism is represented by the formation of a defect in the NLC in the vicinity of the particle. The latter scenario corresponds to the case in which the nematic director is *strongly* anchored at the particle surface (i.e., $c \gg 1$) and thus is not relevant in the context of the experiments considered in Refs. [102, 148].

[170] The two-domain state required us to tune the elastic constant K , because for certain values of K the minimization algorithm produced throughout the sample a perturbed director profile for $B = 0$ as a favorable state. In order to make the corresponding elastic distortions more costly, we increased the value of K to 9×10^{-12} N compared to $K = 3.5 \times 10^{-12}$ N used in Secs. 4.3.1, 4.3.2, and 4.4.

[171] The position of the interface depends on the external field *strength* which should be chosen such that the interface is located approximately in the middle of the slab. We used the values $B = 12$ mT together with $\gamma \approx 240$, $W_{\text{wall}}^{(1)} = 1 \times 10^{-5}$ J/m², $W_{\text{wall}}^{(2)} = 0.1 \times 10^{-5}$ J/m², and $K = 9 \times 10^{-12}$ N.

Acknowledgements

I would like to thank Prof. Dr. Siegfried Dietrich for giving me the opportunity to work in his group. From the very first lecture in (Advanced) Quantum Mechanics during the first semester of my Master's study till the present day it was a great experience to observe the way you work and share opinions.

I am thankful to Prof. Dr. Christian Holm and Prof. Dr. Tilman Pfau for being a part of the committee during my PhD exam.

I am infinitely grateful to Prof. Dr. Markus Bier for supervising me along the way. Your sharp mind always managed to pinpoint the important piece I should focus on. You were always open for discussion even though I can only imagine how much work there was to deal with.

Many thanks to Frau Anke Geigle for managing all the bureaucracy and helping me with filling out forms and such. I really appreciate that because I personally try to avoid dealing with official documents as much as possible but whenever I had to it was not hard since Frau Geigle did all the preparatory work and was very helpful and kind.

I also thank Dr. Paolo Margaretti for many useful discussions and advices and for exposing me, a somewhat grumpy Russian guy, to a positive and open Italian attitude.

Of course I would like to acknowledge my other colleagues I had a pleasure to work with during the years, in particular Hendrik Bartsch, Dr. Nima Farahmand Bafi, Dr. Markus Gross, Dr. Andreas Reindl, Dr. Marcel Labbé-Laurent, Melanie Lipp, Maximillian Mußoter, Dr. Sutapa Roy, Dr. Arghya Majee, Dr. Mihail Popescu, Dr. Adam Law, Dr. William Uspal, Dr. Piotr Nowakowski, Dr. Christian Rohwer, Dr. Matthias Krüger and others. You all contributed to a very friendly working atmosphere.

I cannot express in words how grateful I am to my parents for all the love and support they gave me. Without them with probability 1 I would not be the person I am. I would like to dedicate this thesis to them. I love you very much mom and dad.